Thin Films Containing Heavy Group V Elements as Systems for Topological Materials

Matthew Thomas Vaughan

University of Leeds

School of Physics and Astronomy

Submitted in accordance with the requirements for the degree of

Doctor of Philosophy

August, 2020

Intellectual Property Statement

The candidate confirms that the work submitted is his own and that appropriate credit has been given where reference has been made to the work of others.

This copy has been supplied on the understanding that it is copyright material and that no quotation from the thesis may be published without proper acknowledgement.

The right of Matthew Thomas Vaughanto be identified as Author of this work has been asserted by him in accordance with the Copyright, Designs and Patents Act 1988.

Acknowledgements

I would like to thank my supervisor Gavin Burnell for his help and ever-useful advice during the course of my study. I would like to thank our experimental office Mannan Ali for his exhaustive knowledge of experimental techniques. Ruaraidh MacInnes for helping to modify and troubleshoot Megatron. Nathan Satchell for help with my first beamline experiment. Additionally, I would like to thank Craig Knox, Rowan Temple, Tim Moore, Alex Huxtable, Ben Steele, and Josh Gretton for their support and assistance during my research.

The POLREF team at ISIS was of excellent help during our experiment there and I would like to thank Christian J. Kinane, Gavin B. G. Stenning, and Sean Langridge.

The LEMAS facility at Leeds for providing amazing images and data for my work on half Heusler alloys and I would like to thank John Harrington and Zabeada Aslam for their time.

I would also like to thank the changing of the seasons for allowing me to observe the annealing of Bi/Ni bilayers. Without it, our poorly air-conditioned office could not have been hot enough and then cold enough to observe room temperature annealing.

Finally, but not least, I would like to thank my friends and family. My Parents for their constant support and encouragement. Rob Welch has provided excellent proofreading and also telling me not to work too many weekends, without his assistance this thesis would have been 10 pages longer but not nearly as readable.

Abstract

This thesis looks at growing thin films of heavy group V elements as well as using Pt to study high spin-orbit coupling for topological materials. We start with Bi/Ni bilayers that had been claimed to exhibit an usual form for superconductivity at the interface, instead we found that Bi will diffuse across the interface at room temperature over a timescale of days. The Bi would then alloy with the Ni to create the superconducting alloy $NiBi_3$ and that elevated temperatures would accelerate this process even faster. After this we continued on to heavy half Heusler alloys, growing epitaxial thin films of YPtSb and YbPtBi on c-plane sapphire. The YPtSb thin films grew as smooth continuous layers with high quality crystallinity, but without any transport properties to point to a topological state. YbPtBi on the other hand, grew as aligned triangular islands and we observed a negative longitudinal magnetoresistance that may originate from the chiral anomaly. The chiral anomaly is an expected property of a topological Weyl semimetal. Both YPtSb and YbPtBi were matched well with the c-plane sapphire surface with induced strain and so this process could be used for other half Heusler alloys in the future.

CONTENTS

List of Figures

LIST OF TABLES

Abbreviations

AC	Alternating Current	SLD	Scattering Length Density
AFM	Atomic Force Microscopy	SOC	Spin-Orbit Coupling
ARPES	Angle-Resolve Photo-Emmision Spectroscopy	SQUID	Superconducting Quantum Interference Device
BCS	Bardeen-Cooper-Schrieffer	TI	Topological Insulator
DC	Direct Current	UHV	Ultra High Vacuum
EDX	Energy Dispersive X-Ray Spectroscopy	VSM	Vibrating Sample Magnetometry
FIB	Focused Ion Beam	VTI	Variable Temperature Insert
FOM	Figure of Merit	WSM	Weyl Semimetal
FWHM	Full Width Half Maximum	XRD	X-ray Diffraction
HHA	Half Heusler Alloy	XRR	X-ray Reflectometry
PNR	Polarized Neutron Reflectometry		

CHAPTER 1

Introduction

Physics and topology have had a long twisted history. The field of topology was started when Euler proved it was impossible to cross all the bridges of Königsberg once and only once [29]. Although the term topology would not be in common use until around 1920, Euler and those bridges started graph theory and the early study of topology. Before topology gained its name, Kirchhoff was using graph theory in 1845 to understand electrical networks [75]. Graph theory eventually led to knot theory, and knotted vorticity was an early failed model of the structure of atoms [51, 70]. Recently, however, physics has started to use topology as it is proving useful for defining differences in states that cannot be differentiated by symmetries alone, as was usually done for many types of phase transitions [67]. Then the essential question that could be said to define topological insulators (TI) is: 'given any insulator with a gap, can it be continuously deformed into any other insulator? In effect are these insulators all equivalent systems?' The answer is no, and we can start to look at how these non-trivial topological states differ from the trivial non-topological counterparts.

The quantum Hall effect was first measured in 1978 in Si at high magnetic fields and is perhaps the first direct measurement of a topological state and the edge states [48], although the idea of topological materials was not to be developed until 2003 [7]. The first system to feature intrinsic non-trivial topology was the inverted band gaps in HgTe/CdTe quantum wells back in 2006 as a quantum spin Hall effect, also known as a 2D topological insulator (TI) [15]. Soon after 3D TIs were found in bulk samples of $Bi_{1-x}Sb_x$ [46]. The number of TI materials has continued to expand ever since [8].

Not only has the number of materials exhibiting TI states increased, but the types of topological materials have also expanded. Topological matter now includes various types of topological superconductivity and Weyl semimetals [102]. Weyl semimetals may potentially exist in some of the half Heusler alloys with rare-earth f-electrons as will be discussed later [44]. Weyl semimetals have an advantage over topological insulators as Weyl semimetals have a useful bulk transport effect, the chiral anomaly, that can be used to indicate the presence of a topological state.

Many of the 3D TIs have been studied as bulk signal crystals. But growing TI as thin films has the advantage that there is reduced bulk to surface ratio, thus surface effects become pronounced over the bulk properties. Additionally thin film technology is a highly developed area and successful growth of high-quality TI can take advantage of the nanofabrication process for research on topological matter. And also industry can

adapt thin film TIs into their established processing infrastructure. The morphology of thin films is considerably different from that of the bulk. Even when not considering induced strain, the free surface of the thin film can distort the normal bulk properties. Most multilayer structures are understood to be metastable and that layer diffusion occurs on a long timescale, but that is not always the case (Ch. 4). Overall thin films introduce some challenges to create high-quality materials with the desired properties.

Topological insulators use heavier elements from the lower part of the periodic table and often the group V elements, e.g. Sb, Bi. These have high spin-orbit coupling that is needed to cause band inversion which is the source of the non-trivial topology. We will, therefore, take a detour away from strictly topological systems to look at bismuth nickel bilayers where it had been suggested that a non-trivial topological state might exist [39], along with other potential interesting physics [39, 103]. Bi/Ni bilayers incorporate strong spin-orbit coupling, ferromagnetism, and superconductivity even when neither Bi or Ni are superconducting. At first, it would seem this interface has produced a superconducting phase even in the presence of a strong exchange field where singlet cooper pairs would be destroyed. All of these factors lead to potential forms of exotic states, in particular, the topological states motivated us toward looking at Bi/Ni bilayers. What we found instead was that the $NiBi_3$ superconducting alloy can form at the interface of Bi/Ni layers at room temperature by the diffusion of the Bi/Ni interface. The low temperature annealing is an obstacle when trying to study clean interfaces so we look in detail at the process of interface annealing.

Once we have finished with the interesting problem of low temperature annealing of Bi/Ni bilayers we come back to the search for non-trivial topological matter. Half Heusler alloys have recently become a promising material to harbor such topological states as DFT calculations have predicted an inverted bandgap [21]. Half Heusler alloys can be made of heavy elements for strong spin-orbit coupling, share a similar crystal structure to already studied TIs, and are tunable by easy element substitution.

YPtSb is the first attempted half Heusler alloy (HHA) here as it avoids using Bi and is a lesser explored material with potential for interesting TI states. Bi has a melting point low enough that heating from sputtering can damage the target. Although the constituent elements are lighter compared to other TI materials there is already some work on YPtSb as thin films grown on MgO substrates. So we knew that thin films of YPtSb are possible and we expanded on this work by inducing epitaxial strain. We

successfully grew epitaxial YPtSb as smooth continuous layers on c-plane Al_2O_3, but did not find evidence of a topological state.

Using Yb in a half Heusler alloy leads to the issue of the unfilled f-shells that would act as a local magnetic moments which may interfere with the topological insulator surface states. Additionally, DFT calculations suggested it would be more metallic like than semiconducting with no bandgap [2]. So it was not considered in some early theoretical work on topological insulators [21]. But HHA with rare earth unfilled f-shells were eventually of interest as a potential candidate Weyl semimetal instead [40, 92]. We grew YbPtBi as epitaxial triangular islands with interesting transport properties that hint at a potential Weyl semimetal state.

CHAPTER 2

Theory and Background

The background behind topological matter brings together band theory, spin-orbit coupling and crystal symmetries. The interaction of topological matter with superconductivity, ferromagnetism and under the application of electric and magnetic fields is also briefly introduced here. This chapter serves to give a short introduction to the physics used within this work, for further detail I would recommend several review papers on the subject [8, 113, 114].

2.1 Topological Matter

Topology is the study of connected spaces, whether it is the surface of simple 2D/3D shapes such as a sphere or a torus or the links in a graph. We can apply it to ideas in condensed matter physics where the space we are working in may instead be reciprocal space such as momentum space. To discuss how momentum space can have topological ordering we first need to understand band structures and the behaviour under band inversion.

2.1.1 The Band Inversion

Both insulators and semiconductors have a bandgap between the highest occupied state and the lowest unoccupied state, some finite energy is needed to excite an electron in the higher state. The major difference is that the semiconductor has a smaller bandgap, typically of the order $\approx 1\,\text{eV}$, where as a rough guide at least a few electrons can be thermally excite before the materials melt. This bandgap range is also technologically useful for photovoltaics and p-n junctions. Semiconductors with very narrow bandgaps will be most relevant in this work as HHA TIs typically have very small bandgaps where thermal excitation at room temperature are significant. Any defects or impurities would also add to the available charge carriers as it would move the Fermi level away from the bandgap. These non-thermal carrier sources are a big concern for TIs with all sizes of bandgaps. At first it would seem that it would always be possible to smoothly increase the bandgap of a semiconductor until it behaved as an insulator, and for most semiconductors that would be correct, but not if there is band inversion.

Through spin-orbit coupling (SOC) acting on the orbital momentum type of the band structure, moving bands with angular momentum such as p-like ,d-like, etc bands in energy. With strong enough SOC the bandgap becomes inverted and the oppor-
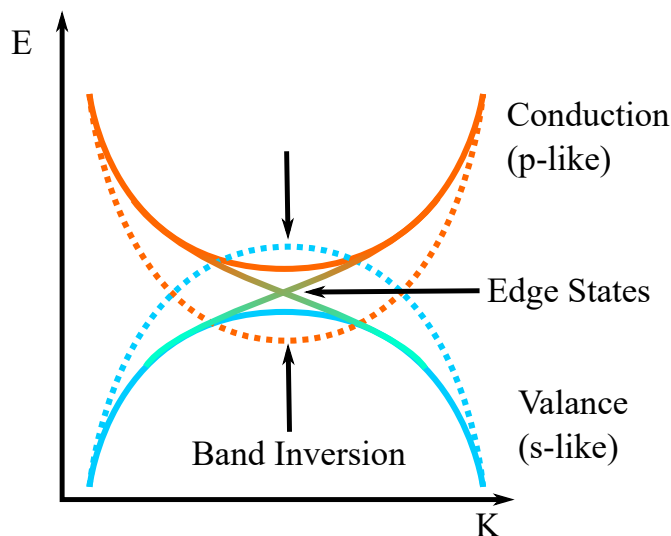
Figure 2.1: TI band inversion induced by SOC acting on the band orbital type. The conduction band and valance band are separated by an energy gap that is traversed by the topological edge states.

tunity for non-trivial topological states can exist (Fig. 2.1). The uncrossing of bands is a discontinuous process and allows for the change in topology as well as the topologically protected surface states. SOC originates from relativistic corrections and is proportional to the atomic weight of the host atoms. These relativistic corrections are usually small even for very heavy atoms and can only make small changes to the band energies which means a TIs bandgap is typically no large than 350 meV [6]. Thus a room temperature topological insulator is highly susceptible to defects, impurities and even thermal effect for smaller bandgaps leading to a significant number of bulk charge carriers that will impede measurements of the conductive surface state.

2.1.2 Berry Flux and Chern Numbers

One method to distinguish the different topologies is the Chern number calculated from the Berry curvature, not all topological system can be characterized this way but it is useful for Weyl semimetals as discussed later. The Berry curvature or Berry Flux is a measure of the phase shift in a particle's state as it is transported along a closed loop 2.2, this is mathematically similar to parallel transporting a vector around a closed loop on a surface. The change in the phase/vector direction is proportional to

the Berry flux/curvature enclosed within the loop and is way the Berry phase is also called the geometric phase as it is only dependent of the path and not time. More precisely the Berry curvature can be define from the Berry connection which is defined as $\mathcal{A}_m = i \langle R(k) | \nabla | R(k) \rangle$, where $R(k))$ is local state is the parameter space k, the expression is then the gradient of the parameter space. The Berry curvature is then the curl of the gradient of the parameter space, defined as $\mathcal{F}_m = \nabla \times \mathcal{A}_m$.
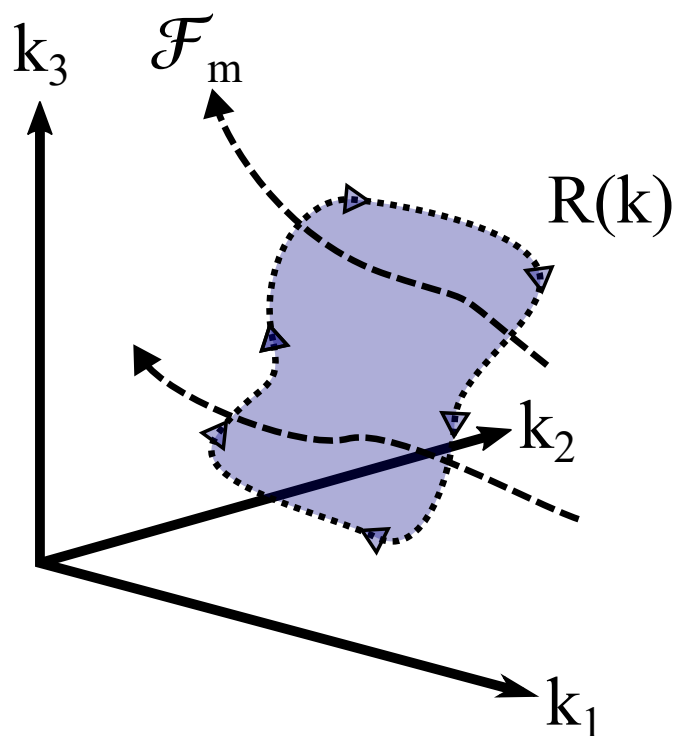
Figure 2.2: As the state $R(k)$ travels around a closed loop in parameter space, k_n, is encloses Berry flux adding a phase to the state. The closed path also defines a surface over which the phase can be calculated from. If this surface is closed like a sphere then the total Berry flux will be quantized by the number and charge of Berry flux monopoles within the sphere.

If we integrate the Berry flux for a closed path we get the total flux through the surface enclosed by the path and use Stokes theorem redefine to integral over the surface instead, further if the surface itself is closed then the total Berry flux becomes an integer multiple of 2π called the Chern number 2.2. To further solidify the connection between mathematical topology and the topology in condensed matter, the way the

Chern number is calculated is nearly identical to the Euler characteristic. The Euler characteristic is a topological invariant that separates different topologies, e.g. spheres have a value of 2 and a torus has a value of 0.

$$N_C = \frac{1}{2\pi} \oint_{S_k} dk \; \mathcal{F}_m \tag{2.1}$$

$$\xi = \frac{1}{2\pi} \oint_S dS \; K \tag{2.2}$$

N_C is the Chern number and $\mathcal{F}_m$ is the berry flux, the integration is over a closed surface in of momentum space, S_k (Equ. 2.1). Equation 2.2 calculates the Euler characteristic ξ by integrating the curvature (K) over the surface of a shape. Without monopoles of Berry flux or winding, the flux lines must form closed loops that integrate to zero. Similarly, over the surface of a sphere, areas of deformation must add and subtract equal amounts of curvature. Chern/Euler numbers can only change by an integer amount as Berry flux monopoles/holes are added or removed. Monopoles are not the only source of non-zero Chern numbers, there can also be an integer winding number. Thus both of these values are invariant except under a change of topology. They are similar because they are can both be derived from the same Chern-Gauss-Bonnet theorem [23].

Naturally, free monopoles of Berry flux don't exist in a vacuum; so the vacuum, as expected, must be topologically trivial. This raises the question of 'what must need to happen at the boundary of topological matter?'. The answer is we find special surface states. These surface states must exist as they allow a transition between trivial and non-trivial topologies; and manifest for topological insulators (TI) as a conducting edge with spin locking momentum and for Weyl semimetals as Fermi arcs on the surface connecting the Weyl nodes in the bulk band structure, see figure 2.3.

2.1.3 Weyl Semimetals

Weyl fermions are a solution to the Dirac equation for a massless fermion [108]. Neutrinos were speculated to be Weyl fermions until neutrino oscillation was discovered and proved that they had a small but non-zero mass [89]. It is yet to be determined if massive neutrinos are now Dirac fermions like the rest of the leptons or are instead Majorana fermions [78]. Weyl semimetals are the condensed matter analog to the particle physics Weyl fermions.
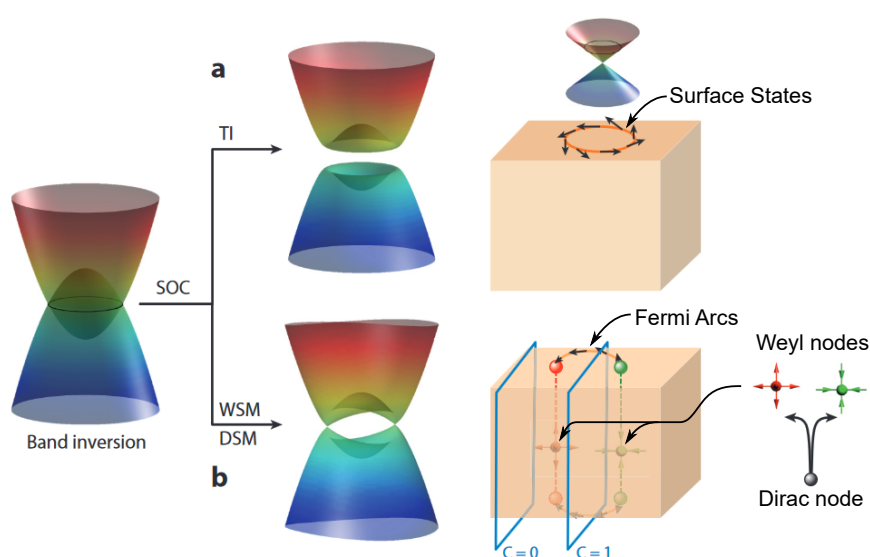
Figure 2.3: Illustration of band inversion and the the resultant TI state (a) or Weyl semimetal (WSM) state (b). The TI has edge states with Dirac cone momentum locking spin (black arrows), whereas the Weyl semimetal (b) has Fermi arcs with chiral currents (Parallel spin and momentum) at the surface connecting the Weyl nodes. The blue planes represent integrating the Berry flux over a limited space, returning the Chern number C. Diagram taken from [81].

The Weyl semimetal state could be thought of as the exact critical point between a normal and TI state, the Dirac cone that would appear at the surface of a TI is now in the bulk and has been split in momentum space into cones of opposite chirality as Weyl nodes. The splitting of the Dirac point is achieved by breaking either Time-Reversal Symmetry (TRS) or lattice inversion symmetry. Half Heusler alloys already have the necessary inversion symmetry breaking built into the crystal lattice. Weyl nodes always come in pairs and act as sources and sinks of berry flux in the bulk band structure.

As previously discussed, topological insulators can be characterized by a non-zero Chern number; Weyl semimetals are different in that the Chern number for the whole system is zero but for some local cases is non-zero (Fig. 2.3.b). Specifically in between two Weyl nodes, as each Weyl node is a source or sink of Berry flux. A plane placed between two Weyl nodes will have a net Berry flux, thus a non-zero Chern number. The non-zero Chern number guarantees that surface states will exist to reconnect the Weyl node and remove the monopoles of berry flux. These surface states manifest as Fermi arcs and have been observed in TaAs using Angle Resolved Photo Emission Spectroscopy (ARPES) [112]. ARPES is an expensive technique that is very sensitive to surface defects, and while a successful observation of Fermi arcs is unambiguous of Weyl nodes, a more obtainable option would be desirable. The chiral anomaly is a bulk negative longitudinal magnetoresistance which will be described later (Ch. 2.2.2).

2.2 Electronic Transport

2.2.1 Ordinary Hall Effect

The Hall effect arises as a voltage difference across a sample that is both perpendicular to the current and magnetic field when a magnetic field is applied out-of-plane on the sample. When carriers flow through a conductor in a magnetic field they are acted on by a Lorentz force. This causes charges to accumulate on one side of the sample. The Ordinary Hall Effect is anti-symmetric in B, $V_H(B) = -V_H(-B)$, and has a negative(positive) slope for electron(hole) type carriers.

$$V_H = \frac{IB}{etn} \tag{2.3}$$

The Hall voltage in equation 2.3 can be derived from simple Lorentz forces acting on a 2D free gas of electrons(holes) in a sample with a carrier density n, applied current
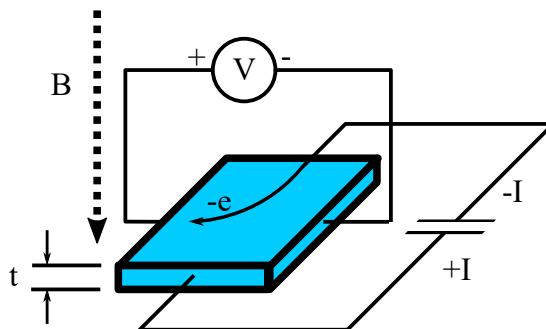
Figure 2.4: Hall effect geometry, here an electron is the carrier. The Lorentz force accumulates electrons on the positive side of the voltmeter and so reads a negative voltage.

I, magnetic field B, and of a known thickness t. Our samples are not expected to be thin enough for a 2D system but the ordinary Hall effect will be give the correct carrier density if the thin film is macroscopically thin and uniform. The quantum Hall effect does require a 2D electron gas but is not observed in this work. The Hall voltage is not dependent on any other geometric considerations. The mobility can also be calculated as long as the conductivity is also known using the relation, $\sigma = ne\mu$. The Hall effect is utilized extensively to measure the carrier density and mobility as useful metrics of sample quality, but of further interest are the other Hall effects that may potentially appear such as the anomalous Hall effect (AHE) in ferromagnets and the topological Hall effect (THE) for topological materials. Although the THE and AHE was not observed within this work, other groups have measured it in half heusler alloys [40, 92].

2.2.2 Magnetoresistance

The change of the sample resistivity with an applied magnetic field is known as Magnetoresistance (MR). The MR is symmetric in B, $MR(B) = MR(-B)$, from time-reversal symmetry and is said to be positive(negative) when the resistance increases(decreases) with increasing field.

Ordinary magnetoresistance in non-magnetic metals is mostly dependent on the shape of the Fermi surface which the the surface for constant energy in momentum space and usually separates filled and unfilled bands. Wherever the Fermi surface is closed or open effects the allowed cycltron paths along the surface and always has causes an increase in resistivity with an increase in magnetic field.

Anisotropic Magnetoresistance

For ferromagnetic metals the strength of the MR is dependent on the angle between the current path and the magnetization leading to the term Anisotropic MR (AMR). The AMR is the result of both the action spin-orbit coupling and magnetization on two channels of up and down spin electrons [20]. In samples with conductive s-bands and spin split ferromagnetic d-bands that are spin in-balanced at the Fermi energy, the SOC causes mixing between the $d_\uparrow$ and $d_\downarrow$ bands. The AMR usually varies as $cos^2(\theta)$ since $\theta + \pi$ is equivalent to a reversal of the field direction and that MR is symmetric in field.

Weak Localization

Within a disordered system of many scattering sites electrons travel in diffusive random walks. By allowing for phase coherence after many collisions we can no longer use classical random walks and quantum interference over many possible paths must be considered. Weak localization occurs as traveling either direction around a scattering loop has an identical path length which then interfere constructively (Fig. 2.5) [26]. This makes circular motion more common than it would otherwise be and increases the resistivity. Introducing SOC into the system creates weak anti-localization (WAL) that instead reduces the resistance. Traveling in opposite directions around a loop with spin coupling to the momentum rotates the spin in opposite directions causing destructive interference making circular paths less common.
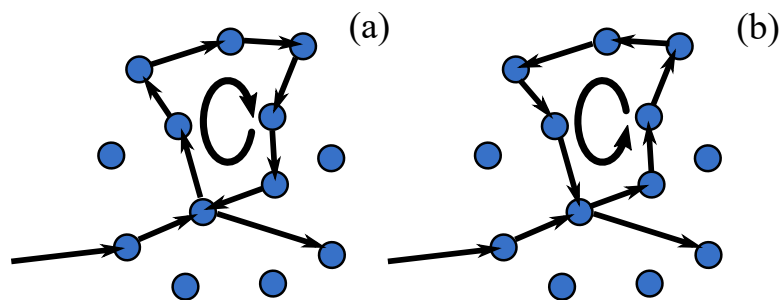
Figure 2.5: A system of scattering sites traversed by a charge carrier. Scattering loops clockwise (a) or anti-clockwise (b) have identical path lengths. Under weak localization these paths constructively interfere making loops like this more frequent.

Weak localization is quickly destroyed by an applied magnetic field. The field

applies a shift in the phase depending on the direction of travel around the loop. The self intersecting paths no longer interfere as they would have and so are no longer as common.

Longitudinal Magnetoresistance

The concept of the chiral anomaly originates from particle physics and refers to an imbalance of chiral fermions [1]. In theories with the chiral conservation law, there must always be an equal number of left-handed and right-handed chiral particles. In Weyl semimetals, the chiral anomaly manifests when parallel magnetic and electric fields are applied and creates a chemical potential difference between the opposite chiral Weyl nodes. The two Weyl nodes have opposing chirality and the pumping of charge from one node to another creates an imbalance in the number of chiral fermions, hence the chiral anomaly [73]. The pumping of charges and imbalance can be measured as a reduction in the resistance leading to a negative longitudinal magnetoresistance (LMR). When the magnetic and electric fields are perpendicular the chiral anomaly is no longer present. The conductivity, σ (Equ. 2.4), of a Weyl semimetal is predicted to follow a parabolic trend with magnetic field in the LMR orientation [47]. The shape is given by the following equation for a parabolic MR and weak localization contributions:

$$\sigma = (1 + c_a H^2)\sigma_{WAL} + \sigma_N \tag{2.4}$$

Where c_a is the chirality constant and σ_{WAL} is the weak anti-localization. The weak anti-localization is given by the equation $\sigma_{WAL} = \sigma_N + a\sqrt{H}$, σ_N is the normal zero-field conductivity and a is the strength of the weak localization. This equation can be fitted to an MR measurement to extracted the chirality constant c_a.

As the temperature increases, there is an increase in chirality flipping scattering as the additional thermal energy is enough to overcome the chemical potential difference [34, 56]. The temperature dependence of the chirality constant, c_a, can be fitted using a $1/T^2$ trend given in equation 2.5. A negative LMR and a good fit to the temperature dependence would be a strong indication of a chiral anomaly.

$$c_a(T) \propto \frac{\nu_f^3 \tau}{(T^2 + \frac{\mu^2}{\pi^2})} \tag{2.5}$$

Where μ is the chemical potential between the Weyl node and τ is the chirality

flipping scattering time. Since the chiral anomaly only arises in the LMR orientation it should be the case that there is an angular dependence on the MR as it moves away from parallel current and field. Indeed it could be that a positive MR results from the presence of normal Lorentz forces MR when the electric and magnetic fields are perpendicular.

2.3 Superconductivity

Superconductivity is an essential component to modern condensed matter physics and within this work is of interest as a potential place to find non-trivial topology. Not only will superconductivity be needed for the work on Bi/Ni bilayers, but also some half Heusler alloys have been measured to be superconducting [68].

Bardeen-Cooper-Schrieffer (BCS) theory is the most well-established method to describe the mechanism for typical superconductivity [9]. It explains superconductivity as an attraction that exists between the electrons in superconductors, normally mediated by electron-phonon interactions, that pairs up electrons into Cooper pairs. The strength of the pairing determines the superconducting gap and the resultant superconducting temperature. Additionally, a pair of $\frac{1}{2}$-spin electrons always have a summed integer spin and so Cooper pairs can be considered a composite boson that can form a Bose-Einstein condensate. The electron-phonon attraction implies a spatially symmetric wavefunction, thus singlet pairing is most common and since electrons are fermions, obeying the Pauli exclusion principle, must have anti-aligned spins (Equ. 2.6). S is the spin of the cooper pair and is allows zero for singlet pairs.

$$S = 0 : \frac{1}{\sqrt(2)} \left[|\uparrow\downarrow\rangle - |\downarrow\uparrow\rangle \right] \tag{2.6}$$

Since the creation of BCS theory theorists and experimentalists have looked for ways to create new exotic types of superconductivity. singlet superconductors are naturally suppressed by strong magnetic fields and exchange interaction as each tries to force spins to align. The natural extension to BCS superconductors would be to switch to triplet pairing.

$$S = 1 : \uparrow\uparrow$$
$$S = 0 : \frac{1}{\sqrt{(2)}} [\uparrow\downarrow - \downarrow\uparrow] \qquad (2.7)$$
$$S = -1 : \downarrow\downarrow$$

Triplet superconductors can have aligned spins and so could be compatible with ferromagnetism as opposed to singlet superconductors (Equ. 2.7). The triplet cooper pairs can now have both a net total spin that can couple with any magnetization or SOC present. Such a state is then very interesting to study as a rich area of possible interactions of ferromagnetism, superconductivity, and high SOC systems. A triplet pairing component can be induced in an singlet pairing superconductor at a superconducting-ferromagnetic junction that are similar to our Bi/Ni bilayers [31]. These types of pairings have applications in spintronics and classical superconducting computing.

Cooper pairs additional have an parity compound as well as the spin component,S, and can be split into s-wave and p-wave which are spatially symmetric and antisymmetric respectively. Thus P-wave superconductors are fragile against retroreflections. When a p-wave cooper pair is reflected without spin flipping, which would need TRS breaking, it becomes destructive to the p-wave state. So it is potentially beneficial to combine p-wave with TIs as the surface states are prevented from back scattering.

S	P*	O	T*
-1	+1	+1	+1
+1	-1	+1	+1
+1	+1	+1	-1
-1	-1	+1	-1

Table 2.1: The allowable symmetry permutations for cooper pairs when restricted to a single band system (O=1). Spin singlet and triplet states correspond to S=-1 and S=+1. p-wave and s-wave correspond to P*=-1 and P*=+1. Odd and even frequency correspond to T*=-1 and T*=+1.

Berezinskii found that for cooper pair correlation functions to obey fermion properties the permutation symmetries of spin (S), parity (P*), orbital (O) and time (T*) must conserve $SP*OT* = -1$[11]. The spin and parity permutation operations relate to the singlet/triplet state and the s-wave/p-wave type respectively. The Orbital per-

mutation is for multiband models. Finally the time permutation leads to even or odd frequency superconductors. Similar to how the -1 parity causes a spatial antisymmetric wave, the odd even frequency leads to correlation this is antisymmetric in time and thus is an odd function instead of an even function. The vast majority of superconductors are even frequency, but odd frequency can be induced in systems that change these symmetries. As mentioned previously a singlet s-wave cooper pair injected across a superconducting-ferromagnetic interface induces a triplet component, but to preserve the Berezinskii condition the even frequency singlet s-wave cooper pairs must become an odd frequency s-wave triplets.

2.4 Magnetic ordering and Heavy Fermions

In later chapters we will be using the rare earth element Yb in YbPtBi (Ch. 6) and working with ferromagnetic Ni in Bi/Ni bilayers (Ch. 4). The origin of magnetism in materials normally starts with partial filled d or f electron orbitals of the transition metals or rare earths respectively. While the Ni in our Bi/Ni bilayers is a typical ferromagnet; YbPtBi has a rich magnetic phase of localized moments and low temperature antiferromagnetism [30, 99].

Ferromagnetism is usually modeled using the molecular mean-field [105]. The molecular field parallel aligns spins by making it more energetically favorable compared to anti-aligned spins. Dipole-dipole interaction would, without a molecular field, anti-align spins to minimize the energy of the system. Coulomb repulsion of overlapping electron orbitals creates an exchange interaction that is the source of the molecular mean-field. These are usually d-orbitals and f-orbitals, and only for particular orbital overlaps found in some crystal structures. The austenitic iron phase is non-ferrous because the crystal structure is fcc and not a body-centered cubic (bcc).

The radial probability distribution function of the f-orbital is confined close to the host atom, the overlap between adjacent moments is limited and so these are often called localized moments. As an element's Z increases, the f-orbitals contract closer to the host atom as Coulomb attraction increases. The lower row has greater electron shielding so the f-electrons are less tightly bound and less localized. The only major exception is the last column of the f-block, as they have full f-shells and thus no moment, the localization increases toward the top right corner of the f-block (Fig. 2.6).

At low temperatures hybrization between the conduction electrons and the localized

More localization

Ce	Pr	Nd	Pm	Sm	Eu	Gd	Tb	Dy	Ho	Er	Tm	Yb
Th	Pa	U	Np	Pu	Am	Cm	Bk	Cf	Es	Fm	Md	No

Less localization

Figure 2.6: The degree of localization increases toward to the top right corner of the f-block with increasing Z and additional least electron shielding. The last column is not present as full f-shells have no magnetic moment.

f-electrons increases the effective mass. This leads to *heavy fermion* materials and their effective masses can be very large, up to 1000 times, compared to a free electron gas model. The local moments do not stay uncoupled at all temperatures. At lower temperatures, the delocalized conduction electrons begin to couple strongly with the delocalized moments coupling the moments together. This is known as Ruderman-Kittel-Kasuya-Yosida (RKKY) interaction that can lead to ferro/anti-ferro magnetic ordering within the heavy fermion at low temperatures [85].

2.5 Half Heusler Alloy

The structure of Heusler alloys was first identified by Bradley and Rodgers in 1934 [17], before this Heusler had studied the alloy Cu_2MnSn as it could produce a ferromagnet without the constituent elements themselves being magnetic [42]. The half Heusler alloys (HHA) structure derives from the full Heusler alloy with a formula of X_2YZ. By removing one of the X's from the four atoms we can obtain a half Heusler alloy (Fig. 2.7). HHAs have the same Zinc-Blende structure as $Bi_{1-x}Sb_x$, a well studied TI material, but with the addition of another face-centered cubic (fcc) sub-lattice. The structure is also noncentrosymmetric, as in, the structure is not the same under the transformation of inversion center symmetry. This can be visualized by focusing on the blue atom in figure 2.7 and inverting them to the opposite side of the center of the unit cell, the blue atoms are then mapped to vacant spaces not back to other blue atoms positions.

The elements XYZ in the HHA structure usually come from the (X and Y) transition block and the (Z) p-block of the periodic table. X can also be replaced with the rare earth elements. With a wide range of elements, HHAs come with over 1000 possible
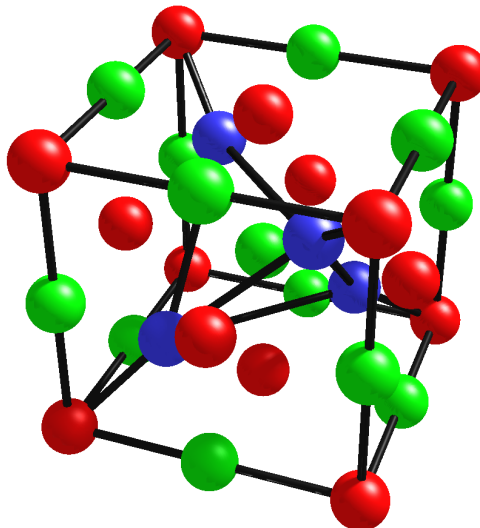
Figure 2.7: Unit cell of a half Heusler alloy. The 3 FCC sublattices at the Wyckoff positions $(0,0,0)$, $(\frac{1}{4}, \frac{1}{4}, \frac{1}{4})$, $(\frac{1}{2}, \frac{1}{2}, \frac{1}{2})$.

combinations, this offers tunability as the properties can be optimized by swapping elements. This can include moving to heavier elements down the table to increase SOC, or across the table to modify the chemical properties and have a greater effect on the band structure. The f-block elements all have similar chemical properties that can be interchanged easily and we have the option to select an element with more or less localized f-electrons, in general, the top right corner, except for the final column are more localized (Fig. 2.6) [24].

Some heavy HHA have been predicted to have an inverted band structure, SOC forces the *s*-like bands to cross over to the lower band to swap the band type (Fig. 2.8)[2]. Many HHA are also predicted to have a zero bandgap where there is a degeneracy as a result of crystal symmetry. A bandgap of the order of $0.1 - 0.5\,\text{eV}$ can be open if the degeneracy is lifted with strain that breaks the crystal symmetry (Fig. 2.8.e). YbPtBi is predicted to have inverted bands but a metallic like band structure, this was found instead to be indicative of a Weyl semimetal.
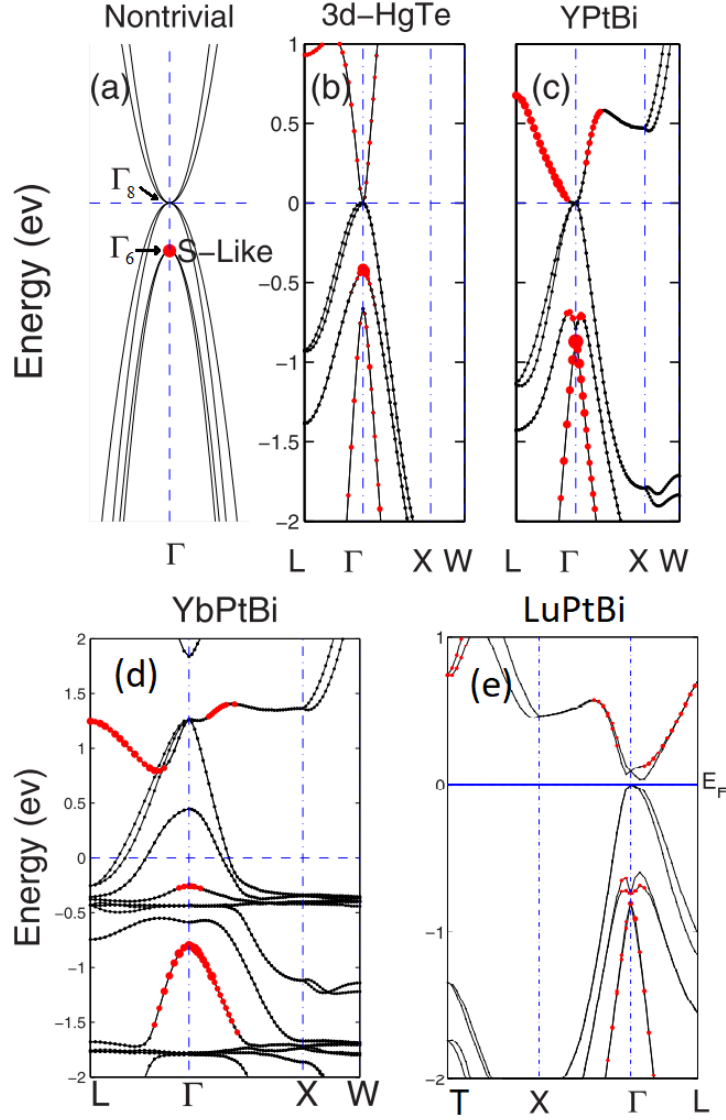
Figure 2.8: DFT band structure calculations of several potential HHA. (a) Non-trivial band structure with a degenerate $\Gamma - 8$ point, the red marks indicate s-like bands. (b) Bulk HgTe Band structure with a clear inverted band .(c) YPtBi with an inverted band. (d) YbPtBi metallic like band structure with band inversion present. (e) LuPtBi strain splitting of the degenerate γ_8 point. Figures adapted from Al-Sawai *et al.*[2]

2.6 Summary

In summation we have covered the background theory for understanding Bi/Ni Bilayers and HHA. Starting with band inversion we have show the origin of the Chern number as it relates to the Berry flux from monopoles and non-trivial windings. From there we moved onto the Weyl semimetals, where we saw the presence of a Fermi arcs on the surface connecting Weyl nodes. Then various transport properties are mention in brief including the chiral anomaly related to Weyl semimetals, as well as superconductivity and magnetism. Finally half Heusler alloys are introduced with there wide range of potential elemental combinations and properties. With this knowledge, we looked for signatures of non-trivial topology and separate them from the trivial case.

CHAPTER 3

Methods

Every sample studied within this work started as a blank substrate, usually either Si/SiO_2 or sapphire, onto which we deposit our thin films. We then go through a structure and crystallinity characterization process using scattering techniques and microscopy. Once we understand the structure and quality of the crystalline order we move onto characterizing electronic and magnetic properties of our thin films.

To grow thin films a stream of the desired material, usually single atoms or small clusters, needs to be generated and then to land onto a substrate. There are many potential sources such as thermal evapouration, pulsed laser deposition, molecular beam epitaxy, wet chemical deposition and amongst others. For this work, we used DC magnetron sputter deposition. Sputtering is a fast, inexpensive and highly flexible process of eroding a target material to generate a stream of mostly neutral atoms and clusters.

Once a sample has finished being deposited, we move onto the characterization. For optimization purposes we are interested in the structure of the thin film, a well ordered crystal and clean interfaces were highly desirable. Optimization was not the only concern, for the study of Bi/Ni we were interested in how an initially clean interface would degrade over time. The structure of a thin film can be determined by either scattering techniques or microscopy. Scattering techniques have a large range of length scales over which they are sensitive, they can tell us about the thin film structures of > 100 nm or atomic crystal ordering ≈ 1 Å. Scattering techniques can only measure the ensemble average of these properties.

Microscopy on the other hand can directly image the structure, although limited in most cases to resolution above the atomic scale. Scanning Electron Microscopy (SEM) and Atomic Force Microscopy (AFM) are readily available techniques with resolution of ≈ 10 nm, microscopic defects or structures can be seen, such as the shape and density of thin film islands. To go beyond this resolution limit Transmission Electron Microscopy (TEM) is needed; TEM is unfortunately not as freely accessible as SEM or AFM. With TEM atomic resolution is possible as well as chemical analysis.

Once a sample is known to have the correct crystallinity and/or thin film structure we could start measuring properties of our thin films. We extensively used magnetrometry and low temperature electron transport techniques to measure the thin film properties. Magnetrometry is well suited for measuring magnetic moments and superconducting messier loops. Low temperature electron transport can tell us about

a wide range of properties like electron/hole scattering, carrier density, magnetism, superconductivity and even information about the band structure and topology.

3.1   Sputter Deposition

3.1.1   Sputtering

Sputtering is the process of ejecting atoms or clusters of atoms from the surface of a material when impacted by high energy particles. The high energy particles are usually ions, and in particular ionized Ar, that have been accelerated by an electric potential applied to the target material. To generate the Ar ions and accelerate them to high enough energy for sputtering we ignite a plasma above the target material. Argon is a useful sputter gas as it is nonreactive, inexpensive and is available in high purity, the disadvantage is that the first ionization energy is one of the highest of the noble gases making plasma ignition harder. Reactive gases can be added to the argon atmosphere such as nitrogen to have them incorporated in the thin film, the process is called reactive sputter. The reaction takes place throughout the sputtering process from reaction of the target source, in transit through the sputter atmosphere and once on the substrate. Reactive sputter is used extensively to grow TaN as it is an effective electrical insulator capping layer to prevent oxidation.

It is possible to only use electric fields to accelerate the ions toward the target but the plasma will be diffuse and difficult to sustain. Once a plasma is ignited more Ar ions are created by the collision of electrons and neutral Ar atoms. To ignite and sustain the plasma a higher argon pressure would be needed. This can be fixed by using a magnetic field to confine the plasma close to the surface of the target. The magnetic field has very little effect on the positive Ar ions as they are accelerated toward the target as they are substantially more massive than electrons. The electrons are deflected toward the surface of the target and trapped in circular motion just above it. During a sputtering event, electrons are also ejected from the target, without the magnet array these electrons would be lost as they are accelerated out of the sputtering plasma. The confinement increases the number of scattering events between electrons and the argon sputter gas allows the magnetron sputter source to operate at a lower potential voltage and lower pressures.

When an Ar ion is incident on the target, there is a transfer of momentum by a
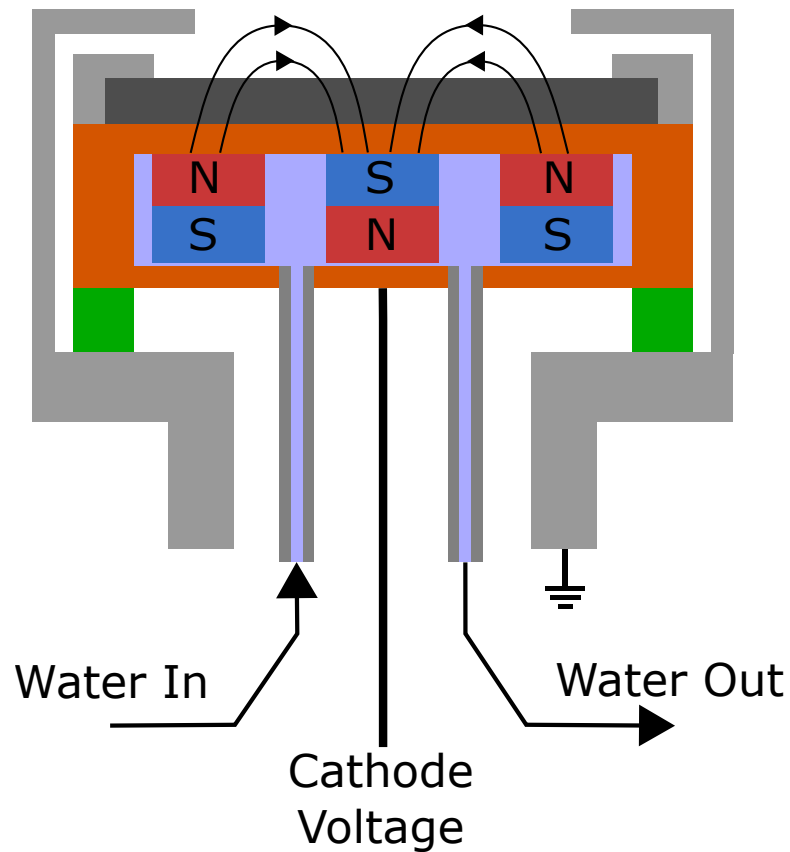
Figure 3.1: Simplified depiction of a cathode magnetron source. The target (dark grey) is placed on a copper cooling block (orange) that holds a magnet array. The copper part is electrically isolated from ground by an insulator (green)) so that a large negative voltage can be applied. Plasma is confined by the magnetic field near to the surface of the target.

cascade of collisions some of which eject material from the surface. The sputter yield is expressed as the quantity of sputtered material for each impacted Ar ion. For very dense targets with lightweight impacting ions there is a large transfer of momentum at each collision, so only a few collisions can take place before the ion comes to rest and so the number of opportunities for ejecting atoms of the target material is limited. The sputter yield is then low.

With a lighter target element and/or heavy ion, collision cascade is an effective model for a target with a high melting point. Since the ions are more massive there is less transfer of momentum at each collision. For this process very many collisions take place with some of the collision pathways ejecting atoms, the sputter yield is similarly increased. The final model is the thermal spike for heavier ions or low melting point targets. At the point of impact enough energy is dissipated to melt a small portion of the target of which some is vapourized as ejected atoms. The thermal spike has a higher sputter yield than a collision cascade process. Out of the sputter targets used in this work, only Bi is likely to experience the thermal spike process as it has a low melting point, as evidenced by its higher sputter rate.

Co-sputtering uses multiple sputter sources to form a mixed sample with variable composition. While it is possible to make and sputter an alloy target with the stoichiometry needed in the final sample, there is no guarantee that this stoichiometry will be preserved. The process can selectively sputter some of the elements faster than others, as well as the interaction with the sputter gas as heavier atoms and clusters are less impeded. If the conditions were right for the correct stoichiometry to be deposited on the substrate there is still no certainty of it being preserved under all conditions, heating the substrate to get good quality crystallinity also increases the vapour pressure of the adatoms possibly to the point that material loss shifts the stoichiometry. With co-sputtering, the composition is vastly more tunable by changing the power to each source at the expense of increased complexity.

The pressure distance product measured from the source to the substrate is an important variable in the thin film growth process; the product is usually given as units of *cm Pa*. Sputtered atoms initially travel through the vacuum chamber ballistically, colliding with the sputtering Ar gas and losing some energy. The higher the product the higher the expected number of collisions before the sputtered atom reaches the substrate. At each collision, the adatoms lose energy until it has reached thermal
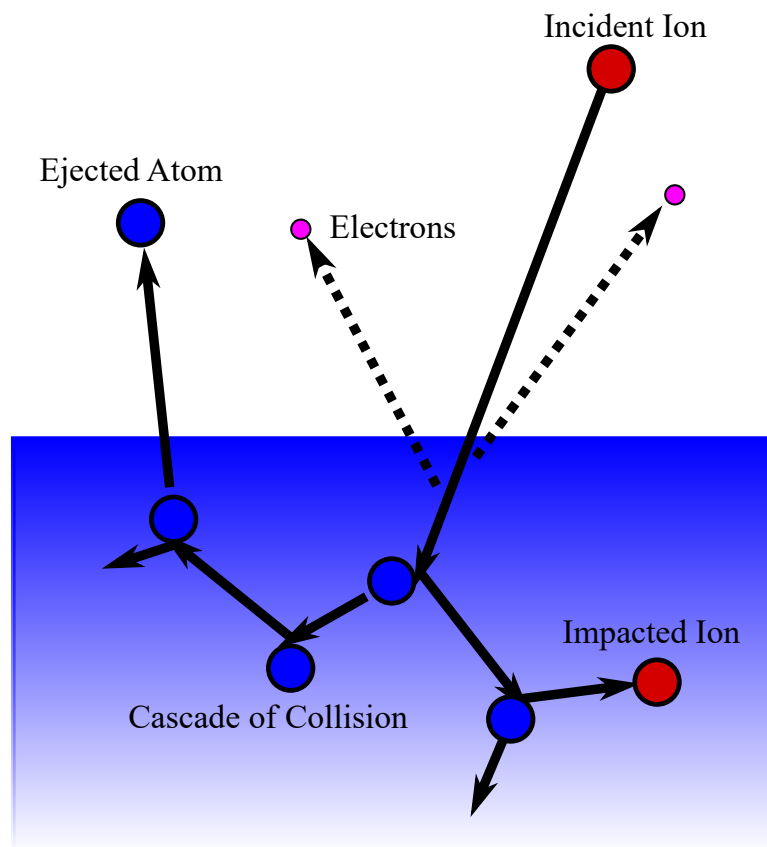
Figure 3.2: Collision cascade for sputter process. Impacting ions implant themselves and eject atoms, secondary electrons are also released.

equilibrium. Once at thermal equilibrium the sputtered atoms move by diffusion instead of line-of-sight, drastically reducing the growth rate of the sample [84]. As the pressure distance product increases, the mean energy of the sputter adatoms onto the substrate surface reduces [69].

3.1.2 Thin Film Growth

Epitaxial Growth

In epitaxy, the thin film lattice and substrate surface lattice matches such that the long-range ordering of the single crystal substrate is inherited by the thin film (Fig. 3.3). The difference between the lattice spacings is given as a percentage mismatch $= \frac{a_{Film} - a_{Sub}}{a_{Sub}}$, the mismatch difference cannot be more than $\approx 10\%$ or epitaxy will not occur [74]. Since perfectly matching films and substrate pairs are rare there will almost always be some strain present, the effect of which must relax at some critical thickness as defects. Typically the disorder is a lattice dislocation where a unit cell is added or removed leading to an abrupt end to a crystal plane. Even if a well matched film and substrate pair can be found it can still be complicated by the presence of other processes, the chemistry between the surface and the adatoms could be weak, the match of the lattice planes is not always unique causing twinning, other undesirable crystal phases may be more thermodynamically stable and many more factors that can affect the epitaxial quality.
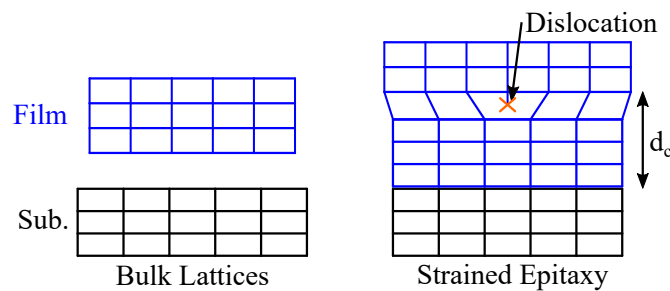
Figure 3.3: For closely matched lattice spacings the film grows onto the substrate such that all the lattices line up and the film inherits the long-range ordering of the crystal. If the strain is present when aligning the substrate there will be some thickness over which the strain relaxes as a defect, usually a dislocation.

HHA which concerns this work have typical lattice constants of 6.6 Å and we wish

to find a good substrate to grow them epitaxially. Nb has a lattice constant of 3.3 Å, nearly half that of many HHA of interest in this work, and is known to grow epitaxially on c-plane Al_2O_3 along the (111) plane [110]. Thus we chose c-plane sapphire for the majority of heated growths. The HHA has two options for alignment with the (011) plane of the cube lying along the a-plane or m-plane. The lattice mismatch for the a-plane is 12.6% and for the m-plane 2.5%. Thus predicted and later observed only alignment for the m-plane exists.
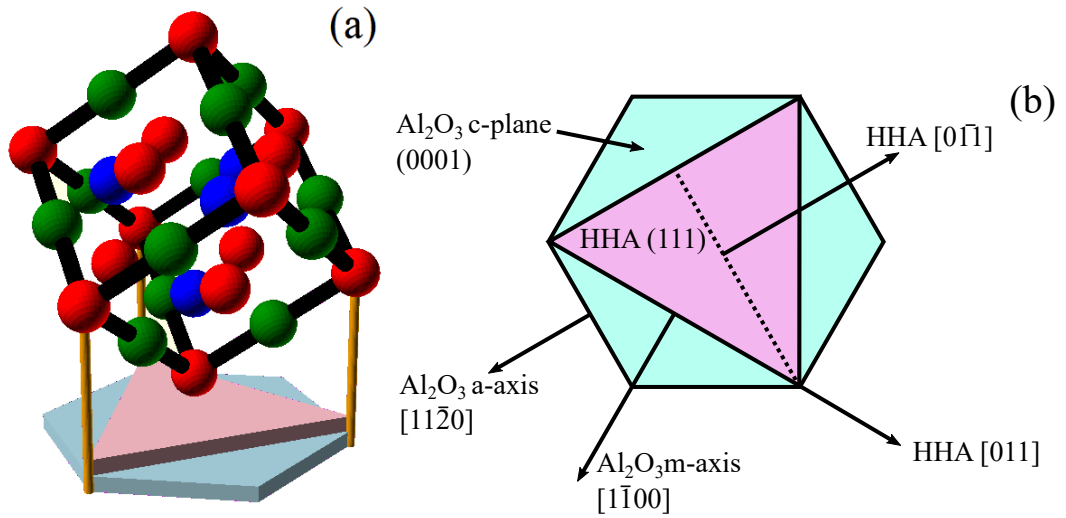
Figure 3.4: (a) The (111) plane of a HHA has a similar size and the same symmetry as the hexagonal c-plane sapphire surface. (b) Top down view of the surface of the substrate with labels for the relevant crystal directions and planes.

This had also aligned the $(1\bar{1}0)$ plane with the sapphire a-plane, so we would expect in-plane x-ray diffraction to see a near $0°$ ϕ difference between the two crystal planes (Fig. 3.4). To achieve a high degree of epitaxy surface reconstrucuting is offten used, reconstructing the surface of the Al_2O_3 would be ideal but requires temperatures higher than is available in our sputter system [35].

Thin Film Growth Modes

Adatom-surface and adatom-adatom attraction dictates the growth mode of the epitaxial thin film. Figure 3.5 has the three primary growth modes depending on the strength of the different attractions. For stronger adatom-adatom attraction than to

the surface, the film will grow as islands with adatoms moving along the surface until it has reached an island of other adatoms or a suitable nucleation site. For strong adatom-surface forces, either layer by layer or Stranski-Krastanov growth can occur. Layer-by-layer has each successive layer complete before the next. Stranski-Krastanov growth (SK), has initial smooth layers formed but at some critical thickness transitions to island growth. The critical thickness for the transition is dependent on strain and chemistry between the adatoms and the surface.
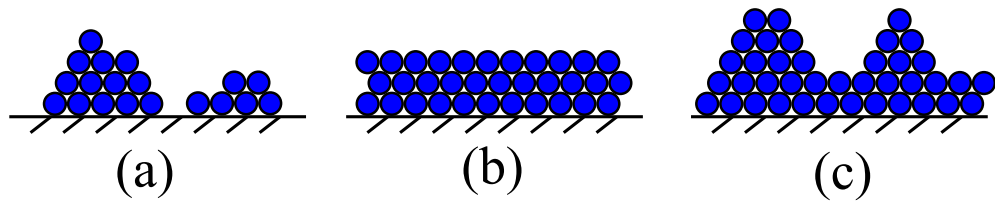
Figure 3.5: (a) Island growth,(b) Layer-by-layer growth,(c) Stranskiâ€"Krastanov growth.

Thin Film Structure

Thin film structure is dependent on many parameters, figure 3.6 only has axes for the substrate temperature and ion energy. These are not the only important parameters but it is not feasible to plot every possible parameter and project the n-dimensional graph to a 2D image. The figure is a guide to how a film may be expected to grow as an approximation. Temperature is important as it freezes different mechanism. At low temperatures relative to the melting point of the film, T^*, the film is in zone 1 (Fig. 3.6). Here the adatoms have very little motion and small crystallites can form. It is important to realize, particularly for the Bi/Ni bilayers chapter, that substrate temperature and melting point need to be compared on an absolute scale as room temperature can be a significant fraction of the melting point.

At $T^* \approx\, > 0.5$ adatoms have greater mobility and can move into lower energy crystal positions and grow larger crystallites into larger grains. These are at the zones T, 2 and 3 each have progressively larger crystal grains. The T zone has thin tall grains that are vertically aligned but not continuous across the entire film thickness. Zone 2 now does have continuous grains throughout the thickness of the film and has grown wider as well. Finally, zone 3 is the start of large grains approaching bulk-like properties. We
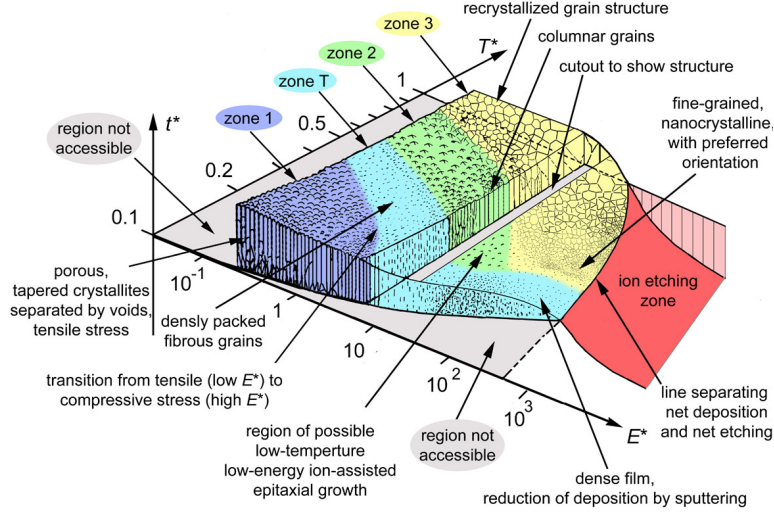
Figure 3.6: Extended Thornton structure zone model of temperature and ion energy with the vertical axis as the effective thickness, Figure from [5]

were aiming for there to be epitaxial growth, which will happen mostly within zones 2 or 3. There are few measurements of the bulk melting point of HHA, but YbPtBi has had its melting point measured around 1050 K so we needed temperatures greater than about 500 K [66].

The ion energy is also important, depending on the target element the sputtered atom energy can be in the range 0.1-100 eV [37]. This energy is not high enough for etching, but some resputtering can occur and can lead to ion-assisted epitaxy as well as reducing the thickness and possibly altering the stoichiometry from preferential sputtering. Since sputtering takes place inside an Ar atmosphere the pressure distance product can give time for sputter atoms to be slowed by collisions. Thus the ion energy is a proxy of the Ar pressure as the distance to the substrate is fixed and increasing the pressure distance product decreases the mean ion energy seen by the thin film.

3.1.3 UHV Co-Sputter Deposition system

We used a custom UHV sputter deposition system built here at the University of Leeds to grow all of the half Heusler Alloys study in this work (Fig. 3.7). The Bi/Ni bilayers are grown in a different vacuum chamber better suited for multilayer deposition as described in the Bi/Ni bilayers chapter, the system described here is optimized for

fine tuned alloys and heated growth. The sample throughput for the UHV system is limited compared to the multilayer system with its 24 sample spaces and full automated control.

The system has two vacuum pumps. A diffusion pump was used for the primary pumping of the main chamber with an additional liquid nitrogen Meissner trap placed above it for additional pumping of high vapour pressure gases. The Turbomolecular pump is used on the load-lock where it is an ideal high vacuum pump as it can start and stop faster than a diffusion pump but still achieve the high-quality vacuum needed not to contaminate the main sputter chamber when moving samples inside. With a load-lock, the main chamber did not need to vent to ambient pressure to exchange samples.

By having all copper gasket seals instead of viton o-rings, except for the continuous water-cooled sputter sources which use low out-gassing Perfluoroelastomer o-rings, the system can be baked to remove absorbed water vapour from the walls of the chamber. Additionally several of the elements used as sputter targets are effective getter materials that will react with and trap the residual gas, further reducing the base pressure. The sputter sources cannot be exposed to bake temperatures and unfortunately must be water-cooled during the bake. As these sources remain at room temperature during the bake, they keep the adsorbed water vapour and become a major source of outgassing after baking.

Four sputter sources from Angstrom Sciences were mounted on the top flange pointing downward toward a UHV design heater stage holder. Each of the four sources is confocal to the sample position and placed approximately $10.5\,\mathrm{cm}$ away from the sample. The typical sputter pressure to maintain a consistent plasma is $5 \times 10^{-1}\,\mathrm{Pa}$, the pressure-distance product is thus $5.25\,\mathrm{Pa\,cm}$. The pressure distance product to thermalize a target element is positively correlated with its molecular weight. The lightest element used within this sputter system to grow HHA was Y. We can compare Y to Mo, only 3 atomic numbers higher, which has a previously measured pressure distance product for thermalization of $10\,\mathrm{Pa\,cm}$ and conclude that Y and all heavier elements are within the ballistic region [69].

The heater stage holds the molybdenum sample plates in position at the focal point of the four sputter sources. The heating element is made of Ta foil coated in a yttrium oxide. It can heat the sample up to $800\,^\circ\mathrm{C}$. The contamination shields prevent
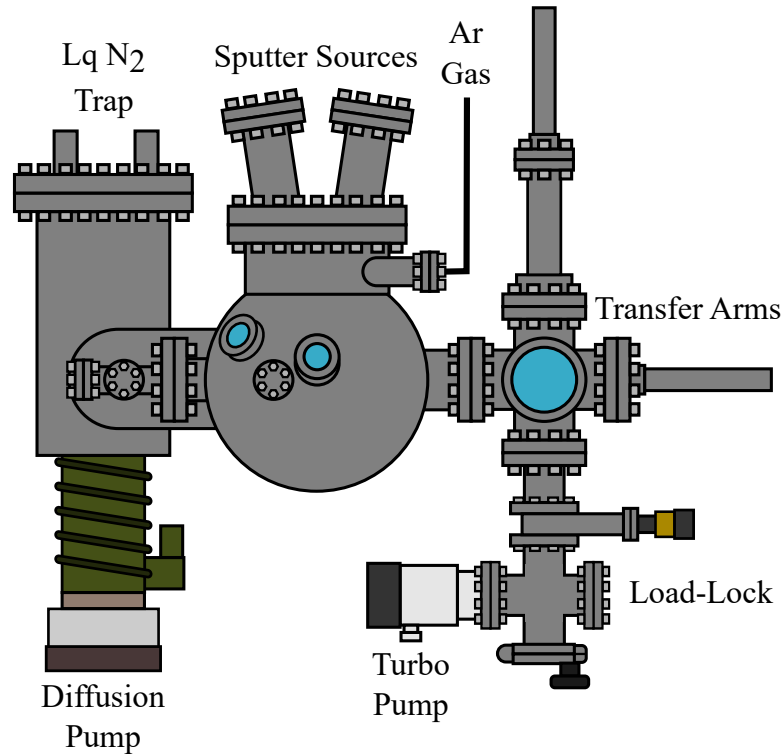
Figure 3.7: Simplified diagram of the sputter system used for the HHA growths. Backing pumps for the diffusion pump and macromolecular pump are not shown.
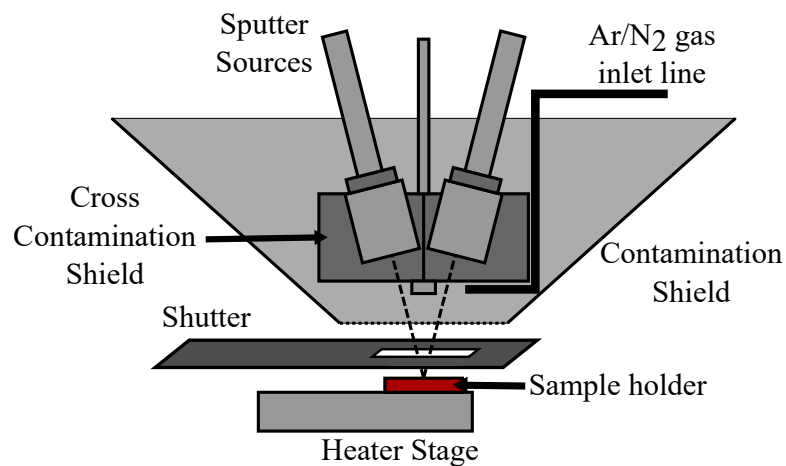
Figure 3.8: Simplified diagram of the sample heater stage, the sputter sources and the shutter. The sputter sources are shielded from depositing on each other and the walls of the chamber. The shutter is moved with a linear motion metal bellows.

depositing material from one source to another, they also prevent deposition into the chamber walls. The shields can be easily removed for cleaning, without the shields the deposited material would be difficult to remove from the chamber walls would trap gases when vented for maintenance. The sputter gas is directed near to the front of the sources where it might act to increase the plasma stability from an increase in localized pressure.

The typical growth rates during sputtering were 0.3-0.7 Ås^{-1} and at the stated base pressure the monolayer deposition time was of the order of $100\,\text{s}$. This is where sputtering is advantageous over MDE or thermal evapouration which typically have longer deposition times; sputtering has a high deposition rate and is then less sensitive to base pressure contamination.

3.2 Reactive Sputtering: Tantalum Nitride

By introducing N_2 into the Ar sputter atmosphere we could react our sputter material to form nitrides. This is known as reactive sputtering and the sputter system was setup to use both N_2 and O_2 as well as the normal Ar gases. Ta metal is a somewhat resistive metal compared to most metallic thin films, until its superconducting transition temperature at $4.4\,\text{K}$, and excellent capping layer to prevent oxidation. But our HHA films have higher resistivity from the low carrier density and a Ta cap would short the electrical current. To solve this we capped our HHA with TaN by reactive sputtering. The resistivity of pure Ta is not an issue for the Bi/Ni bilayers as we were interested only in the superconducting properties, and Ta grown as a thin film cap ($< 10\,\text{nm}$) is not superconducting at our measurement temperatures.

The reactive sputtering of a pure Ta target was optimized to find the best conditions for both ease of sputtering and high resistivity. Figure 3.9.a has the sputtering voltage as we increased the N_2 pressure, if this were to increase too far the sputter plasma would become unstable and difficult to maintain. The electrical resistivity of our TaN capping layers is orders of magnitude greater than the most resistive HHA thin film measured when the Ar sputtering atmosphere is above 30% N_2 (Fig. 3.9.b). When using this capping method the electric current flowing through the cap will be negligible.
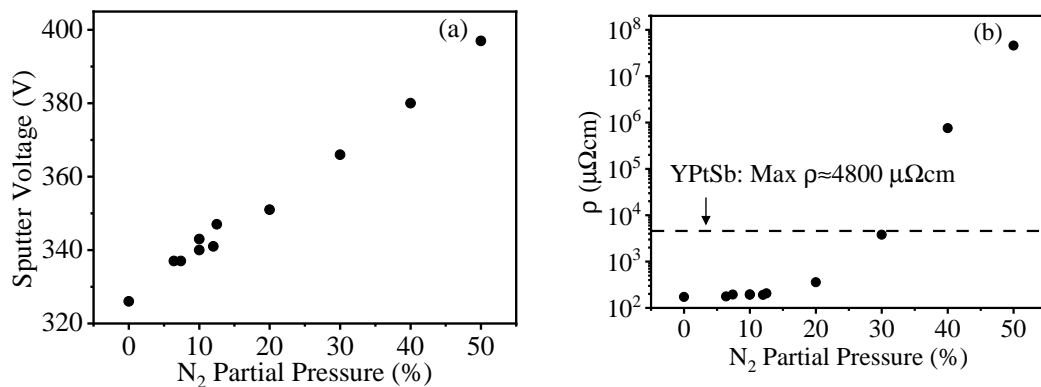
Figure 3.9: (a) The applied cathode voltage to the sputter source at increasing N_2 partial pressure when reactively sputtering Ta to make TaN. (b) The Resistivity as a function of the N_2 partial pressure, line indicates the maximum YPtSb resistivity measured.

3.3 Scattering Techniques

The scattering used within this thesis uses either Bragg reflections or specular reflections scattering off different features and at a wide range of length scales. These two reflection types are similar but importantly the refractive index is important for specular reflection but not Bragg diffraction. The relation between the angle θ, wavelength λ and length d is described by momentum transfer, Q , in equation 3.1. At low 2θ angles the corresponding length scale, d, is large compared to the wavelength used ($\approx$100-10 nm). This is useful for characterizing thin film structure as the interfaces between the layers are typically separated by those lengths. If repeated thin film layers or multiple units cells are present then Bragg diffraction can occur, similar to Bragg diffraction of crystal planes. We can simulate thin film layers with a software called GenX. For higher 2θ angles, d approaches the lattice constants of many crystals ($\approx$10-1 Å) and can be used to examine the structure at the atomic scale.

$$d = \frac{2\pi}{Q} = \frac{\lambda}{2\sin(\theta)} \tag{3.1}$$

The Scattering Length density (SLD) is the product of the density of a material and the intrinsic strength of the scattering interaction with the materials constituent elements. For x-ray scattering the scattering strength are strongly dependent of the Z

number of the element, heavier elements typically scattering elements more than lighter ones. For neutrons that have no charge, the scattering strength depends instead on the nuclear interaction cross-section.

The SLD for neutron reflectometry is dependent on the magnetization strength and orientation. An up neutron will interact more strongly with an anti-parallel magnetic field than for a parallel one. The asymmetry in the up and down neutrons is proportional to the total magnetic moment in the sample.

3.3.1 X-ray Scattering

The instrument used to preform x-ray scattering was a Bruker D8 discovery diffraction, unless otherwise stated. The x-rays are generated by a 40 KeV 40 mA x-ray tube using a copper block as a source of primarily the Cu-Kα at 1.5406 Å as well as other Cu peaks and Bremsstrahlung radiation. The equipment has additional filter to remove the Bremsstrahlung radiation and the undesired Cu peaks. Bragg's law for crystal lattice diffraction is identical to the momentum transfer equation as before but d is the separation between the lattice planes accounting for the (hkl) miller indices (Equ. 3.1). We calculate the allowed Bragg peaks and their intensities using the powder x-ray diffraction simulations software PowderCell [53].

Our samples are all macroscopically flat thin films with a defined surface normal vector. The orientations of the sample surface normal relative the reflection plane, the plane of specular reflection, can be broadly separated into either out-of-plane or in-plane scattering. This is particularly of interest to epitaxial thin films as the lattice constant and observable miller planes changes as we move bewtween these two orientations. While the out-of-plane direction is easier and quicker to measure owing to the higher intensity of the diffraction peaks and easier alignment, the in-plane components are essential to verify the epitaxy of the thin film at the cost of lower intensity and greater time investment.

Out-Of-Plane XRD

The Bruker instrument uses a Bragg-Brentano geometry with a monochromatic super mirror before the sample to reduce the intensity of all x-ray wavelengths that are not close to the Cu K-α peaks. The monochromator is very effective at removing Bremsstrahlung radiation but only marginally reduces the intensity of the Cu K-β

peak. To further reduce Cu K-β a Ni filter is used. Ni is the element before Cu and as such has an absorption peak at the Cu K-β peak.
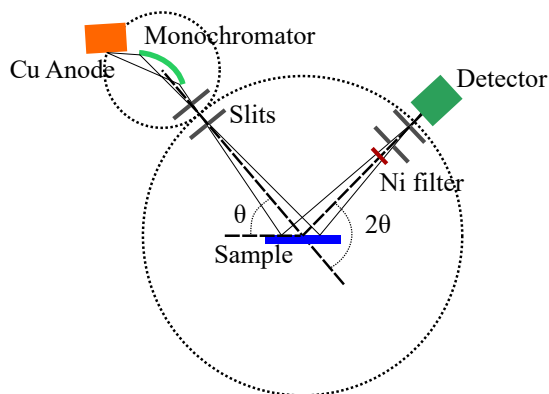
Figure 3.10: Diagram of the x-ray optics of the Bruker diffracometer. The dashed lines are the goniometer circles, each represents the line on which the x-rays are focused and where the slits and detector were placed.

The dash circles are the points at which x-rays are focused (Fig. 3.10). To be fully focused the sample would also need to be curved but a flat surface roughly approximates a short arc of a circle. By placing each instrument at this circumference the intensity and angular resolution were maximized. This setup is the typical way in which out-of-plane XRD and XRR measurements were taken. For in-plane, we still use the same setup as out-of-plane but we introduce additional rotations, χ and ϕ, to the sample.

In-Plane XRD

Figure 3.11 defines the angle χ as the angle between the surface normal of the sample and the θ /2θ reflection plane. At $\chi = 0°$ the sample is out-of-plane and at $\chi = 90°$ the sample is in-plane. The angle ϕ when $\chi = 0°$ principally changes nothing about the reflection, only at $\chi > 0°$ and importantly near 90° does ϕ become important. In this case, ϕ acts similar to the angle θ and by rotating around this axis we observe the repetition in the thin film.

The Bruker instrument as originally delivered did not fully support in-plane measurements. With the addition of two extra rotation stages, ξ and ζ, in-plane measurements become practical. In principle, the ξ and ζ axes are redundant as any angle of the sample can be achieved with the original three axes of rotation. The additional axes
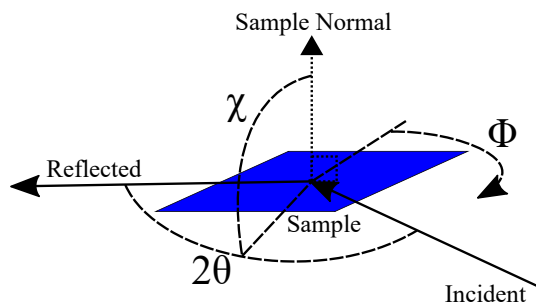
Figure 3.11: Diagram of the relevant angles and geometry of the in-plane measurements.

were there to align the sample surface normal with the original axes. Without these additions, complex multi-axis rotations and alignment would be needed to correctly scan across the intended axis. While in-plane measures are very informative for epitaxy, they are also more difficult to measure. Since the beam only glances the surface, x-rays become attenuated quickly deeper into the film. The effect of which makes in-plane a surface-sensitive only measurement and reduces the intensity of the diffraction peaks as a result of the reduced scattering volume. As such the signal to noise ratio is worst for in-plane.

X-ray Reflectometry

The data from either x-ray or neutron reflectivity encodes information about the SLD profile of the thin film. For simple single layer films, Keissig fringes have a well known analytical solution, each peak (m) in the reflectivity curve is separated from other peaks by an angle (θ) inversely proportional to the thickness (t) of the film (Equ. 3.2). These are particularly useful for calibrating the sputtering rate of a target. Unfortunately, complex reflectivity curves from films with multiple layers cannot be constructed from simple single film components. Instead reflectivity fitting software is used (Ch. 3.3.4).

$$\theta_{m+1}^2 - \theta_m^2 = \frac{\lambda^2(2m+1)}{4t^2} \tag{3.2}$$

3.3.2 Polarized Neutron Reflectivity

Typical x-ray reflectometry can measure the structure of a thin film but it has limitations, it is sensitive to the roughness, does not include magnetization information and some elements can have similar x-ray contrast. Neutrons contain a magnetic dipole and

are sensitive to magnetization of the thin film. Neutron reflections are done at lower angles where the roughness of the thin film is less disruptive and has a different set of cross-sections so similar contrasting elements in x-rays maybe have better contrast with neutrons[1]. Protons and electrons also have magnetic dipoles along with electric charge. Also both are easy to obtain in an unbound state and manipulate with electric and magnetic fields. Unfortunately, protons and electrons can not be used for reflectometry as the Coulomb scattering cross-section limits severely the penetration depth.

3.3.3   ISIS Beamline: PolRef

Free neutrons are not readily available to use for reflectivity and are charge neutral so they cannot be accelerated with electric fields or deflected by magnetic fields. The source of neutrons at the ISIS beamline facility is a spallation target source. Pulses at $50\,\mathrm{Hz}$ of high energy protons are accelerated into a tungsten target which causes spallation. The energy of the proton beam ($800\,\mathrm{MeV}$) is comparable to but less than the binding energy of the tungsten nucleus ($\approx 1500\,\mathrm{MeV}$). Spallation does not knock off protons and neutrons like billard balls. Instead the energy of the proton is adsorbed and a cascade of high energy interactions takes place ($> 20\,\mathrm{MeV}$), the nucleus is left in an excited state and the energy is released as many particles such as protons, electron and neutrons. [86]. Secondary spallation from the higher energy neutrons and protons produces even more particles. Neutrons straight from a spallation target are too high energy for reflectometry. The energetic neutrons are slowed down to lower energies with a liquid methane moderator.

The moderator is then an isotropic radiating source of the neutrons for the PolRef instrument at ISIS (Fig. 3.12). Before reflecting off the sample the neutron beam needs to be conditioned by collimation and filtering of usable wavelengths. The speed of neutron beam used was $4400 - 266\,\mathrm{ms^{-1}}$ which corresponds to a De Broglie wavelength of $0.9 - 15\,\mathrm{Å}$. Spinning chopper wheels at these wavelengths/velocities can move fast enough to allow the correct wavelength to pass through. The T0 detector stops the prompt neutrons that are traveling near the speed of light, this rotates out of the beam path in time for the front of the desired wavelength packet to pass. Successive choppers cut off the trailing neutrons.

---

[1]The contrast issue also applies with the reverse logic and some elements have poor contrast for neutrons but not x-rays
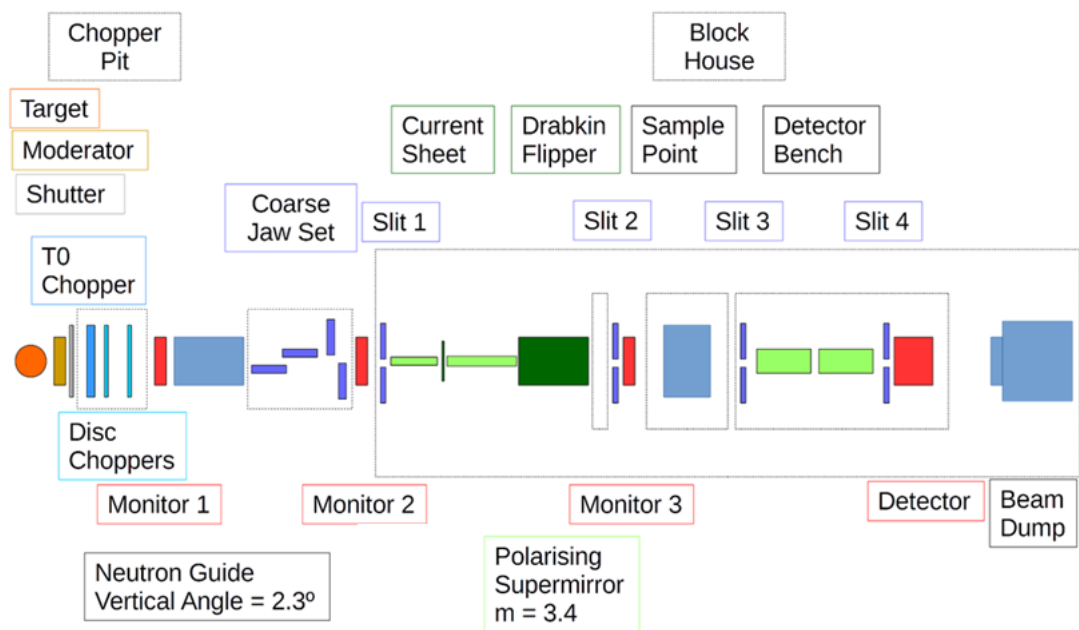
Figure 3.12: Neutron beam path for the POLREF beamline at ISIS. The neutrons are generated by spallation then moderated to lower energy. The wavelength is selected with rotating choppers and the beam narrowed with slits, polarized by a polarizing mirror. Finally the neutrons reflect off the sample and then enter the detector.

For collimation, the sample is placed far away from the moderator and several slits placed far apart are used to narrow the beam to 60×30 mm in height and width. The long distances and comparably narrow slits limit the divergence of the beam to less than $\approx 0.16°$. Several monitors are placed throughout the beam path that intercept a small portion of the neutrons. Since each pulse will not be exactly the same intensity these monitors normalize the detected beam intensity.

To get magnetic information from the reflectometry the beam needs to be first polarized. This was achieved by a polarizing magnetic supermirror where the up and down states have different critical reflection angles and so neutrons in the wrong orientation can be rejected [1]. Additionally, half of the measured neutron pulses needed to be flipped to allow for contrast between the up and down neutron states. The Drabkin flipper is a divergent magnetic field that switches neutrons from up to the down state. To be more accurate, the field orientation is reversed as the center of the flipper goes though zero field, the neutron spin orientation thus changes with respect to the field.

The 1D detector measured both the position of the reflected neutron and the arrival time. From that, the time-of-flight is calculated and thus its velocity/wavelength can be inferred. For our measurements, the detector, which remained at discrete fixed angles, can measure over a range of Q-space by deducing the Q value from the time of arrival and the known distribution of neutron wavelengths.

3.3.4 Reflectometry Analysis Software:GenX

GenX uses the Parratt algorithm to simulate a reflectivity curve from a model SLD profile. The SLD profile is calculated from a box model defined by a set of parameters. The typical parameters consist of separate thin film layers each with a thickness, chemical composition, density, magnetization, and roughness. The scattering strength of each chemical element is known and along with an estimate of the density as a fitting parameter gives an SLD, once intermixing between the layers is added the SLD can be calculated at each thickness interval.

The primary function of GenX is to optimize these parameters to minimize the difference between the real data and the simulated data as measured by the Figure

---

[1]Polarized magnetic supermirrors are multilayer stacks of contrasting refractive index material with layer thickness tuned to constructively reinforce reflection, each layer also has a different magnetization to achieve spin polarization.
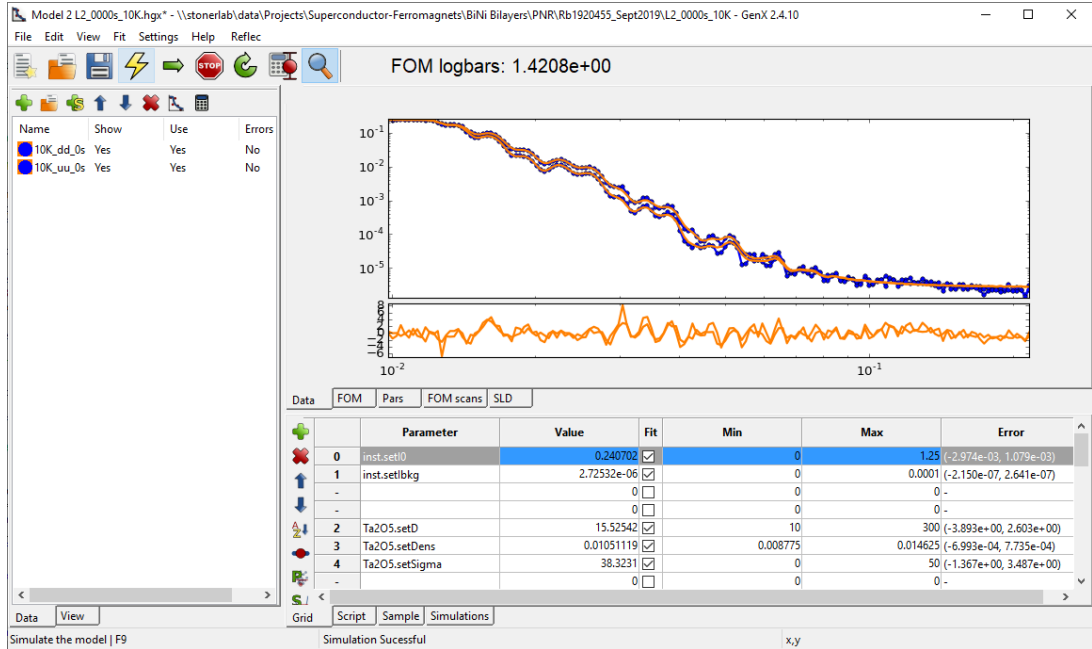
Figure 3.13: A screenshot of the software GenX fitting to data obtained from PNR.

Of Merit (FOM). To do this GenX utilizes a genetic optimization algorithm, an initial population of randomized parameter sets is generated with defined bounds. At each step in the optimization process, the members of the population with the lowest FOM are kept and the worst members are discarded to be replaced by the offspring of the successful members. Additionally, random 'mutations' are applied to the offspring which might further reduce the FOM. Genetic algorithms are better at avoiding being stuck in local minima.

3.4 Nanoscale Microscopy

3.4.1 Focused Ion Beam and Scanning Electron Microscopy

The Focused Ion Beam and Scanning Electron Microscopy (FIBSEM) had two roles in this work. Firstly ion milling and assisted ion deposition to cut and attach a thin cross-section of a thin film to a sample holder for TEM imaging as mentioned later (Ch. 3.4.2). To cut a thin cross-section, thin films were first prepared by deposition of a sputtered Ir layer and then a Pt/C layer by assisted ion beam deposition. The ion beam used gallium ions that were accelerated to high enough energy to mill away matter

instead of being deposited on the surface (Fig. 3.6). Although some ion implantation may occur. Secondly, it was also used to image the surface structure with the SEM. The FIBSEM is part of the LEMAS facility, it is managed and operated by John Harrington.

3.4.2   Transmission Electron Microscopy

The LEMAS facility in the School of Engineering at the University of Leeds provides a Titan TEM to image at the atomic scale. Cross-sectional TEM is a powerful analysis tool allowing the direct observation of the crystal lattice and its relation to the substrate. SEM is limited in resolution as the large volume over which electrons and x-rays are generated, transmission is only sensitive to direct absorption and can achieve higher resolution. Electron transmission is limited to penetration depths of a few 100 nm so to get a cross-section image, FIBSEM is needed to cut out a thin section. The Titan TEM features an energy-dispersive x-ray spectrometer (EDX) for composition scanning across and through the thin film. With this, we could measure if the film is epitaxial, the stoichiometry, grain sizes, etc. The Titan TEM is managed and operated by Dr Zabeada Aslam.

3.4.3   Atomic Force Microscopy

Atomic Force Microscopy (AFM) uses a sharp tip that is close to the surface and scans over it to produce an image. Figure 3.14 contains a diagram of the AFM tip setup. The tip is static with respect to the instrument, instead the sample is moved by piezoactuators. The tip is on a cantilever which deflects under an applied force, the forces involved are an attractive Van Der Waals forces further away and then short-range Coulomb repulsive contact force. The cantilever deflection is measured by a laser reflecting off the back of the cantilever onto a quadrant photodetector, the laser light is aligned in the center such that the photodetector voltage bias from opposing sectors is near zero. While the tip could be dragged along the surface maintaining a constant deflect in a mode known as contact mode, that can damage the tip or the surface, we instead use an alternative called tapping mode. AFM tips are made with resonance frequency with a certain range 100-300 KHz, by oscillating at this resonance the AFM tip will 'tap' the surface periodically. Tapping the surface dampens the amplitude of oscillation so it is used as the feedback to control the height. All AFM images taken were in tapping mode as it works well for steep edges such as those found on growth

islands.
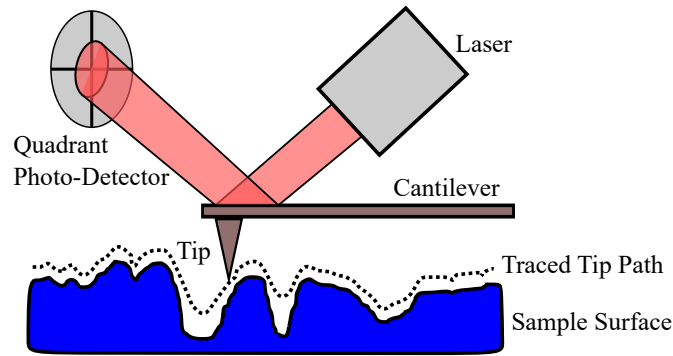
Figure 3.14: Diagram of an AFM tip and reflected laser path. Laser light reflects off the back of the tip, the tip is static and the sample is move by piezoactuators. Surface features exaggerated.

Ideally the AFM tip would be atomically sharp and thin. This is not possible with current manufacturing techniques and so the tip limits the resolution of the image. The tip profile and also debris that is adhered to the tip form a convolution with the surface. Debris on the tip can superimpose copy images of the debris on to the sample. If many similar looking objects appear in the image it may be an issue with the tip. The ability to fit the tip through narrow and deep holes is limited, this is illustrated in figure 3.14 where the traced tip path cannot reach the full depth of the holes. The result makes sharp edges sloped and holes less deep.

3.5 Low Temperature Electron Transport

3.5.1 4-Point AC measurement

All transport measurements within this thesis are 4 contact resistance measurements, and increased to 5/6 when measuring the Hall effect at the same time (Fig. 3.15.a). Ideally a Hall bar geometry would be used to measure the resistivity and Hall effect, but this was not easily available. So we utilize techniques to mitigate geometric effects. The resistivity of a thin film is calculated from the Van der Pauw method which is a technique to cancel out geometric effects of the resistance by swapping contact points [100]. As Hall effect is directly related to the current between the contacts and by assuming a large majority of the current will pass nearer the centerline, as long as

the Hall contacts are close to opposing edges of the sample the measured voltage will be very close to correct value. Additionally because the Hall effect and MR are anti-symmetric and symmetric respectively, the signal, $V(B)$, from the voltage contacts can be decomposed into the symmetric/anti-symmetric compounds using equations $V_{sym} = \frac{1}{2}(V(B) + V(-B))$ and $V_{asym} = \frac{1}{2}(V(B) - V(-B))$ respectively. Doing this removes any cross contamination of the signal from misaligned voltage contacts.

DC constant current and a voltmeter in a 4 contact type geometry could be used to measure the resistance of a sample with reasonable precision, but AC can improve upon this. For AC measurements an alternating current is applied to the sample and a lock-in amplifier to measure the voltage response from the sample. This geometry works well assuming a uniform current distribution.
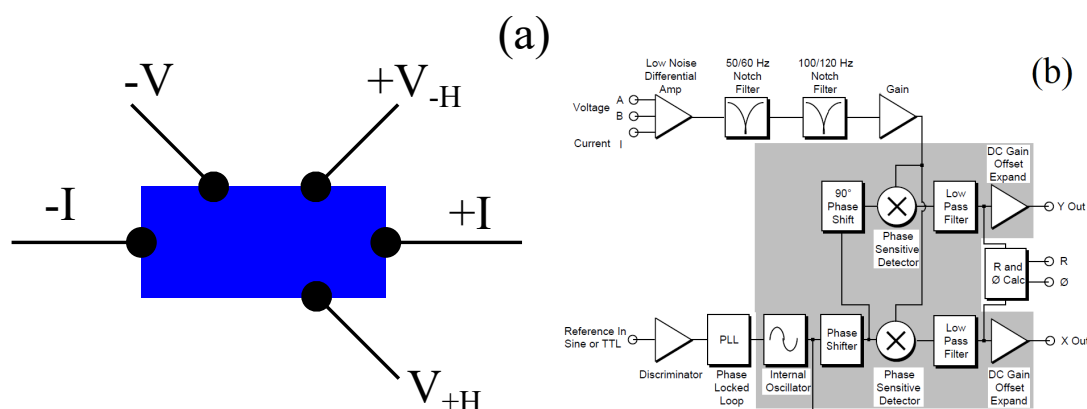
Figure 3.15: (a) Five point contact geometry for simultaneous measurement of resistance and Hall effect. (b) Functional block diagram of the internal process for a SR830 lock-in amplifier, diagram from manual. The SR830 has an impedance of $10\,\text{M}\Omega$ compared to our sample resistance of 100-1000 Ω.

Lock-in amplifiers read in both a voltage signal from the sample and a reference frequency from the current source, in our case we exclusively use a Stanford SR830 lock-in amplifier (Fig. 3.15.b). First, the signal is amplified and two notch filters are applied at 50 Hz and 100 Hz for reasons discussed later. Then the signal and reference are digitized into a 24-bit number. The signal and reference are multiplied together in a phase-sensitive detector (PSD) and then run through a low pass filter with a selectable time constant. By moving the measurement frequency from 0 Hz in the case of DC to some high frequency we can eliminate the 1/f noise and form a narrow band filter

around our measurement frequency. Any noise not at the correct frequency will be averaged by the time constant filter. This works as when two sine waves are multiplied together, only when the frequencies match will it produce a net positive value over many oscillations. Mismatched frequencies will move out of phase and when averaged over many oscillations have a net-zero response. Since any signal can be perfectly reproduced by an infinite series of sine functions as a Fourier series this applies to any signal+noise. The whole process is repeated again with a $90°$ phase shift to get the out-of-phase component of the input signal.

Care must be taken when selecting a frequency, avoiding the mains frequency of $50\,\mathrm{Hz}$ is obvious and also the high multiples to avoid mains line harmonics. The SR830 has in build filter tuned to mains frequency for this reason. For this thesis, the frequency is selected such to avoid obvious interference and also avoid capacitive and inductive effects to create an out-of-phase component. This is usually in the range of 70-200 Hz. It is possible to reach noise levels better than 1:10000 with a Lock-in amplifier and good sample contacts.

3.6 Cryogenics

To measure at $\approx 1\,\mathrm{K}$ and above a wet He4 cryostat is used as shown in figure 3.16.a. The term 'wet' refers to direct contact between the He4 cooling gas and the sample. The cryostat has multiple vacuum jackets separating the liquid N_2 jacket and He4 bath from each other, the outside environment and the variable temperature insert (VTI) where the sample is placed. The VTI contains a heater and needle valve, the latter is the source of cooling power as it allows liquid He4 into the VTI. The VTI is constantly pumped on by a vacuum pump that can reach pressures as low as $1\,\mathrm{mBar}$. The cooling power comes from the latent heat of vapourization as the He4 evaporates from a liquid to a gas, the cooling powering is then proportional to the vapour pressure of the He4. The lower the pressure that can be achieved, the lower the temperature. Near $1\,\mathrm{K}$ the pressure has reached the limit of the pump and the rate of cooling falls exponentially. Further cooling would need high vacuum pumps and better thermal isolation.

To resolve this problem and get lower temperatures the working liquid/gas can be changed to the much more expensive He3 isotope. The vapour pressure of He3 is considerably higher than He4 for the same temperature. With a similar setup a He3 could reach a few $100\,\mathrm{mk}$. Unfortunately He3 is far too costly to waste on losses
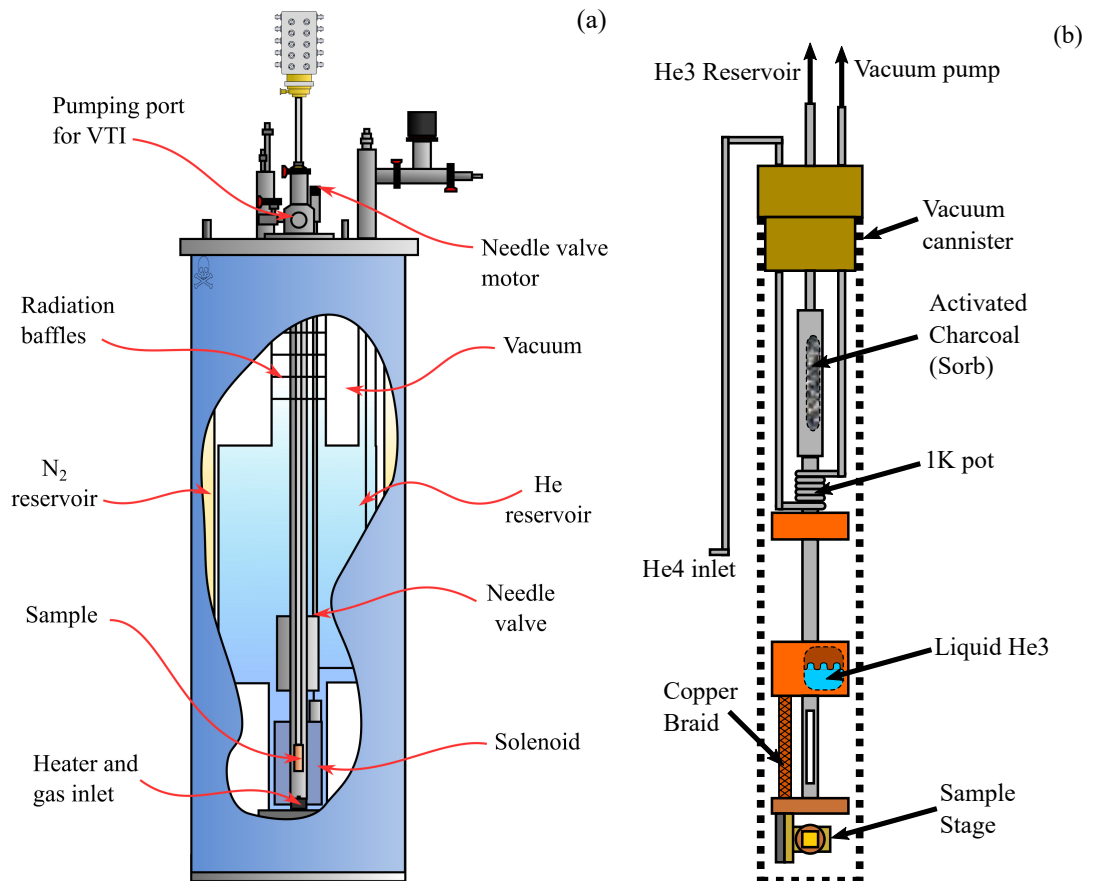
Figure 3.16: (a) Diagram of a wet cryostat with a Liquid N_2 jacket and He4 reservoir [10].(b) Diagram of the Heliox. The internal stack is in near vacuum with some small residual He4 gas for heat exchange above the He boiling point. The He3 is condensed in the evaporation chamber where evolved gas is adsorbed in the activated charcoal sorb section.

from collecting and reliquifying. Instead, the He3 remains permanently sealed within the system and to reduce the pressure, adsorption is used, this system is known as a Heliox. The Heliox is cooled with He4 in a $1\,\mathrm{K}$ pot where the He3 is liquified from a reservoir of gas. Starting with initially unsaturated activated charcoal the adsorption can start. All of the pumping on the liquid He3 comes from the adsorption of He3 vapour into the activated charcoal inside the sorb. The sorb is cooled by the $1\,\mathrm{K}$ pot with an attached heater, controlling the temperature of the sorb controls the pumping speed. As He3 evaporates it cools down liquid He3 pot and also the thermally connected sample stage. With this system temperatures as low as $250\,\mathrm{mK}$ can be reached.

CHAPTER 4

On the Origin of Superconductivity at Nickel-Bismuth Interfaces

The work within this chapter was published in the Physical Review Research Journal along with the co-authors [101]. Nathan Satchell, Christian J. Kinane, Gavin B. G. Stenning, Sean Langridge, and Gavin Burnell assisted in taking PNR measurements with the POLREF beamline at ISIS. Nathan Satchell and Gavin B. G. Stenning also assisted with measurements taken with the Quantum Design MPMS 3 SQUID and Rigaku SmartLab diffractometer at the ISIS R53 characterization Lab.

Unconventional superconductivity has been suggested to be present at the interface between bismuth and nickel in thin-film bilayers. In this chapter, we study the structural, magnetic, and superconducting properties of sputter deposited Bi/Ni bilayers. As-grown, our films do not display a superconducting transition, however, when stored at room temperature, after about 14 days our bilayers developed a superconducting transition up to 3.8 K. Our samples did have a superconducting transition during the earlier phase of our investigation, but during this time the room temperature was elevated due to the summer heat and the lead time between growth and measurement could be a few days. Later into the study, the superconducting transition was no longer present as the average temperature dropped and when samples were measured the day after growth. This led us to the suspicion of room temperature annealing.

Superconductivity and ferromagnetism are normally considered incompatible phases as the strong exchange field of a ferromagnet will act to break superconducting Cooper pairs [36]. It is therefore unusual to find a superconducting transition at about 4 K in Bi/Ni bilayers, when ferromagnetic Ni has no known such superconducting transition, and crystalline Bi is only superconducting below 0.5 mK [80]. Higher critical temperatures in Bi have been reported under certain conditions, for example, $T_C \approx 6\,\text{K}$ in amorphous Bi, $T_C \approx 4\,\text{K}$ induced under pressures of a few GPa, a T_C range of between 2-5.5 K on the surface of grain boundaries and T_C of 1.3 K in nanowires [18, 57, 79, 97, 106]. None of these can, however, explain the superconductivity in Bi/Ni bilayers.

Bi/Ni bilayer superconductivity was initially discovered in Bi layers grown on a dusting of Ni in tunneling measurements, which showed that the superconductivity extends across the entire thickness of the Bi [63]. Later, similar measurements showed that in such bilayers, superconductivity and ferromagnetism coexist [55]. Recently, there is a renewed interest in Bi/Ni bilayers as the combination of superconductivity, ferromagnetism, and strong spin-orbit coupling may lead to exotic new physics. In

particular, epitaxial bilayers of Bi/Ni grown by molecular beam epitaxy have been heavily studied [22, 38, 39, 98, 103, 118, 119]. There is speculation that results on these epitaxial bilayers show p-wave superconductivity [38], time-reversal symmetry breaking [39], and chiral superconductivity [103]. All of this is said to originate from the interface of the Bi and Ni (Fig. 4.1.a)

Interfacial Superconductivity (a)   Superconducting Alloy (b)
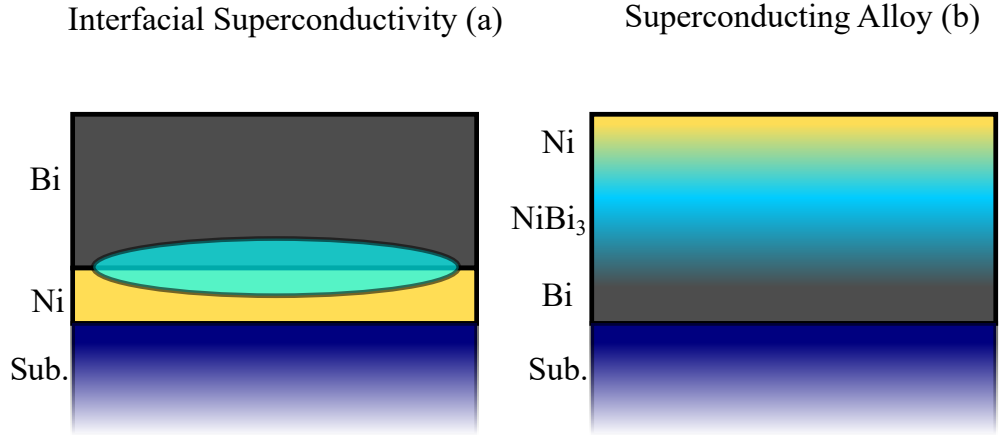
Figure 4.1: Two different models for the origin of superconductivity within Ni/Bi bilayers. (a) Thin film of Bi grow on Ni with interfacial superconductivity highlighted. (b) Our thin films with the NiBi$_3$ superconducting alloy forming at the interface.

An alternative explanation for the origin of the superconductivity in the Bi/Ni bilayer is by the presence of the alloy NiBi$_3$ (Fig. 4.1.b), which is established to superconduct with a similar T_C of 4 K [3, 95]. Measurements on bulk crystals of NiBi$_3$ suggest that it shows coexistence of superconductivity and ferromagnetism [94], however, it is expected to be a singlet, s-wave, superconductor [117]. Silva et al observed this alloy in thin-film Bi-Ni interfaces, which they attribute to spontaneous formation during sample growth at a temperature of 60° C [94]. Liuet al also observe interdiffusion during sample growth at 300 K but no interdiffusion when samples are grown colder than 110 K [59]. Whilst formation during growth will be dominated by comparatively rapid surface diffusion, it is also important to establish whether, and under what conditions, the formation of NiBi$_3$ can occur post-growth when the as-grown samples show initially clean and distinct interfaces of Bi/Ni.

In this chapter, we set out to determine at what timescales and temperatures intermixing from an initially distinct Bi/Ni interface becomes significant. Annealing at low

temperatures, we use SQUID magnetometry, x-ray diffraction (XRD), and polarized neutron reflectometry (PNR) to measure changes in Bi/Ni samples. X-ray reflectometry is not used as the x-ray scattering density for bulk Bi and Ni are too similar for effective contrast at the interface. In successive chapters we have used cross-sectional TEM to look at the crystal structure of the film, a similar technique could be applied here but the local heating effects when using ion milling to cut out the thin cross-section would interfere with the annealing process we are trying to study. We observed the onset of a superconducting T_C, the evolution of the magnetic moment, and the changing structure of the interface. Our results suggest that special handling of the Bi/Ni samples and refrigerated storage is necessary to prevent the formation of $NiBi_3$, which otherwise occurs after a few days at room temperature or a few minutes at temperatures typical of many cleanroom processing steps.

4.1 Experimental Details

Samples were grown by DC sputtering from pure metal targets of bismuth (99.99%) and nickel (99.95%) at $4.3\,\text{Ås}^{-1}$ and $3\,\text{Ås}^{-1}$ respectively. The substrate is thermally oxidized Si with $100\,\text{nm}$ of SiO_2 cleaned using $5\,\text{mins}$ of acetone and then isopropyl ultrasonic cleaning. Using a pure argon (6 nines) atmosphere the growth pressure was $0.43\,\text{Pa}$ for Bi and $0.61\,\text{Pa}$ for Ni, the pressure distance product was $4.4\,\text{Pa cm}$ and $3.8\,\text{Pa cm}$ respectively. Each target was pre-sputtered for $5\,\text{mins}$ as well as a Nb target to act as a getter, a liquid N_2 Meissner trap also reduced the partial pressure of water. The typical base pressure was $1.2 \times 10^{-5}\,\text{Pa}$ and temperature was $21°\,\text{C}$. Growth rates are calibrated by fitting to Keissig fringes obtained by low-angle x-ray reflectometry on single layer reference samples. To prevent oxidation, the samples were capped with $5\,\text{nm}$ thick Ta layers.

The sputtering system was not the same as described in detail in the Methods chapter. This sputtering system is used for depositing multilayers from individual sputter sources that are not confocal. The system has space for 24 samples and 12 sputter sources. The Meissner trap takes 2 hours to reach room temperature before the chamber can be vented, the samples then had to spend that time at room temperature. After the growth was complete, the samples were kept on the Meissner side of the vacuum chamber to partially limit annealing.

Figure 4.2 are the thickness optimizations to achieve the highest T_C and it is found

that optimal layers are above 50 nm of Bi and at 6 nm of Ni, consistent with previous work [38]. The presence of a superconducting transition was not dependent on the order of the layers and we took advantage of this to grow Ni on Bi [38]. Attempting to grow Bi on Ni as was done in the earliest work was unsuccessful, the Bi grew very loosely adhered islands on the surface and not a smooth layer. The islands were poorly attracted and susceptible to oxidation.
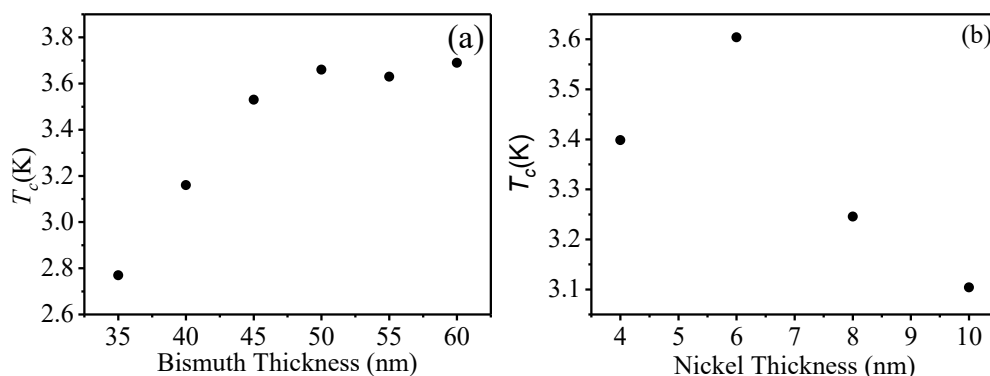
Figure 4.2: Optimization of superconducting T_C as measured by the meissner in a VSM. (a) Nickel layer fixed at 6 nm with bismuth layer varied, after 2 weeks at room temperature.(b) Bismuth layer fixed at 50 nm and nickel layer varied, annealed at $100°$ C. Maximize above 50 nm of bismuth and 6 nm of nickel. Typical T_C uncertainty of ± 0.002 K

To prevent unintentional annealing, directly after removing from the deposition system, the samples were stored in a freezer at $\approx -20°$ C (Beko fridge/freezer model CDA543FW) and transported in a portable refrigerator (Halfords 24L 12V Electric Coolbox) at $\approx 4°$ C. Samples were vacuum packed in airtight plastic to minimize condensation. 31 days elapsed between sample growth and the PNR measurements. We either anneal our samples at room temperature ($21°$ C), or perform controlled annealing of our samples between $50°$ C and $150°$ C on a preheated hotplate under a cover to maintain a uniform temperature. Samples were placed and removed directly from preheated hotplates face down to thermal cycle the thin films as fast as possible to minimize time error, < 10 s.

PNR was performed on the PolRef beamline at the ISIS neutron and muon source. PNR data was analyzed using the GenX software [16]. XRD was performed on a Rigaku SmartLab diffractometer using Cu K$_\alpha$ $\lambda = 1.54$Å radiation and magnetization loops were measured using a Quantum Design MPMS 3 SQUID magnetometer both courtesy

of the ISIS R53 characterization lab. We also employ an Oxford Instruments MagLab 8T VSM for additional magnetization measurements for the temperature dependent annealing. Electrical transport measurements were performed using a standard 4-point probe AC method utilizing a lock-in amplifier and a $77\,\text{Hz}, 100\,\mu\text{A}$ current inside a 4He variable temperature cryostat with a $3\,\text{T}$ superconducting magnet in a horizontal Helmholtz Coil configuration.

4.2 Polarized Neutron Reflectometry Measurements

By measuring the neutron reflectivity as a function of the wavevector transfer and neutron spin eigenstate, PNR allows the scattering length density (SLD) to be obtained. Careful fitting to the two obtained reflectivity curves in PNR allows the extraction of depth dependent magnetization and structure. PNR is widely employed in the successful characterization of spintronic materials [115] and is particularly useful in this study due to the large SLD contrast between the Ni and Bi layers. The samples were annealed repeatedly at $70°\,\text{C}$. Films were loaded at room temperature and cooled in an $0.2\,\text{T}$ field to $10\,\text{K}$ where we performed PNR measurements.

Figure 4.3 (a,c) shows the obtained PNR curves for the sample with the corresponding fit to each spin state. (a) shows the as-grown state, while (c) was after $3600\,\text{s}$ annealing at $70°\,\text{C}$. The higher frequency oscillations arise from the thick SiO_2 layer on the substrate. The thinner, rougher layers of the film modulate these oscillations. The spin asymmetry as calculated by $\frac{u-d}{u+d}$ is shown in figure 4.3 (b,d). The spin asymmetry directly scales with the sample's magnetization. The spin asymmetry shows a significant reduction between the as-grown and annealed states indicates a reduction of magnetization.

We employed a box model to fit the PNR data with the layers Ta_2O_5/Ta/Ni/NiBi$_3$ /Bi/SiO_2/Si. Ta_2O_5 is the most common oxide of Ta and the SiO_2 density is taken as amorphous. Each layer is assigned a thickness, roughness, magnetization, scattering length, and density. The scattering lengths were fixed from the known bulk values. Magnetism in the structure is limited to the Ni and NiBi$_3$ layers, NiBi$_3$ is not ferromagnetic and we do not find a significant moment inside this layer. All other parameters except the substrate density and thickness (the substrate was infinitely thick) were free fitting parameters with physically realistic bounds defined from either the known bulk or as-grown values. The results of fitting are shown in figure 4.3 (e), table (Tab. 4.1)
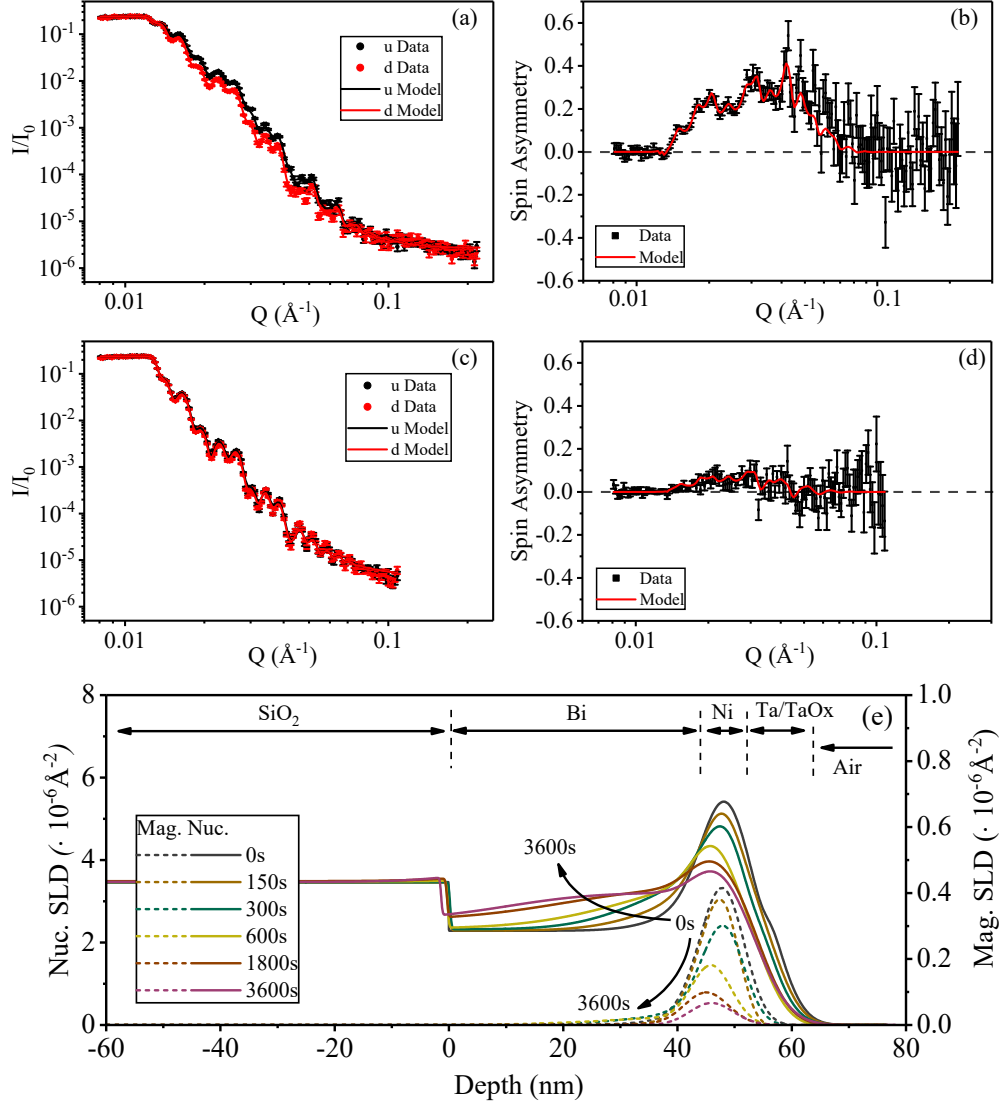
Figure 4.3: Polarized neutron reflectometry (PNR) measurements at 10 K and 0.2 T of Si/SiO (100 nm)/Bi (50 nm)/Ni (6 nm)/Ta (5 nm) sample. (a),(b) PNR and spin asymmetry in the as-grown state. (c),(d) PNR and spin asymmetry after 3600 s annealing at 70° C. The solid lines are fits to the data and the returned fit parameters are given in table 4.1. (e) The nuclear and magnetic scattering length density (SLD) with depth returned from fitting showing the evolution of SLD with successive annealing.

and the full fitted parameters are listed in the appendix A.

The results of fitting are shown in figure 4.3.(e). As grown the samples do show a thin (2 nm) NiBi$_3$ layer that has either formed during growth or in the time taken to remove them from the deposition system. Consequently, the Ni and Bi layers were slightly thinner than expected (4.4 nm and 44 nm versus the nominal 6 nm and 50 nm). The thickness of the NiBi$_3$ layer in the model was less than the roughness of either the Bi or Ni interfaces and suggested that it was an intermixed region rather than a distinct ordered layer of NiBi$_3$. The magnetic SLD of bulk Ni is $\approx 1 \times 10^{-6}\,\text{Å}^{-2}$ where our magnetic SLD for the Ni in the as-grown state was $\approx 0.4 \times 10^{-6}\,\text{Å}^{-2}$ as the roughness distributes the Ni over a wider range. The area under the magnetic SLD and the area derived from the box model with no roughness was $3.98 \times 10^{-6}\,\text{Å}^{-1}$ and $3.97 \times 10^{-6}\,\text{Å}^{-1}$ respectively.

The main changes to the structure with annealing the sample were the diffusion of Ni atoms into the Bi layer. The stronger nuclear scattering of the Ni increased the SLD of the Bi layer where atoms have diffused (Fig. 4.3.(e)). The structural profile of the final annealed state suggests that the Ni can diffuse across the entire thickness of the Bi as the SLD of the entire layer was raised. At the Bi/Ni interface, we report that a layer with the correct SLD for ordered NiBi$_3$ intermetallic layer was found. The thickness of this layer increases with annealing from (2 nm) in the unannealed state, to (38.8 nm) in the final annealed state.

As the Ni diffused; less ferromagnetically ordered Ni is left, in turn decreasing the magnetic SLD profile and moment measured independently from SQUID. For the final two annealing steps, the fitting returns a very thin layer of Ni (0.7 nm). The large roughness (4 nm) of this layer suggests it is no longer continuous and has been replaced by an intermixing layer. In an attempt to improve the modeling, we tried replacing this Ni layer with a layer approximating a NiBi intermixing layer. Doing so, we find the fitting returns a lower figure of merit, indicating that the model has a closer resemblance to the physical sample. This suggests that in the final annealed state, Bi contaminates the Ni layer in addition to the Ni diffusion into the Bi layer. There is very little change to the scattering length density shown in figure 4.3.e between the two models as the roughness tends to smear such fine details. The full fitting parameters from each model are provided in the appendix A.

Layer (nm)	Initial	Final
Ta_2O_5	1.6 ± 0.3	4 ± 0.5
Ta	4.9 ± 0.4	0.5 ± 0.5
Ni	4.5 ± 0.7	0.7 ± 0.1
$NiBi_3$	2.3 ± 0.4	38.8 ± 0.7
Bi	44.1 ± 0.4	9.3 ± 0.7
SiO_2	95.0 ± 0.3	93.9 ± 0.5

Table 4.1: The initial ($0\,s$) and final ($3600\,s$) annealed fitted thicknesses at $70°\,C$. The full fitting parameters are given in the appendix A.

4.3   Magnetometry

To study the magnetic and structural properties of our Bi/Ni bilayer samples we employed SQUID magnetometry and Cu K_α $\lambda = 1.54$Å x-ray diffraction (XRD). We used a sample grown in the same vacuum cycle as the sample we study by PNR, which we diced into smaller ($4x4\,mm$) cuttings. The individual cuttings were treated with the same annealing process at $70°\,C$ as the PNR sample. After annealing, we first measured the magnetic hysteresis (moment vs field) of the cuttings at 10 K (the same temperature as the PNR), then checked for a superconducting transition by measuring moment vs temperature from the base temperature of the magnetometer at small applied field (2-10 K sweep at 5 mT), finally we transferred the cuttings to the x-ray diffractometer where XRD was measured at room temperature. To minimize annealing during the x-ray measurements, the total time to align and record an XRD scan was optimized to take about 30 minutes. Nevertheless, we find by re-measuring a cutting's magnetic response after the room temperature XRD scan has finished, that some annealing occurs during the x-ray measurement. We do not believe this to have been an influence on the results presented in this section, however, as a precaution we do not measure the same cutting more than once and each annealing time for SQUID and XRD measurements were from a different cutting of the pristine sample.

The magnetic characterization of our Bi/Ni bilayer samples are shown in figure 4.4. We extracted the saturation (applied field of 1 T) moment/area by measuring hysteresis loops from cuttings with different annealing times. Exemplar hysteresis loops are shown in the inset of figure 4.4. For the as-grown sample cutting, the saturation
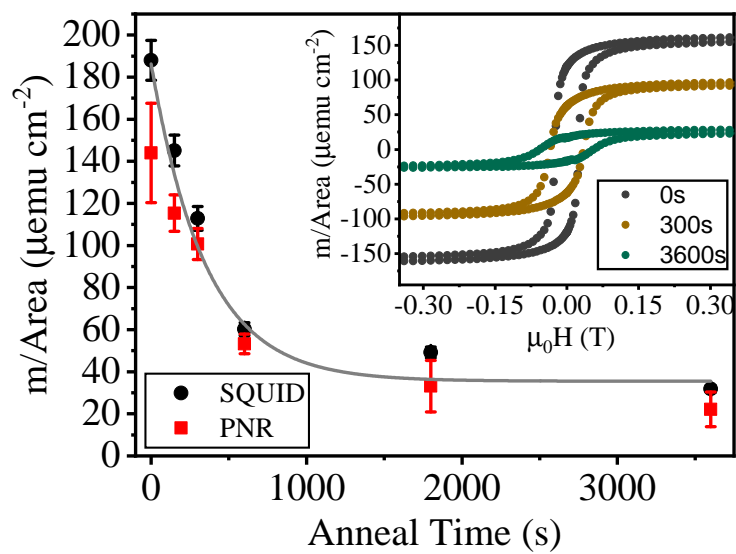
Figure 4.4: Magnetic characterization at 10 K of Si/SiO (100 nm)/Bi (50 nm)/Ni (6 nm)/Ta (5 nm) samples. The moment per area calculated from the hysteresis loops, inset, are shown with annealing time at 70° C. The diamagnetic contribution due to the substrate has been subtracted. The uncertainty in the SQUID moment/area is dominated by the area measurements (different cuttings of the sample are used for each annealing step), and is less than 5% . Also shown is the moment/area extracted by fitting the PNR measurements. The line on the main figure is a guide for the eye.

magnetization of the 4.4 nm Ni layer was $318\,\mathrm{emu/cm^3}$, reduced from the bulk value of $600\,\mathrm{emu/cm^3}$. The reduced magnetization is consistent with the formation of magnetic dead layers, which are often observed in thin film Ni [82]. For all sample cuttings, we find that a large magnetic field (nearly 1 T) was required to achieve full saturation, hence the hysteresis loops shown in figure 4.4 inset do not fully close within the field range shown. As the film was annealed, two changes to the hysteresis loops were observed; firstly, the saturation moment/area of the sample reduces and secondly, the coercive field increases. Both observations are consistent with the PNR modeling which shows that as the sample is annealed, non-magnetic $NiBi_3$ intermetallic forms reducing the ferromagnetic Ni thickness.

It is possible to compare the measured magnetic moment returned from the SQUID measurements and PNR fitting (Figure 4.3) by normalizing datasets to the areas of the samples. Collated moment/area with annealing time at $70^\circ\,\mathrm{C}$ for the samples are shown in figure 4.4. As the sample was annealed we observed an exponential type decay of the sample moment/area from about $188\,\mathrm{emu/cm^2}$ in the as-grown state to $32\,\mathrm{emu/cm^2}$ after 3600 s annealing at $70^\circ\,\mathrm{C}$. The time constant of the decay was $430\,\mathrm{s}$. The extracted moment/area by the two techniques show close agreement in both trend and absolute value for annealed samples, we note that there was some disagreement in the magnetic moment of the as-grown state.

4.4   X-Ray Diffraction

Figure 4.5.a shows the results of XRD characterization. In the as-grown state, structural peaks due to the Bi layer and Si substrate were present in the sample. We do not expect Ni or Ta peaks to appear as these layers were too thin. After annealing, peaks appear in the XRD scan which correspond to the $NiBi_3$ intermetallic and equally the Bi peak intensity drops, suggesting that the textured Bi layer was being replaced by a textured $NiBi_3$ intermetallic. The timescale for these structural changes to occur to the sample was similar to the timescale where changes are observed in PNR and SQUID measurements annealed at the same temperature.

To get a better idea about the orientation of these $NiBi_3$ crystallites the individual Bragg peaks can be projected on a pole plot to map out the relative orientation preference (Fig. 4.6). The $NiBi_3$ has a weakly preferred orientation toward to [203] direction as well as [001]. Because the $NiBi_3$ was created by annealing of an interface Bi and
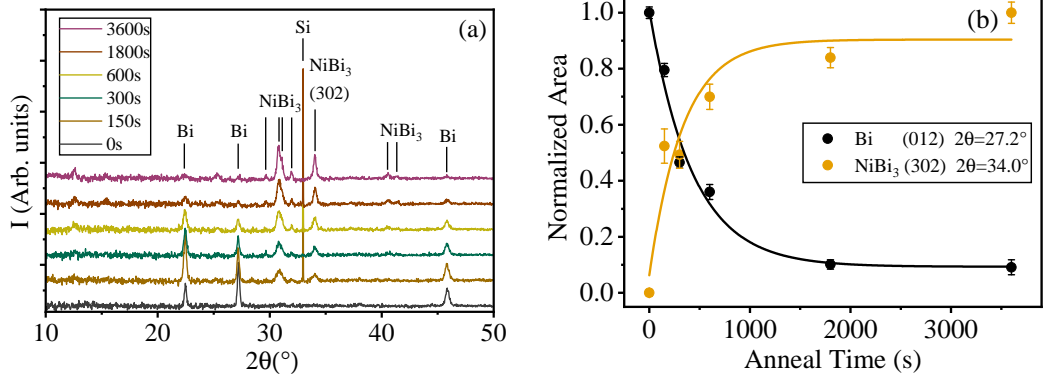
Figure 4.5: X-ray diffraction characterization of 70° C annealed Si/SiO (100 nm)/Bi (50 nm)/Ni (6 nm)/Ta (5 nm) samples. (a) Surfaced aligned XRD scans with annealing time. Peaks due to the Si substrate, Bi layer and NiBi$_3$ intermetallic are indexed. (b) The normalized area under the Bi (012) and NiBi$_3$ (302) peaks to show evolution of the sample with annealing step. Lines are a guide to the eye.

Ni, and neither layer had any significant orientation preference it is surprising that the NiBi$_3$ layer does. This could be because the diffusion rate of atoms may be anisotropic through NiBi$_3$, thus any grains that initially forms along one of these higher diffusion directions will grow faster. At the end of the annealing the grains that started in the high diffusion orientations grew larger, giving a larger XRD response.

4.5 Superconducting Transport Properties

Low temperature 4-point probe transport measurements of a 70° C fully annealed sample (3600 s) showed a clear zero resistance superconducting transition at 3.8 k (Fig. 4.7), the critical magnetic field in-plane and out-of-plane were also measured (Fig. 4.8). The critical field is measured by fixing the temperature and sweeping the field through H_{c2}. The normal state resistance also had a positive MR as would be expected for a normal metal.

H_{c2} was calculated by fitting a logistic function to the MR sweep and taking 50% of normal state resistance as the critical point (Fig. 4.8). The out-of-plane and in-plane H_{c2} temperature dependence can be fitted effectively by the following Ginzburg-Landau (GL) model for a thin superconductor;
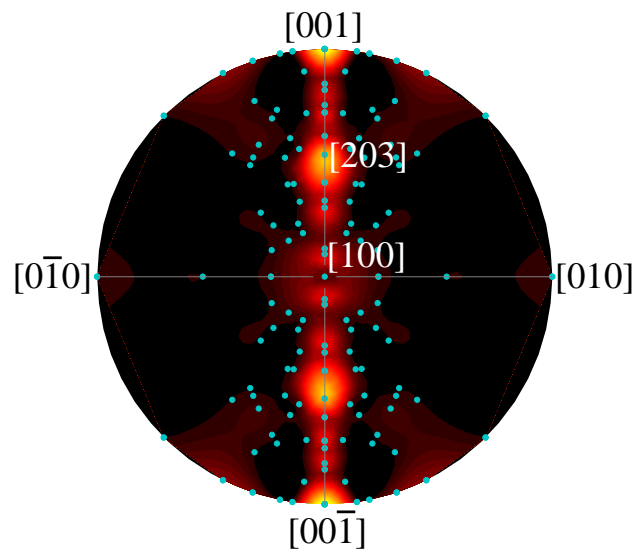
Figure 4.6: Pole plot of the NiBi₃ peaks projected along the [100] direction. The most prominent peak is the [203] peak. Blue points are the individual peaks expected for NiBi₃, the measured peak intensity is normalized against the powder diffraction peak intensities. The heat map uses a smoothed contour for easy of viewing. The points are relative to the powder diffraction intensities.
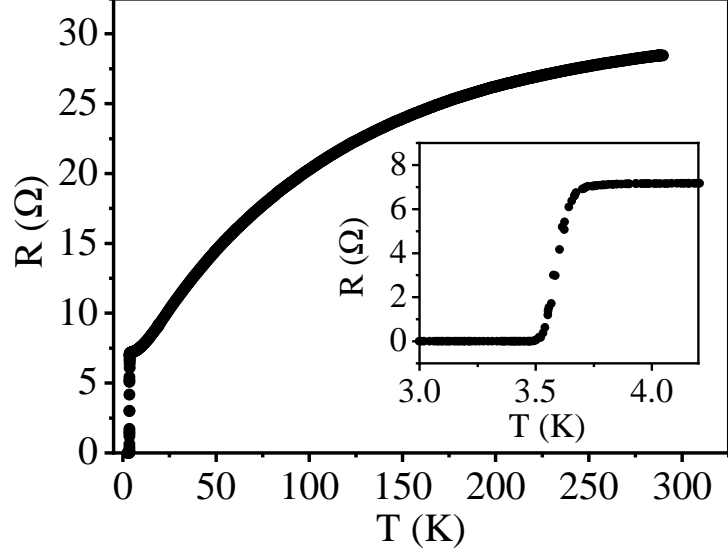
Figure 4.7: Electrical transport characteristic of Si/SiO (100 nm)/Bi (50 nm)/Ni (6 nm)/Ta (5 nm) sample after 70° C annealing for 3600 s. Resistance verses temperature with the superconducting transition at 3.8 K shown in the inset.

$$\mu_0 H_{c2}^{\perp} = \frac{\Phi_0}{2\pi\xi_{\mathrm{GL}}(0)^2}(1 - \frac{T}{T_c}) \tag{4.1}$$

$$\mu_0 H_{c2}^{\parallel} = \frac{\Phi_0\sqrt{12}}{2\pi\xi_{\mathrm{GL}}(0)d_{\mathrm{SC}}}(1 - \frac{T}{T_c})^{\frac{1}{2}} \tag{4.2}$$

where Φ_0, $\xi_{\mathrm{GL}}(0)$ and d_{SC} stands for flux quantum, in-plane coherence length and effective thickness of the superconductivity respectively. Taking the values from both in-plane and out-of-plane H$_{c2}$(0) fits the coherence length ξ_{GL} as 13.8 nm and the effective superconducting thickness d_{SC} as 36.2 nm, similar to the thickness of the NiBi$_3$ layer as obtained from the PNR data. The GL-theory for thin superconductors assumes that the $d_{\mathrm{SC}} < \xi_{\mathrm{GL}}$ which is not the case here and is visible in figure 4.9.b from the inadequate fitting for the in-plane H_{c2} data. The T_C during fitting is fixed to the T_C measured by the resistivity verses temperature data.

Alternatively, making the power of the in-plane equation a free parameter (instead of a fixed $\frac{1}{2}$), returns a value of 0.659 for the power and a more satisfactory fit to the experimental data. A returned power of 1 is expected for bulk behaviour, suggesting this sample is in some intermediate state between bulk and thin superconductivity.
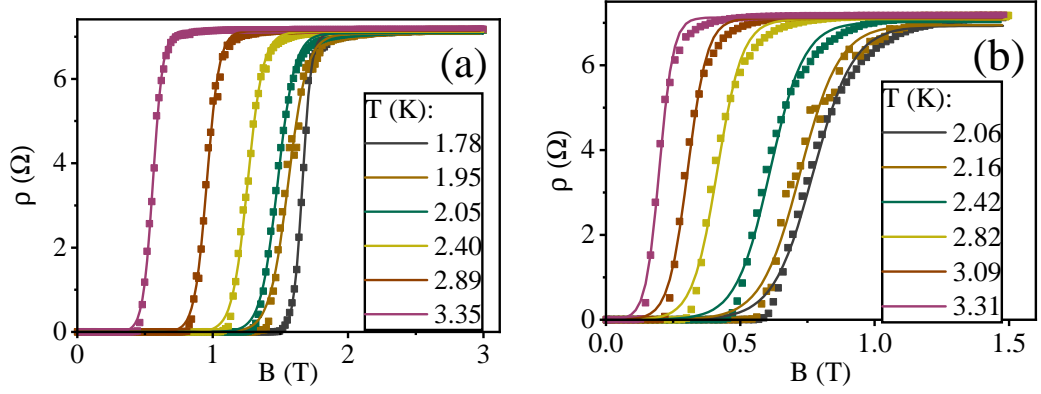
Figure 4.8: (a) The in-plane critical field measured by field sweeping at a fixed temperature. Solid lines are logistic function fits and the critical point is taken at the 50% threshold. There is a small positive MR in the normal state. (b) The critical field for the out-of-plane is the same just with smaller fields.
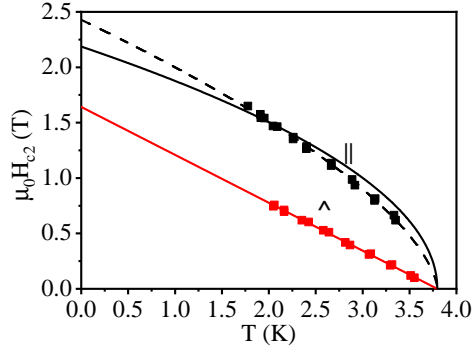
Figure 4.9: Magnetoresistance characteristic of Si/SiO (100 nm)/Bi (50 nm)/Ni (6 nm)/Ta (5 nm) sample after 70° C annealing for 3600 s. The out-of-plane (red) and in-plane (black) H_{c2} data, solid lines a model fit for a thin superconductor (Equ. 4.1,4.2). The dashed line has the power of $\frac{1}{2}$ in equation 4.2 as a free fitting parameter. $\mu_0 H_{c2}^{\parallel} = 2.28$ T and $\mu_0 H_{c2}^{\perp} = 1.72$ T, the power of the dash line is 0.659.

4.6   Influence of Annealing Temperature

Samples as-grown were not immediately observed to be superconducting, but after annealing or leaving at room temperature for several days the magnetization of the Ni layer was reduced although it is nonvanishing and an increased coercivity (Fig. 4.10.a), after that a superconducting transition appeared and increased until stabilizing at 3.8 k (Fig. 4.10.b). The thickness of the NiBi$_3$ layer grows quickly as the sample was annealed and once the layer was thick enough to support a superconducting transition there was a Meissner response that was measured to deduce the T_C. By measuring the T_C at several points along the annealing process a time constant for the onset was fitted from a decaying exponential. As long as the sample was far from saturating T_C the time constant would not be affected by small amounts of annealing that may have already taken place. The time constant against annealing temperature can be described well by the Arrhenius equation for a thermally activated reaction with an association activation energy of (0.86 ± 0.06) eV (Fig. 4.11.b). The activation energy was lower than for similar systems of interface mixing and diffusion with typical activation energies of ≈ 1 eV [45, 72].
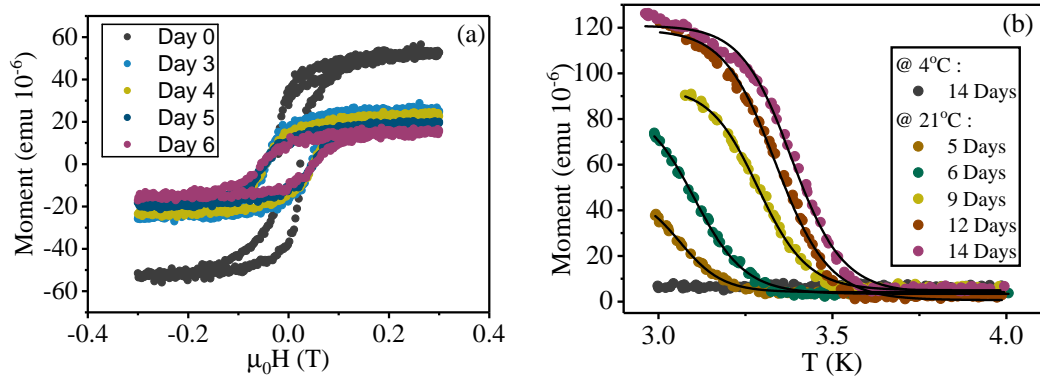
Figure 4.10: (a) Sample of Ta(5)/Ni(6)/Bi(50) nm stored at room temperature and hysteresis measured at 3 K. (b) MvT of two Ta(5)/Ni(4)/Bi(50) nm samples stored at room temperature (21 °C) and within a fridge (4 °C), black lines are logistic function fitting for which the T_C is taken at 20% height.
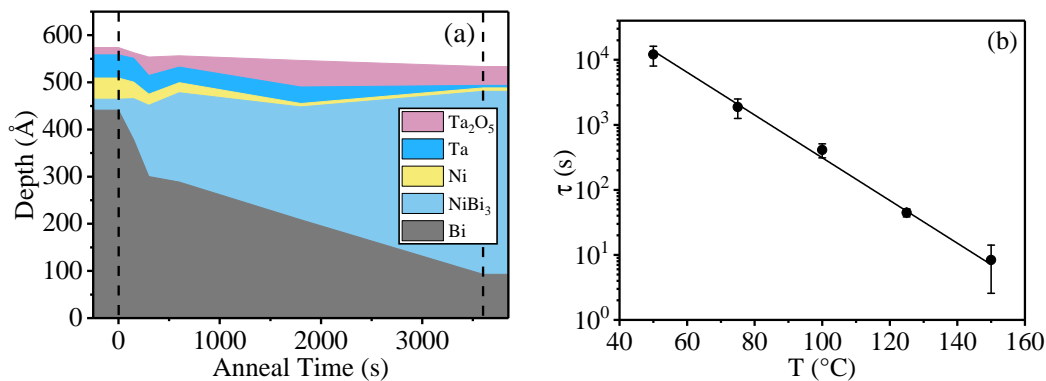
Figure 4.11: (a) Fitted thickness extracted from PNR data for each annealing step, omitting the roughness at the interface for simplicity. The annealing at $70°$ C takes place between the dashed vertical lines. (b) Arrhenius plot of Bi/Ni bilayers annealed in the temperature range of $50°$ C– $150°$ C with an activation energy of (0.86 ± 0.06) eV, time constants taken from the superconducting T_C onset rate measure by VSM (Fig. 4.10).

4.7 Discussion

Figure 4.11.a shows the fitted thickness for each annealing step as extracted from PNR. The Ta_2O_5 increased as expected for heating in air and protected the lower layers from oxidation. The thickness of the Bi and Ni layers reduced as the $NiBi_3$ layer became thicker. We also observed an overall reduction in film thickness as the $NiBi_3$ alloy is denser than the individual Bi or Ni layers. To optimize the T_C at least 50 nm of Bi was needed for 6 nm of Ni (Fig. 4.2.a), the ratio may suggest that to obtain the highest T_C annealed samples one should minimize the remaining Ni and maximize the thickness of the $NiBi_3$.

Extrapolating from the Arrhenius plot toward $21°$ C gave a time constant for the annealing rate as 4 days which is comparable to the timescale measured at room temperature, the exponential has a doubling/half life of every $\approx 6°$ C such that if kept at $3°$ C the timescale extends to 12 days (Fig. 4.11). The low annealing temperatures can be understood from the low melting point of Bi of 544 K being about twice room temperature (≈ 294 K). It is not uncommon to anneal thin films to form alloys at 50% of the constituent layers melting points. The Bi atoms become mobile at higher temperatures diffusing across the interface and the same for Ni as it diffuses into the

Bi layer forming a $NiBi_3$ alloy.

Process	τ (s)
SQUID+PNR Mag.	440 ± 90
XRD Bi peak	430 ± 80
XRD $NiBi_3$ peak	300 ± 100
Ni Thickness	500 ± 100
Bi Thickness	1300 ± 900
$NiBi_3$ Thickness	2000 ± 2000
T_C Onset	1500 ± 700

Table 4.2: The decaying exponential fits for various measurements for different parameters during the $70\,^\circ$C annealing. Thickness from the PNR GenX fits, SQUID+PNR Mag. from figure 4.4, XRD Bi and $NiBi_3$ from figure 4.5, T_C fitted from VSM measurements.

Table 4.2 has the time constants fitted from various measures such as PNR, XRD, and SQUID. Since only 6 points were taken for the PNR study, the errors for these values are large. All of the values are within an order of magnitude of each other follow a reasonable ordering. The fastest process was the reduction of the Ni thickness, loss of magnetism in the SQUID+PNR and the $NiBi_3$ XRD peak. One of the slowest processes was the T_C onset as both the ferromagnetic Ni must be first reduced and then grow a thick enough $NiBi_3$ layer to allow a superconducting transition. The XRD peak data was faster than expected from the PNR thickness time constants, both instruments have different sensitivity but also it was known that during an XRD measurement a sample will anneal as the interior space of the Rigaku was above room temperature.

When first measured in PNR, the as-grown un-annealed sample had a thin layer, $2\,nm$, at the interface with a similar SLD to $NiBi_3$. In comparison the corresponding un-annealed XRD there were no $NiBi_3$ peaks above the background noise and so quantity of any *ordered* $NiBi_3$ should be small. In samples that have been intentionally annealed, the ratio between $NiBi_3$ XRD peak intensities and the fitted layer thickness suggest that if $2\,nm$ of ordered $NiBi_3$ did exist in the un-annealed state as the PNR suggests the there should be $NiBi_3$ peaks above the background noise in the XRD. Thus the $2\,nm$ of $NiBi_3$ is then not as ordered and is closer to that of an amorphous intermixed region. This thin intermixed layer was not unexpected. Because of the roughness of

the Bi layer, implantation of Ni adatoms during growth, and the time taken to get the samples from a room temperature vacuum chamber to the freezer all contributed to some intermixing of the interface but without time to form an ordered alloy of $NiBi_3$.

Liu *et al* performed pulsed laser deposition (PLD) of Bi/Ni bilayers where they report the $NiBi_3$ alloy forms during growth. Their interpretation is that PLD is a nonequilibrium process such that Ni atoms arrive at the Bi layer with enough energy to implant deep into the film. Ni implantation stops at the SiO_2, where it accumulates forming a NiBi alloy and a $NiBi_3$ layer further from the SiO_2. We find that ordered $NiBi_3$ does not exist in our samples as grown, but formed during annealing and was confined to the Bi/Ni interface. We do not find evidence for ordered NiBi alloy in our films, however, in the final annealed state Bi may have contaminated any remaining Ni layer in the structure. We conclude that during growth the Ni implantation depth is confined to near the top surface of the Bi, as fitted by the 2 nm of $NiBi_3$ in the as-grown state.

By measuring PNR below T_C in an applied field, it is possible to observe Meissner screening under the right conditions ,that the film thickness, roughness, and the superconducting penetration depth are balanced to allow for measurable screening to occur [28, 116]. It is also possible that exotic superconducting states can influence the magnetic response of a superconducting sample [32, 33, 60]. Here, we measured both the as-grown and fully annealed states of the sample at 3 K (below the superconducting transition for the annealed sample) to look for changes to the magnetic response from the sample. No such changes were observed below T_C in the PNR, most likely as the $NiBi_3$ superconductor was too thin to observe Meissner screening.

Experimental results by other techniques suggest that superconductivity in bilayers of Bi/Ni may be spin-triplet (*p*-wave) in nature [22, 38, 39, 98, 103, 118, 119]. The symmetric spin-triplet states are found in only a handful of superconductors, where Sr_2RuO_4 is currently the best candidate [60]. In these materials, the antisymmetry requirements are satisfied by the condensates of these superconducting materials being spatially antisymmetric, that is, odd in angular momentum. It is also possible to generate spin-triplet states in proximity coupled thin films where *s*-wave pairing is retained by introducing a Berizinskii state with spontaneous breaking of time-reversal symmetry [13]. Our Bi/Ni samples contain all the necessary ingredients for such a state to occur; a source of *s*-wave superconductivity ($NiBi_3$), ferromagnetism (Ni), and

strong spin-orbit coupling (Bi) [12, 49, 87, 88].

4.8   Conclusions

In this work samples of Bi/Ni bilayers were observed initially to be non-superconducting until either left at room temperature for several days or a short period of heating as low as $+50°$ C. The superconductivity was attributed to the intermixing of the Bi/Ni interface forming an alloy of NiBi$_3$ identified by XRD Bragg peaks. PNR data is consistent with initially distinct Bi/Ni layers with minimal NiBi$_3$ in the as-grown states, when annealed at $70°$ C for 1 hour the diffusion across the interface increased the NiBi$_3$ thickness and reduced the thickness of the pure Bi/Ni layers.

From this, it seems that to properly study clean and distinct interfaces that maintaining a low temperature for preparation and storage is important. Normal device fabrication recipes which use heating to bake resist or growth methods that allow the sample to heat up will fully anneal Bi/Ni bilayers. Although the superconductivity originates from a known bulk superconductor, the existence is still interesting as it is in close proximity to a ferromagnetic layer, a strong spin-orbit coupling Bi layer and also the likely proximity effect in the Bi layer.

CHAPTER 5

High-Quality Single Crystals of Epitaxial YPtSb (111) Grown On C-plane Sapphire By Co-Sputtering

In this chapter we will look at the HHA YPtSb. Y and Sb are lighter elements with weaker SOC than many other HHA considered as candidates for TI states. As a result band structure calculations have predicted that it sits at the boundary for a TI state [2]. As it is so close to a TI state, tuning and external triggers might switch it from a normal state to a TI state, making it a potential exciting system to work in. As the band inversion strength is close to zero (Fig. 5.1), the bandgap is also predicted to be very small or zero. To open a gap in both the normal and TI states, strain would be needed [21], such as growth on c-plane Al_2O_3 where the lattice mismatch is $\approx 5\%$.
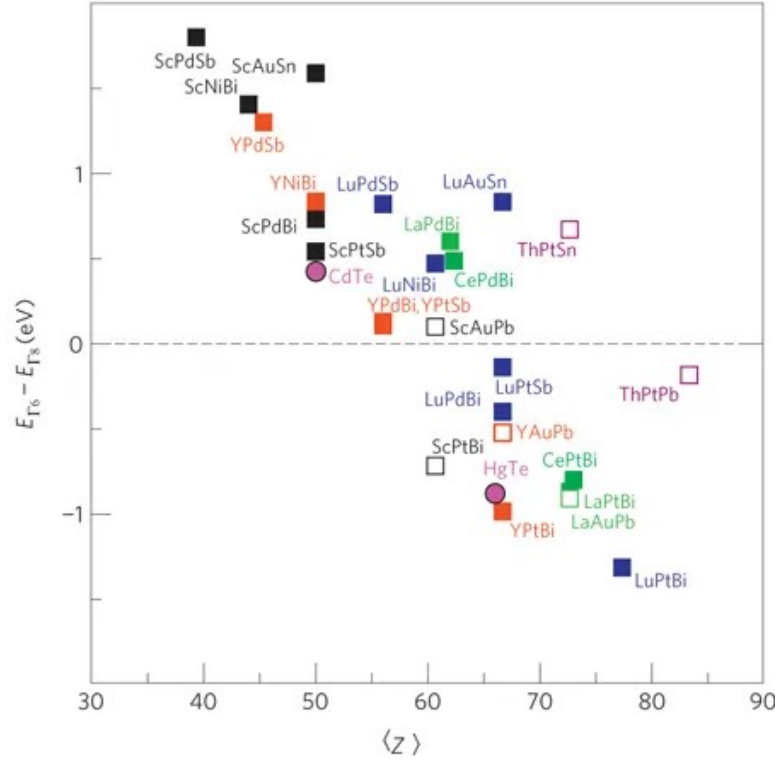
Figure 5.1: Graph of the predicted band inversion strength as measured by energy difference between the top of the Γ_6 band and the bottom of the Γ_8 band ($E_{\Gamma_6} - E_{\Gamma_8}$) for several HHA. The $<Z>$ axis is the strength of the SOC. Points below the dashed line are predicted to be topological non-trivial. Graph from [21].

Bulk single crystal samples of YPtSb have been made by arc melting and used in optical measurements, where the band gap is at most $60\,mV$ and thus assumed to be gapless [76, 77]. Ouardi *et al.* observed the real and imaginary permittivity and

reflectivity in the photon energy range of 1-5 eV and 6-1000 eV. They successfully fitted an analytical model with a linear dispersion band to the optical measurements and concluded this as evidence for a conic like dispersion relation. Figure 5.2 has their measured carrier densities, with values of the order of $7 \times 10^{18}\,\mathrm{cm}^{-3}$ and mobilities as high as $400\,\mathrm{cm^2V^{-1}s^{-1}}$. They also measured the thermoelectric properties and found a high figure of merit, ZT= 0.2. High figure of merits are common for many TI materials since both have small band gaps are made of heavy elements [111].
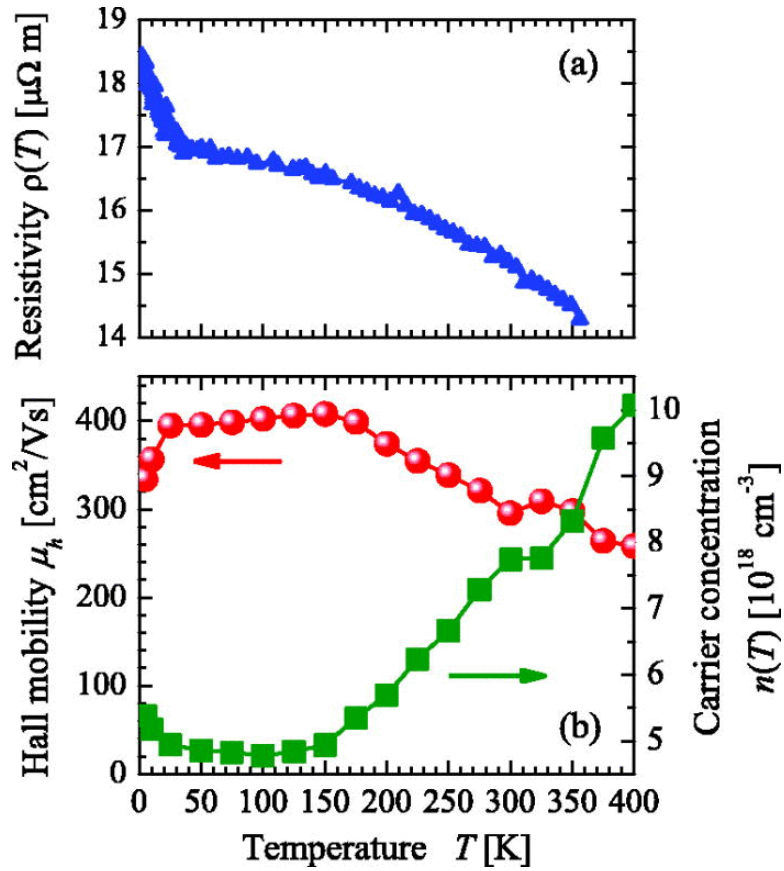
Figure 5.2: (a) Resistivity as a function of temperature showing non metallic behaviour. (b) The carrier density and mobility also as a function of temperature. Graphs from [76].

Another group have also observed high mobilities in polycrystal samples of YPtSb that are as large as $4124\,\mathrm{cm^2V^{-1}s^{-1}}$, as well as LaPtBi and LuPdSb with similarly high mobilities [93]. Compared to the single crystals of Ouardi *et al.*, the mobility is

$10\times$ greater and the carrier density $\times 5$ lower. They also observed a non-saturating positive MR and came to the conclusion of a zero-bandgap through electrical transport properties, and even extended it to also suggesting a linear dispersion band. Their justification of a linear dispersion band was the very high mobility leading to a light-effective-mass expected from a linear dispersion band. There is no quoted crystallite size that would indicate if this high mobility is achievable at our film thickness.

Thin film YPtSb has previously been grown on MgO substrates and on MgO buffer layers on Si substrates by the Shan *et al.*group [91]. For the MgO substrate work, only the carrier density is explicitly quoted in the range of 10^{20}-10^{21} cm^3. By taking the stated resistivity we can calculate a mobility of $\approx 250 \, \text{cm}^2\text{V}^{-1}\text{s}^{-1}$. Their thin films have a strong preference to growth on the along the (111) YPtSb plane and also in-plane XRD shows the four lattice matching orientations repetitions (Fig. 5.3). The preference for the (111) was explained as the densest plane growth which can be expected to occur. The in-plane texture is unexpected as the mismatch quoted in the work is 10% and that the MgO has square symmetry while the (111) YPtSb plane has hexagonal symmetry. Ultimately the strength for any in-plane texturing is no greater than a factor 5 as the in-plane XRD peaks are broad and overlapping. We expect that for c-plane Al$_2$O$_3$, the orientation preference will be unique. We also attempted to grow on MgO to replicate work done by the group Shan *et al.*.

The Wang *et al.* group grew YPtSb on a MgO buffer layer where no lattice matching is expected or in-plane texture [104]. Their thin films are in the μm thickness range and had only a slight preference for the (111) orientation with many of the diffraction peaks still appearing in the XRD. Their grain size was $25 \, \text{nm}$ similar to the thickness of our thin films. They also achieved a carrier density as low as 5×10^{18} cm^3 and mobility as high as $450 \, \text{cm}^2\text{V}^{-1}\text{s}^{-1}$. The group observed negative longitudinal MR that transitions to a positive MR when the field is applied perpendicular to the current. They offered a possible explanation of polarized spins locked perpendicular to the current direction, when the field is applied parallel to the current path it is perpendicular to the spin polarized and leads to a negative MR.

There is some potential for a non-trivial state in YPtSb as these previous works have shown narrow band gaps and potentially linear dispersion bands [76, 77, 93]. While we could replace Sb for Bi to increase the SOC and create YPtBi which is predicted to be a TI[2], we used Sb instead as it has the advantage of a higher melting point and is easier
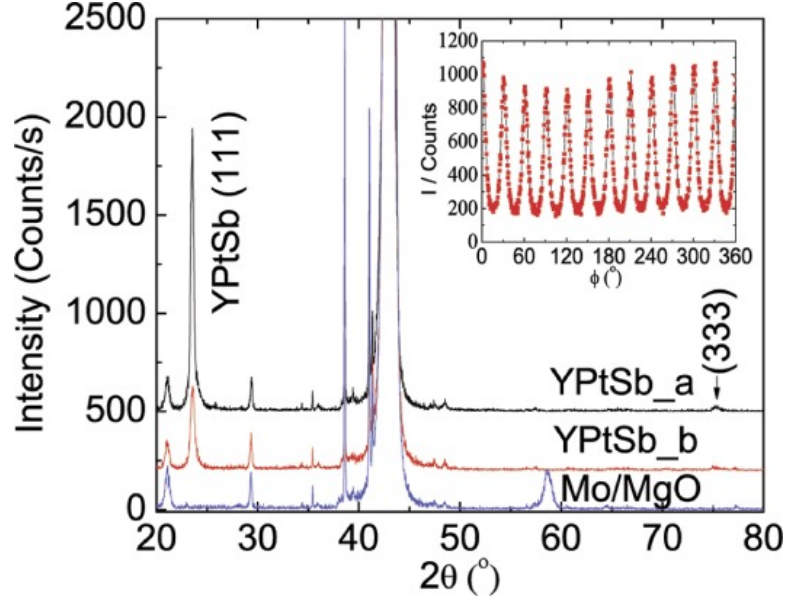
Figure 5.3: XRD of thin films of YPtSb grown on (100) MgO substrate, with both a strong (111) YPtSb texture and (220) in-plane repetition. The in-plane peaks are partly overlapped with the intensity never reaching zero. Graphs from [91].

to sputter with as the Sb target is unlikely to be damaged by the plasma heating. We also have other groups successfully growing YPtSb as thin films proving its viability. In our films we will introduce strain by epitaxially matching. Additionally, Y is an excellent getter, useful for reducing the base pressure inside the growth chamber. This made YPtSb a good first material to study and confirm the ability to grow HHA.

This work presents the growth of YPtSb thin films. The films were optimized for higher temperatures and better grain sizes. The (111) plane lattice matches to the (0001) c-plane Al_2O_3 as confirmed by XRD and TEM. Electrical transport measurements were made that give a higher carrier density and low mobility compared to bulk.

5.1 Experimental Details

Samples are grown by DC magnetron co-sputtering from 3 sputter sources as discussed in chapter 3.1.3. By varying the powers of each of the sputter sources the stoichiometry can be tuned to optimize crystal formation and electrical transport. The substrate was c-plane Al_2O_3 cleaned with 5 mins in an ultrasonic bath of isopropanol and acetone.

MgO substrates were also grown on and prepared by the same method of cleaning. MgO substrates were stored inside a desiccator to remove moisture prior to deposition. The typical base pressure was 3×10^{-6} Pa and the growth temperatures were between $450°$ C $- 650°$ C. A tantalum nitride cap was also used on some samples to prevent oxidation and that it would not significantly affect the transport properties (Ch. 3.2).
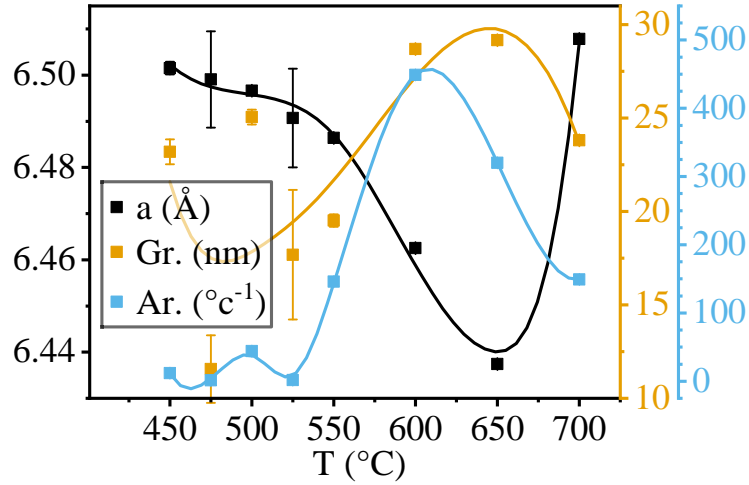
Figure 5.4: The temperature optimization for YPtSb thin films. (a) The lattice constant, (Gr.) estimated grain size and (Ar.) the area under peak are from the (111) XRD peak. Curves are guides for the eye. When the Area (Ar) is small there is a larger uncertainty due a worst signal to noise ratio, additional the grain size and lattice constant are sensitive to the fitting values.

Figure 5.4 contains a selection of samples grown at different temperatures. Each of these samples were not identical in terms of power ratios as the needed ratios for optimal crystallinity change with temperature. As such these samples are not guaranteed to be absolutely optimal for their respective growth temperatures. Even so the area under the (111) peak is more than an order of magnitude greater for the temperature range $600°$ C $- 650°$ C and the grain size is also at maximum. Later samples are grown within this range.

5.2 Results

5.2.1 XRR and XRD

Figure 5.5 shows the XRR of YPtSb thin films without a TaN capping layer. The reflectometry data is fitted by GenX, using a box model of YPtSb on a Al_2O_3 substrate with an oxide layer at the surface (Ch. 3.3.4). Table 5.1 contains the fitted values, the bulk density is calculated by assuming the bulk lattice constant of 6.538 Å and that each unit cell has 12 atoms, 4 of each element, giving a value of $9.675\,g\,cm^{-3}$ [107]. The model fits very well and reproduces all of the features of real data. The large uncertainties in the table are likely a result of the roughness of the film, reflections off a rough surface have less information as a small change in either the thickness or density does not change the scattering significantly. The fitted oxide thickness was much thinner than a reasonable oxide thickness for any metallic material. For an epitaxial film, a density close to 100% would be expected and is with the range of the asymmetric errors. It is likely that the roughness of the surface is hiding an oxide layer and that it isn't visible in the XRR as evidenced by the large uncertainty in the thickness.
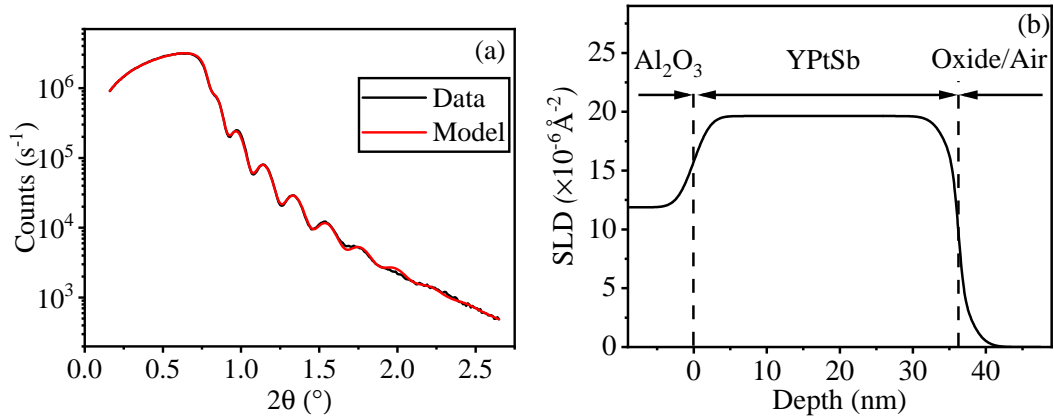
Figure 5.5: (a) XRR of YPtSb thin film grown on c-plane Al_2O_3. (b) SLD as calculated be GenX. Film is 36 ± 7 nm thick.

YPtSb had a strong preference to grow with a (111) plane texture in contrast to the denser (100) and (110) planes which typically form more often as well as having greater scattering intensities (Fig. 5.6.a). The lack of any (200)/(220) peak is a good indication that the (111) axis is strongly preferred over any other. *Pendellösung* fringes

Parameter	Value
Oxide: d (nm)	0^{+2}_{-0}
σ(nm)	2^{-2}_{-1}
YPtSb: d (nm)	36^{+4}_{-11}
ρ (% bulk)	80^{+30}_{-10}
σ(nm)	$1^{+9}_{-0.6}$
Al_2O_3:ρ (% bulk)	100*
σ(nm)	2^{+2}_{-2}

Table 5.1: Fitting parameters after using GenX to fit the XRR data in figure 5.5.(+) and (-) are asymmetric errors ranges.(*) Value fixed to bulk.

on the (111) peak indicated that we have inter-lattice interference, which is the result of smooth thin films and another sign of high-quality crystals. Figure 5.6.b is of a thinner sample where the oscillations were spaced farther apart for easier identification and fitting.
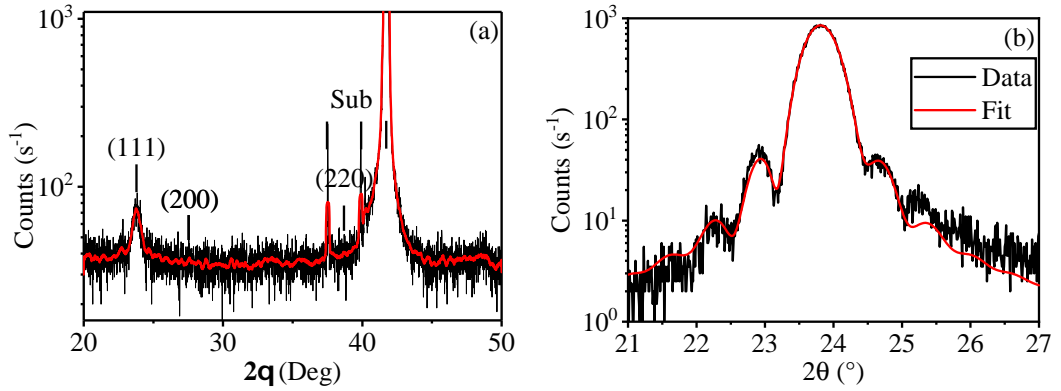
Figure 5.6: (a) HAX for YPtSb film with the (111) peak visible but no (200)/(220) peak can be seen above the noise, the red line is a 25 point adjacent-average guide to the eye. (b) Another thinner film with the pronounced *Pendellösung* fringes on the (111) peak that fit a thickness of 140Å and a lattice constant of 6.467Å. The red line is a fit that is described in the discussion section and figure 5.16.

In-plane XRD was used to look at the surface texture. The most intense miller axis normal to the (111) axis is the ($\bar{2}$20) plane. The surface texture of Al_2O_3 has

hexagonal symmetry and as such the ($\bar{2}$20) peak would repeat every 60°. This can be confirmed by scanning across Φ. Figure 5.7 has the ($\bar{2}$20) peaks repeating every 60°, where each peak is sharp with a FWHM of 2.1°. The precise separation angle expected for a hexagonal substrate and the sharpness of the peaks reveals a high selectivity for the expected orientations. Planes ($\bar{2}$20), ($\bar{2}$20) and ($\bar{2}$20) are all normal to the (111) and each is separated by 60°. Along the (111) axis each plane is a hexagonal tilting of pure constituent elements of the HHA. Thus if two islands meet during growth that started 60° apart the stacking will be indistinguishable as if it had started as 0°.
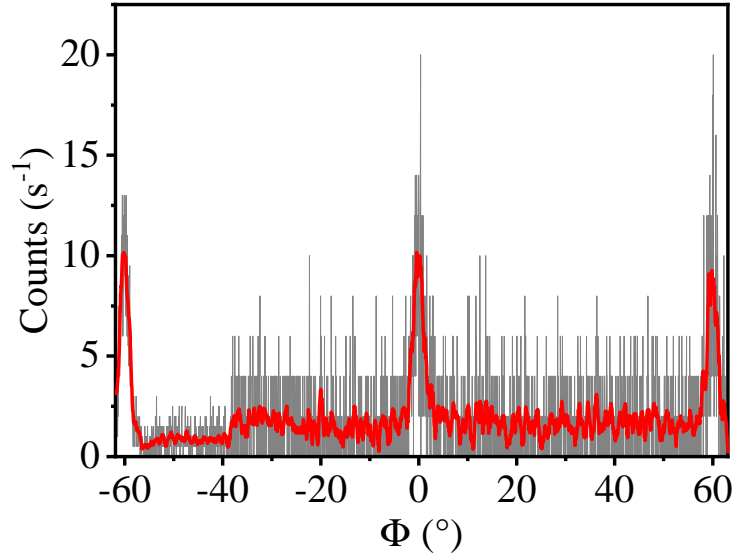
Figure 5.7: The (220) in-plane peak as measured as a function of Φ , the peaks only appear every 60° as the substrate has hexagonal symmetry. The red line is a moving average as a guide to the eye.

In figure 5.8 the in-plane lattice constant near $\chi = 90°$ is marginally above the bulk value. Given that this is a surface sensitive measurement it indicates partial relaxation of the thin film. The lattice constant near the substrate may potentially be larger than is measured by in-plane XRD.

5.2.2 Cross-Sectional TEM

In figure 5.9.a the image shows clear individual layers but there is no obvious periodicity along a layer line. It may be the case that this is off axis, looking at the substrate
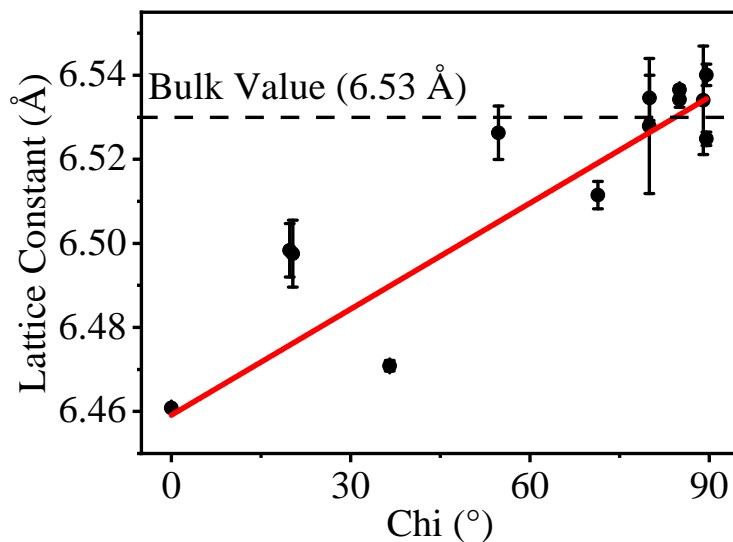
Figure 5.8: Changing lattice parameter as the sample is moved from in-plane ($\chi = 0°$) to out-of-plane ($\chi = 90°$). Lattice parameters and error bars calculated from fitting a normal distribution to x-ray diffraction peaks at the expected Chi angles for a (111) surface texture of YPtSb. The red line is a linear fit as a guide to the eye.
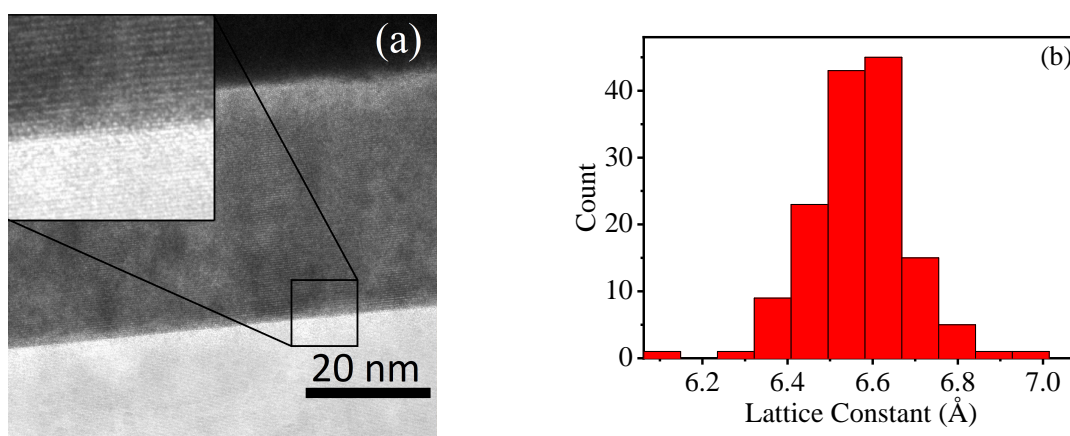
Figure 5.9: (a) cross-sectional TEM images of YPtSb thin films. The film has clearly defined layers starting at the substrate, the top surface is disordered. Disorder thickness was $\approx 4\,$nm, the film thickness $\approx 35\,$nm. (b) Histogram of the lattice constants as derived from 144 linescans over 6 different sections of the same sample.

it also lacks any in-plane periodicity. No obvious grain boundaries exist within this short section, although the last layers near the top are disordered. A distribution of lattice constants is calculated from Fourier transforms of many line scans over different sections of the same sample (Fig. 5.9.b). The mean lattice constant is 6.57 ± 0.07 Å and the skewness of the sample is -0.0465 tilting the distribution toward higher lattice constants. There was no correlation of the lattice parameter with depth inside the film. From this, it would appear that 35 nm is below the relaxation length for this pairing of the substrate and thin film. Although any relaxation would be most noticeable for the in-plane lattice constant which cannot be measured.
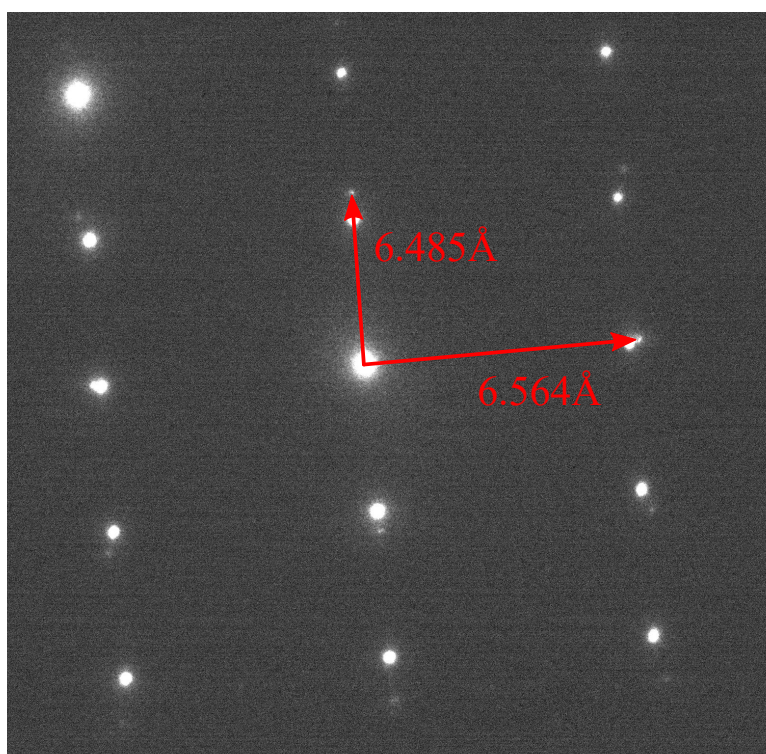
Figure 5.10: Electron diffraction of YPtSb from TEM. The thin film orientation is consistent with previous TEM images. The bright points are from the substrate, the satellite points are the thin film.

Changing to electron diffraction, the reciprocal space image shows peaks from both the substrate and the thin film. Ideally only the film would be measured but the minimum spot size for the electron beam is wider than the film thickness. Since the film was epitaxially matched the in-plane peaks for both the substrate and the YPtSb

were nearly merged. Out-of-plane diffraction peaks from the YPtSb were visible in comparison as no matching exists for the axis.

By measuring the substrate lattice peaks and assuming these should be bulk the image was calibrated. The lattice constants for the YPtSb thin film were 6.485 Å and 6.564 Å for the out-of-plane and in-plane directions respectively. These values are consistent with the XRD and real space TEM data. The in-plane lattice constant is also larger than that measurement by in-plane XRD as this measurement is sensitive to both the surface and buried interface where the film is under greater strain.
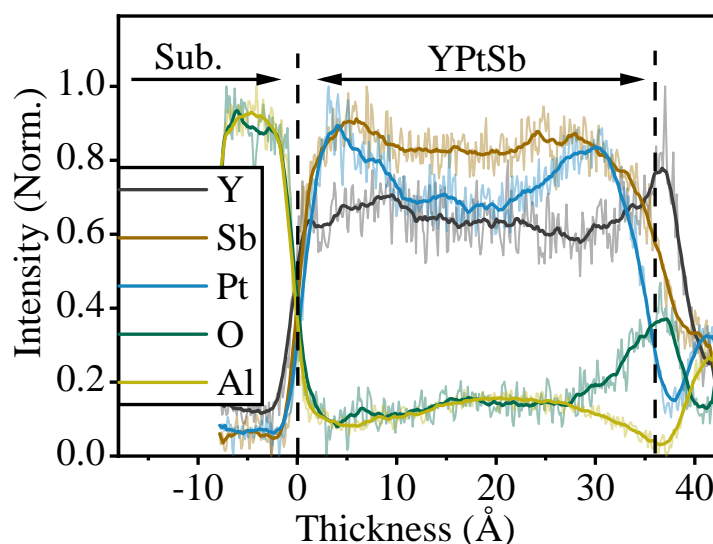
Figure 5.11: EDX line scans across the depth of the thin film of YPtSb. 0 Å is centered at the substrate and thin film interface. There is excess Y as well as oxygen at the thin film surface, ≈ 35 Å.

The relative composition of the constituent elements is approximately even across the thin film, the concentration percentages of Y:Pt:Sb across the thickness of the thin film were estimated to be 31.8% :20.2% :23.9% respectively. These do not sum exactly to 100% because of the inclusion or the apparent inclusion of Al and O, and at the surface excess Y has accumulated as seen from the peak in concentration. Very little oxygen migration from the substrate is seen at the interface, it is assumed that most of the oxygen in the thin film has come from the exposure to air. The excess Y at the surface may explain the disordered surface with oxygen inclusion seen in the real space

TEM image but that was not fitted be XRR (Fig. 5.9.a). The Genx model did not account for excess Y in the oxide layer so may have resulted giving a zero thickness oxide layer. EDX is a useful tool in determining the composition of a thin film, but it does not perfectly reproduce the relative intensities and if there is unexpected contamination it may not be obvious which element(s) it may be as element spectra peaks often overlap, particularly for heavy metals.

5.2.3   Growth of YPtSb on MgO

YPtSb grown on MgO (100) did not exhibit an epitaxial ordering as it did on Al_2O_3. The growth conditions were as near to identical as possible with the same power for each sputter gun, argon pressure, temperature and grown on the same day. The thin film on Al_2O_3 was grown first and the MgO second as the base pressure was lower, reducing potential contamination in the MgO sample. Despite these factors, the MgO (111) peak is 2 orders of magnitude weaker than the film grown on Al_2O_3 and there is also a (002) peak not previously seen in other YPtSb with Al_2O_3. It would have been surprising if YPtSb were to have formed along the (111) direction as it did in the samples made by the Shan *et al.* group [91]. It would be more likely that a square texture would grow on the (100) MgO substrate.

5.2.4   Electrical Transport

Figure 5.13.a has a positive MR curve that is expected for a normal metal. The carrier density is approximately 3 orders of magnitude lower than for most other metals which are in line with the $\rho(T)$ of a weak semiconductor with thermally activated charge carriers (Fig. 5.13.b). This result is also consistent with a narrow bandgap semiconductor as an asymptotic resistance versus temperature does not occur at finite temperature. Fitting an Arrhenius law to resistivity below $20\,K$ gives a activation energy of $\approx 1\,meV$ which would be expected from the bandgap of a narrow semiconductor and is inline with results for the Ouardi *et al.*group. The small activation energy could also be explained be ionization of impurity sites.

$\rho(T)$ data down to $250\,mK$ has a repeatable drop in resistance with no hysteresis (Fig. 5.14). The onset point is too low to measure the magnetic properties with the VSM here at Leeds, as it is a He4 wet cryostat, so it is not possible to probe any magnetic properties such as the Meissner effect or ferromagnetism. The highest current
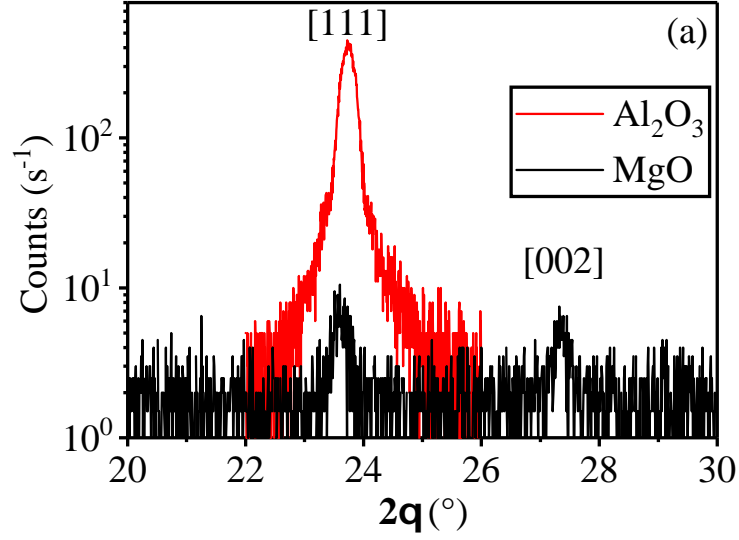
Figure 5.12: HAX of YPtSb grown on Al_2O_3 and MgO. Samples are grown one after another with the same parameters.
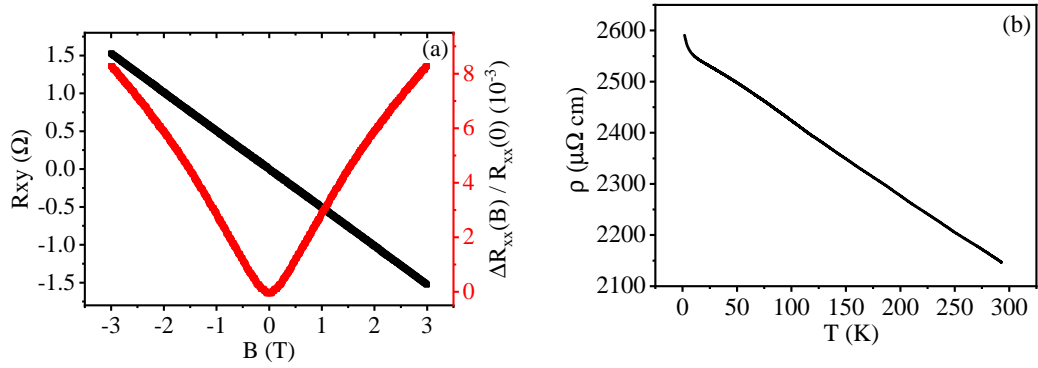
Figure 5.13: (a) MR and Hall measurements of 24 nm YPtSb on c-plane sapphire at 1.9 K. The carrier density is 6.18×10^{20} cm^3 and mobility is 6.067 cm^{2}V^{-1}s^{-1}. (b) Linearly decreasing resistivity as a function of temperature is expected for a weak semiconductor/semimetal with an upturn below 20 K.
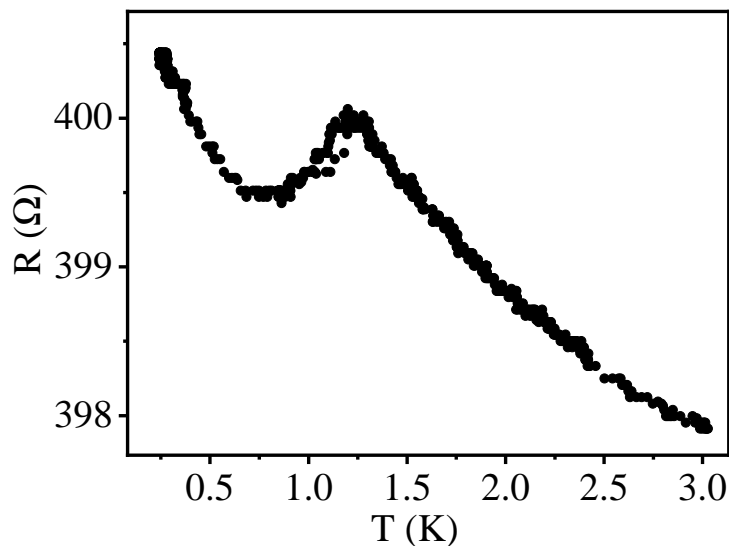
Figure 5.14: R(T) down to 250 mK of a thin film of YPtSb with a slight down turn at 0.4 K, the step can be retraced in temperature eliminating transient contact resistance changes.

used was 1 mA at 1 K which did not see a critical current point, a higher current would have had a detrimental effect on the thermal stability at very low temperatures. The limited change of the resistivity ($\approx 0.25\%$) and the lack of a critical current near the T_C constrainted the allowable volume of any potential superconductivity to a tiny volume fraction of the sample.

5.3 Discussion

The *Pendellösung* oscillations on the (111) peak were not symmetric as might have been expected for a single crystal thin film. We find that the asymmetry can be accounted for by a distribution of lattice constants and film thicknesses.

$$S(q) = \frac{1}{N} \frac{\sin Nqa/2^2}{\sin qa/2^2} \tag{5.1}$$

To fit the *Pendellösung* oscillations in figure 5.6.b we took the summation of an ensemble of parameters for the Scherrer equation (Equ. 5.1), where both the lattice constant, a, and the number of layers, N, was varied; along with a set weights for each

point. The scherrer equation is usually expressed in q-space. To create the relative weights for each member of the ensemble, gradient descent was used. The flow chart in figure 5.15 describes the process by using a randomly generated Gaussian to modifying the ensemble by a small amount. The modifier is tested and applied if it reduces the FOM. The width of the Gaussian is ranged from influencing a single point to large scale changes. This method works well for the assumption that final ensemble will be approximately continuous and neighboring intensities are positively correlated. This is repeated many times until the FOM has reach a minimum.
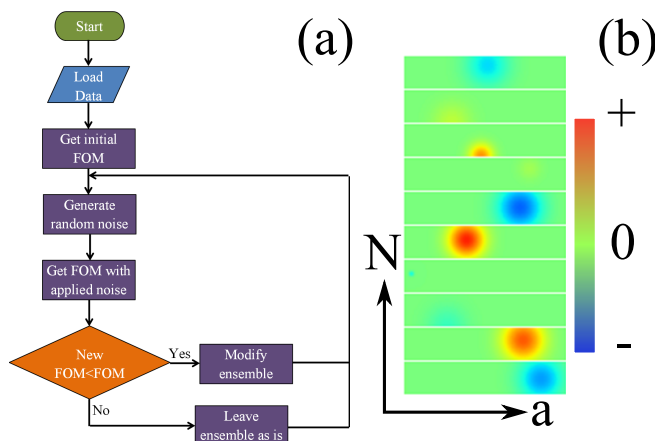
Figure 5.15: (a) Flow chart of the gradient descent program, it continuously tests and applies a small modification until the require fit is achieved. (b) A sample of the randomly generated Gaussians used to edit the ensemble map, N is the number of layers and a is the lattice constant.

The skewness from the TEM images and the heat map from figure 5.16 both lean toward the higher lattice parameters. The sign of the skewness may be the same but the TEM has a smaller skewness than the HAX heat map data (Fig. 5.16). This discrepancy could be either poor statistics of the TEM images with only 144 line scans, some having areas of poor contrast thus large uncertainty. Or the gradient descent could be stuck in a local minimum in parameter space which does not correctly represent the XRD data.

Figure 5.17 has the carrier densities for samples as a function of the FWHM. The correlation of the FWHM to the carrier density could suggest the grain boundary imperfections are adding additional charge carriers to the thin film. Converting from
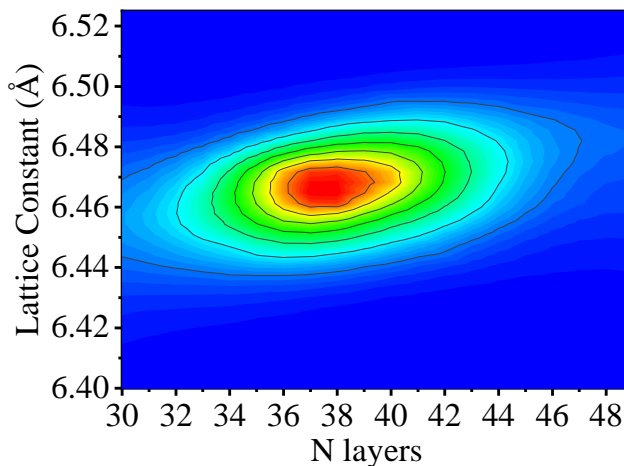
Figure 5.16: The heat map of the relative intensities of members of the ensemble after gradient decent optimization to fit the data in figure 5.6.b. The members are mapped out as a 2d heat map for the number of layers, N, against the lattice constant, a. The mean lattice parameter is 6.46 ± 0.03 Å with a skewness of -0.117.

cm^3 to nm as an approximate distance between carriers, for the highest carrier densities this comes to 0.66 nm for the highest densities and for the lowest 1.7 nm. The density of these charge carrier sources were on the scale of a single unit cell whereas the FWHM correspond to grains between $8 - 37$ nm. So many charges would need to be generate to explain these densities. With each unit cell having 12 atoms, potentially the charge carriers sites are located evenly across the film and on average slightly less than 1 atom in the unit cell is a source of carriers, either through a vacancy or substitution site. Possibly a form of anti-site disorder known to be an issue for 100% spin polarized HHA could generate the charge carriers [90].

Alternately, the charge carriers may originate from another source such as the disordered surface. Assuming the disorder surface is metallic with ≈ 1 carrier per atom and a similar density to the HHA structure then the thickness of the disorder film would need to be $\approx 8\%$ of the film thickness. The TEM cross-section shows a disordered thickness to ordered thickness ratio of 11% (Fig. 5.9.a). Thus the high carrier density could be explained by the presence of disordered surface charge carriers.

For the growth on MgO substrates, the (111) miller peak was two orders of magnitude weaker than for a near-identical set of parameters grown on Al_2O_3. MgO has
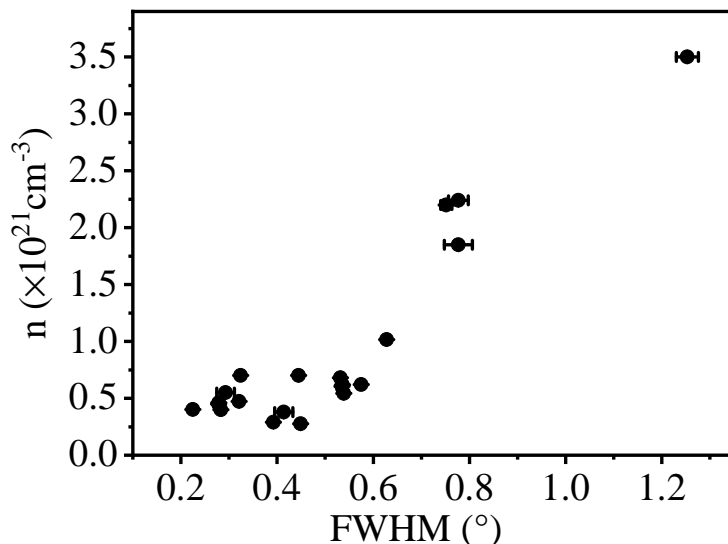
Figure 5.17: The strong correlation of the out-of-plane FWHM of the (111) peak with the carrier concentration as measured from the Hall effect at low temperature. The FWHM was measured at room temperature and the carrier density at $1.5 - 3\,\mathrm{K}$.

approximately twice the thermal conductivity of the Al_2O_3, as a result, the temperature of the substrate facing the sputter sources will be slightly hotter than compared to the Al_2O_3 substrate. While a slightly higher temperature would reduce the crystallinity, it would not explain the presence of the (002) peak. The Shan *et al.* group did use high temperatures than used here and it might be the case that good match of MgO only happens at higher temperatures. While their best result was a $800°\,\mathrm{C}$ they still saw ordered YPtSb at $600°\,\mathrm{C}$.

YPtBi is observed to superconduct at $0.77\,\mathrm{K}$ but no other group has seen superconductivity in YPtSb[19]. The small drop in resistance at $1.1\,\mathrm{k}$ is not expected to be a superconducting transition; if it were, it would need correspond to a vanishingly small volume (Fig. 5.14). Instead this resistivity drop may be related to a ferromagnetic or antiferromagnetic ordering similar to that found in YbPtBi that also has a small drop in resistance as seen in bulk crystals. Future work on YPtSb could study the magnetic properties at very low temperatures and in bulk samples to observe the same effect in resistance drop.

5.4 Conclusion

By using co-sputtering it is possible to grow high-quality crystals of YPtSb on c-plane sapphire that were well aligned to the substrate. The lattice mismatching induced a strain in the thin film and this was seen in both XRD and TEM. Although the carrier density remains too high and the mobility too low to see any surface states or quantum oscillations. We cannot confirm the linear dispersion bands, but we can agree on a small to zero bandgap by low energy thermal activation of charge carriers.

Some transport properties could potentially be improved by thicker films ($> 100nm$), although the crystal structure is not guaranteed to be continuously strained over a large thickness. Thicker films can only reduce the carrier density so far, even if it is assumed that the vast majority of carriers originated from the surface, the film thickness would need to increase by 2 orders of magnitude from our current thickness to reduce the carrier density close to bulk. Very large thickness as just suggested constitute a large commitment to a singular sample when the available sputter target materiel is limited. The disordered surface could potentially become ordered if a post-annealing step is taken, post-annealing is used extensively in the chapter on YbPtBi to mitigate the effect of a disorder surface. The poor transport properties may also be resolved by additional fine-tuning of growth conditions, some previous works have used lower temperatures but we found that to get good crystal ordering a higher temperature was needed.

High quality crystals do not always correlate to improved electrical properties, at higher temperatures the HHA phase may form more easily but also increases the number of vacancies and substitutions. The temperature may have been too high as compared to the Wang *et al.*group who used only 550°C in their growth, and potential issues with stoichiometry. Either post annealing or modifying the substrate surface through reconstruction may have allowed us to reduce the temperature further.

CHAPTER 6

Epitaxial Growth Of The Weyl Semimetal
YbPtBi (111) On C-plane Sapphire By
Co-Sputtering

Weyl semimetals are materials with a chirality split Dirac cone into Weyl nodes [113]. Using f-electrons in a HHA can lead to the formation of a Weyl semimetal state as the exchange field from the f-electrons causes the initial splitting of the Dirac point [61]. For the bulk, the chiral anomaly effect is created where chiral electrons are pumped from one chiral node to another and leads to a negative LMR [96]. This is an effective way to infer the presences of Weyl nodes in our thin films of HHA.

GdPtBi is a HHA with a predicted Weyl semimetal state, where it is the localized Gd f-electrons that split the Dirac point into two Weyl nodes of opposite chirality [44]. GdPtBi is an antiferromagnet with a Néel temperature at 8.5 K and was considered as a potential antiferromagnetic topological insulator before it was a Weyl semimetal candidate [54, 64]. When the Hirschberger *et al.* group grew single crystals of GdPtBi and measured the electrical transport, they observed a large negative LMR and deduced that it must be the chiral anomaly (Fig. 6.1). There was also a strong angular dependence on the LMR as the chiral anomaly only applies to parallel B and E fields. They therefore conjectured the presence of Weyl fermions.
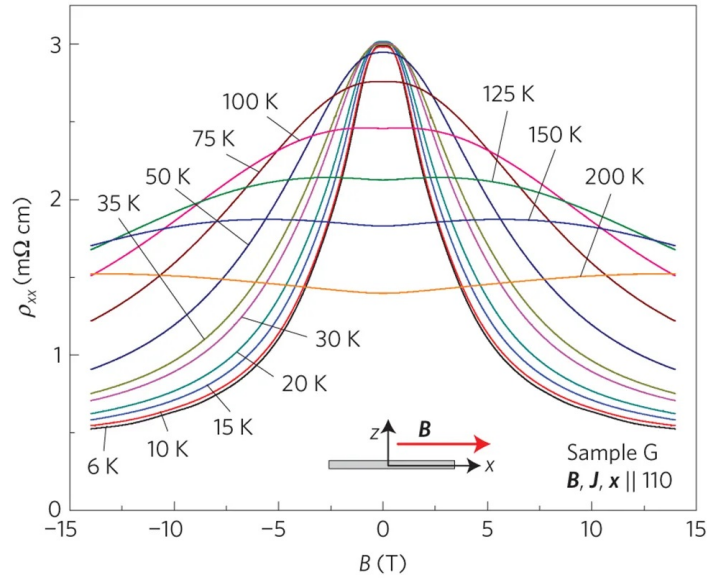
Figure 6.1: The LMR of GdPtBi at different temperatures. Figure from [44].

YbPtBi is very similar to GdPtBi and so was also predicted to be a Weyl semimetal. Although for YbPtBi the Yb, having a more filled f-orbital, has the moments more localised than GdPtBi and upon cooling becomes a heavy fermion system [30]. Several

groups have already grown YbPtBi as bulk crystals with these claimed properties of topological Weyl nodes and the chiral anomaly; antiferromagnetism from the RKKY coupling of localized Yb f-electrons at low temperatures; and heavy fermion behaviour - as those same localized f-electrons interact with the conduction bands [30, 40, 99]. The Guo *et al.*group have done DFT calculations and correlated those calculations with ARPES measurements. They also fit the chirality constant from the negative LMR to the theoretical temperature dependance and get values from that of $v_f^3\tau \ = 135\,\mathrm{m^3s^{-2}}$ and $\mu \ = 1.5\,\mathrm{meV}$ (Equ. 2.5). Where $v_f^3\tau$ is the cube for the Fermi velocity, v_f, and the chirality scattering time , τ; and μ is the chemical potential difference between the Weyl nodes.
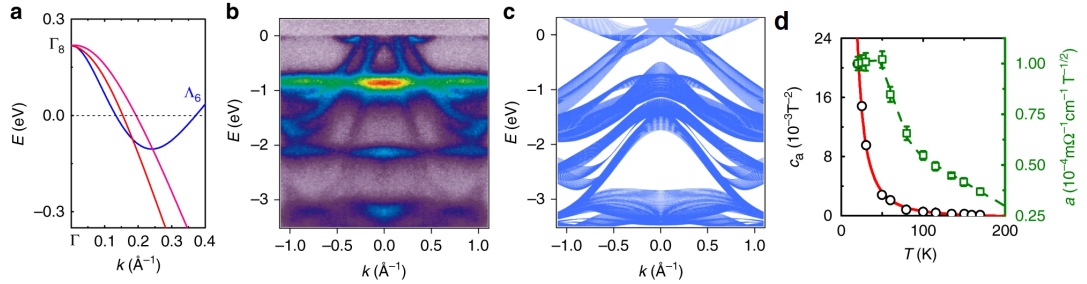
Figure 6.2: (a) DFT band structure calculation of YbPtBi, featuring a hole and electron pocket slightly away from the Γ point. (b) and (c) show the ARPES and the DFT calculation were in good agreement. (d) The chirality constant extracted from the negative LMR fitted with the expected temperature dependance. Figures from [40].

So far no examples of YbPtBi thin films exist and if high quality thin films can be produced it opens up the possibility of research that can be achieved with thin films such as: the effects of induced strain, device fabrication, doping implantation and so on. The ability to fabricate long and thin Hall bar geometry devices is of particular utility as one of the easiest to observe characteristics of the Weyl semimetal state is the negative LMR from the chiral anomaly [56], but current jetting effects can also produce negative LMR [27].

Current jetting is an induced anisotropic resistivity along the magnetic field direction having the effect of channeling the current through a small volume in the bulk crystal or in the case of thin films through a narrow channel (Fig. 6.3). Current jetting effects could be eliminated if the current path is confined in a narrow channel such

as a Hall bar with a high aspect ratio. This is where a thin film is most useful as a menagerie of options exist for fabricating hall bars into thin films,(Fig. 2.4). This is not the case with bulk crystals, where cutting a high aspect ratio bar is very difficult, even worse is that for a bulk sample the current path is buried within the sample.
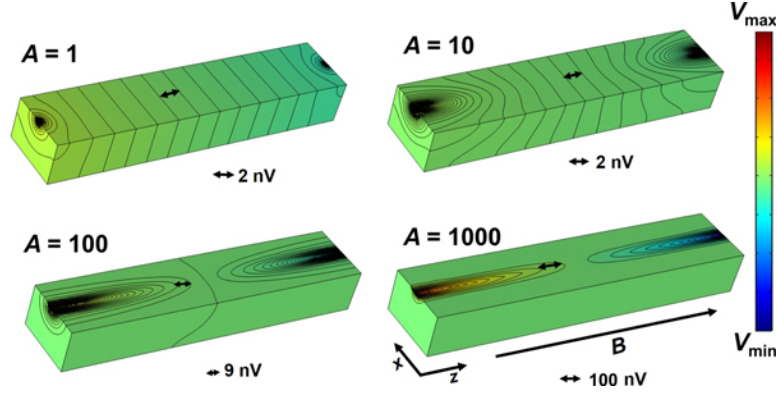
Figure 6.3: An illustration of current jetting, the vertical false colour scale is the voltage and is divide into equipotential lines. Voltage contacts placed on the edge of the sample would measure a drop in voltage as the equipotential lines move deeper into the film because of the increase in the conductivity anisotropy constant A. If sample was longer and thinner the measured resistance would be less sensitive to the factor A. Figure from [27].

In this chapter, we present a study of epitaxially grown YbPtBi thin films that grew as triangular islands with matched faceted edge orientations. The structure is confirmed to be epitaxial from out-of-plane XRD, in-plane XRD and cross-sectional TEM. We also measure the electrical transport properties and find a non-metallic R(T) similar to the other semimetal RePtBi (Re=Gd, Ce, Sm) HHA, although different from bulk YbPtBi. Negative LMR and the temperature dependence of an apparent chiral anomaly are strong indicators of a Weyl semimetal state. We also obverse a large hysteretic MR at very low temperatures not previously seen in YbPtBi.

6.1 Experimental Details

Thin films of YbPtBi were grown by DC magnetron co-sputtering in a pure Ar (6 nines) atmosphere of 5×10^{-1} Pa from pure metals targets of Yb (99.9%), Pt (99.95%) and Bi (99.99%), the typical base pressure was 5×10^{-6} Pa. The substrate was

(0001) c-plane sapphire which has a 2.5% lattice mismatch with bulk YbPtBi across the (111) plane [83]. Substrates were cleaned with 5 mins of acetone and isopropanol ultrasonic cleaning before loading into the chamber. Samples were transferred to the heater stage and outgassed at $650°$ C before cooling to $(575 - 625)°$ C for film growth. After depositing they are left to anneal briefly for 5 mins within an Ar atmosphere before finally being cooled down at $50°$ C/ mins.

It was also found that by depositing a monolayer of Pt first before the rest of the film, it would improve some aspects of the crystal quality by acting as a seed layer, although there is also a small component of the densest (110) out-of-plane when used. The Pt seed layer was indented to prevent island formation but had no effect. Samples were capped with a tantalum nitride (TaN) layer by reactive sputtering from a pure tantalum target in a 50/50 mix of Ar/N_2, TaN prevented oxidation and as an insulator would not have affected the electrical transport (Ch. 3.2).

X-ray diffraction measurements were preformed on a Bruker D8 using an additional ξ and ζ motion stages to align samples for in-plane measurements. Electronic transport above 1.8k was measured in a He VTI cryostat using a 6 point method with a split 3 T superconducting magnet, the MR and Hall measurements are decomposed into the symmetric $(\frac{a+b}{2})$ and antisymmetric $(\frac{a-b}{2})$ compounds respectively to eliminate misalignment from the voltage contacts. The contacts geometry is set up so a $90°$ rotation of the sample holder changes from longitudinal to out-of-plane without exchanging contacts. For electrical measurements down to 250mk a He3 sorption pump refrigerator was used with the same contact method and an 8 T solenoid superconducting magnet. Rotation inside the dipole magnet did not change field orientation so a change of contact geometry was needed instead.

6.2 Sample Optimization

For optimization, attempts to use a lower temperature were unsuccessful as seen in figure 6.4. The lower melting point of Bi over Sb and the rapidly increasing vapour pressure of Yb make higher temperatures unfavorable because of wetting behaviour and material loss. The bulk melting point of YbPtBi is $775°$ C and the thin film growth temperature needs to be a sizable fraction of the melting point [66]. For the lattice constant there is no clear trend as a function of temperature as there was for the YPtSb. The lattice mismatch is smaller for YbPtBi than for YPtSb so any changes from epitaxy
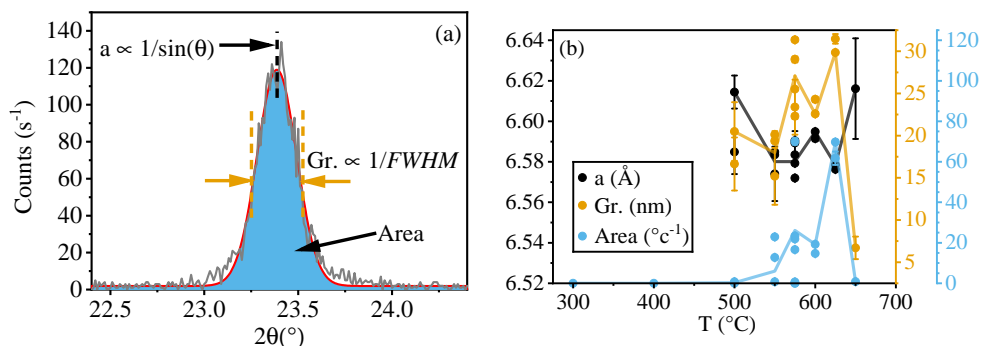
Figure 6.4: (a) Parameters taken from the XRD of the (111) peak of YbPtBi as important optimization metrics, Lattice parameter (a) and Grain size (Gr.) fitted with Bragg's law and the Scherrer equation respectively. (b) The optimization for YbPtBi thin films as a function of temperature. Solid lines are moving average as guides to the eye.

are smaller. The area under the (111) peak and the estimated grain size are mazimized at approximately $600°$ C. The rest of the samples shown here were grown close to this temperature range.

6.3 Results on Optimized Samples

6.3.1 X-ray Diffraction

Out-of-plane XRD of thin films of YbPtBi without a Pt monolayer only had peaks of the $< 111 >$ directions and higher multiples, all other miller directions were orientated at some other angle to the surface normal (Fig. 6.5.a). The out-of-plane lattice parameter was only marginally shorter than that of the bulk value (6.595 Å) [83]. The in-plane lattice parameter was larger as it has expanded to match the sapphire substrate. The unit cell volume of bulk YbPtBi is 286.84 Å^3, and from the measured in-plane and out-of-plane lattices constants our unit cell volume was 287.80 Å^3. If it is assumed that composition was correct and there were no vacancies then our samples have a density of 99.7% of bulk. XRR could be used to get a direct measure of the density if it was not for the island formation discussed later (Fig. 6.7.a). The difference in lattice parameters nearly cancels out to match that of the bulk, as the lattice stretches in-plane it must also shrink out-of-plane to maintain the same unit cell volume. The

FWHM for the (111) peak was 0.252° and 0.294° with and without a Pt monolayer respectively. With the addition of Pt monolayer, a small (220) peak is present where no peak is seen in the data without a Pt seed layer. The fractional volume that is oriented along the (220) axis can be approximated by comparing the relative intensities powder diffraction peaks and the measured peaks, giving a 0.6% fraction of (220) orientation [53].
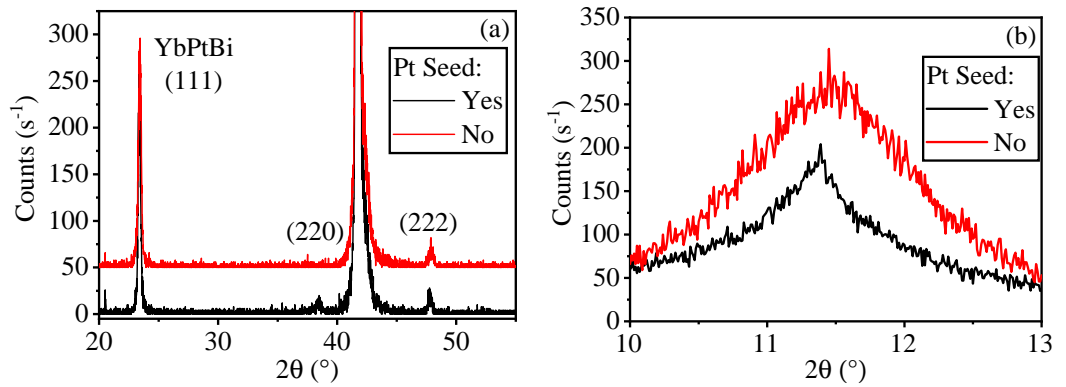
Figure 6.5: (a) With the Pt monolayer the XRD has mostly the (111) orientation visible with a smaller peak for the (110) (Black), when lacking a Pt monolayer it strictly only has the (111) peaks (Red). The out-of-plane lattice constant is 6.583 Å and in-plane is 6.612 Å. (b) Rocking Curve over the (111) peaks with and without a Pt monolayer.

The YbPtBi thin film matches the orientation of the substrate with the expected 60° repetitions in the Φ axis, with and without the Pt monolayer (Fig. 6.6). The Φ scan peaks are sharp with very little broadening and no peaks in between the ones at multiples of 60°. As with the YPtSb chapter this is a strong indicator of matching the substrate surface texture. The rocking curve with the Pt monolayer was weaker but also overall narrower, the wider the rocking curve the less aligned the film is to the substrate as it represents a wider distribution of angles.

Again this material was also growing epitaxially just as the YPtSb thin films did in the previous chapter. XRD can only get an ensemble average of the thin film. Microscopy is needed to observe the microstructure where, as will be seen, the situation changes from the relatively smooth films of YPtSb to the island growth of YbPtBi. This has already been indicated by the absence of strong *Pendellösung* fringes on the (111) XRD peak that this cannot be a smooth thin film.
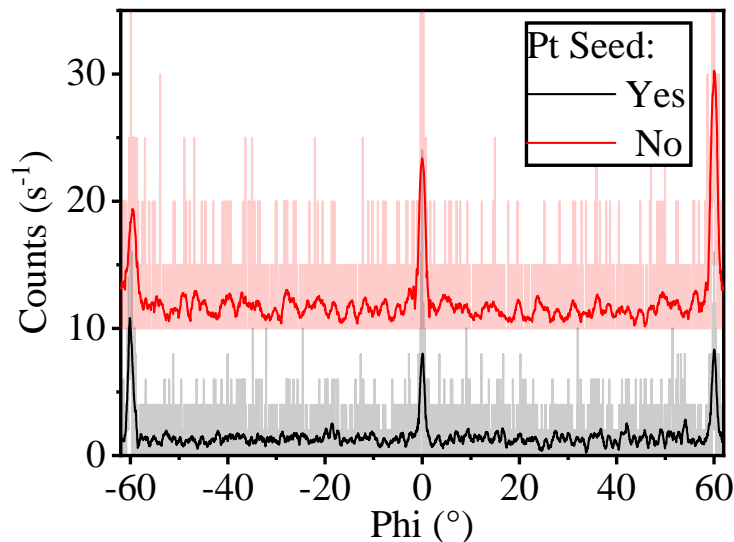
Figure 6.6: Φ scan for the (110) peak in-plane with and without a Pt monolayer, the data is centered to the substrate a-plane position and repeats every 60°. The data is partially transparent with a solid moving average overlay as a guide to the eye.

6.3.2 Cross-Sectional TEM

The growth process of YbPtBi was to form equilateral triangular islands that all shared the same facet orientations observed by SEM (Fig. 6.7.a). This correlated facet orientation is inherited from the hexagonal symmetry of the c-plane sapphire surface. The triangles are randomly placed and have clear gaps that expose the substrate.

Epitaxial matching is clear in the TEM images from inside one of these islands, the thin films have formed clear rows and columns of aligned crystal structure with the same width of the substrate beneath it (Fig. 6.7.b). Previously in the YPtSb chapter the alignment in-plane was not good enough to observe periodicity. This is now possible with these images with periodicity visible in both the substrate and thin film. Comparing the substrate pattern to TEM images of other groups and crystal projections we can say that this is the a-plane and that this is an image of the (110) thin film plane as would be expected [25]. The TEM image is calibrated assuming that the substrate is bulk like. The unit cell volume from the lattices parameters in figure 6.7 is 286.5 Å^3, are again very similar to that of bulk.

Yb and Al have an overlapping energy spectral edge from the Yb M4 (1.5763 KeV),
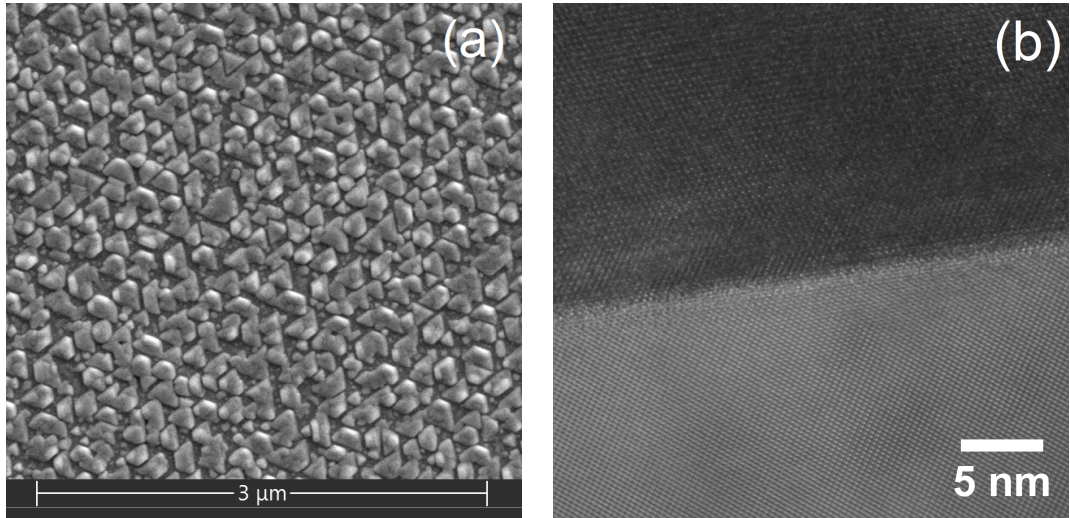
Figure 6.7: (a) SEM image of the surface of the thin film, the edges of the triangles are all similarly aligned. (b) Cross-sectional TEM of one of these islands, the lighter half was the substrate and the darker half the YbPtBi. The lattice spacing was $6.509\,\text{Å}$ out-of-plane and $6.634\,\text{Å}$ in-plane.
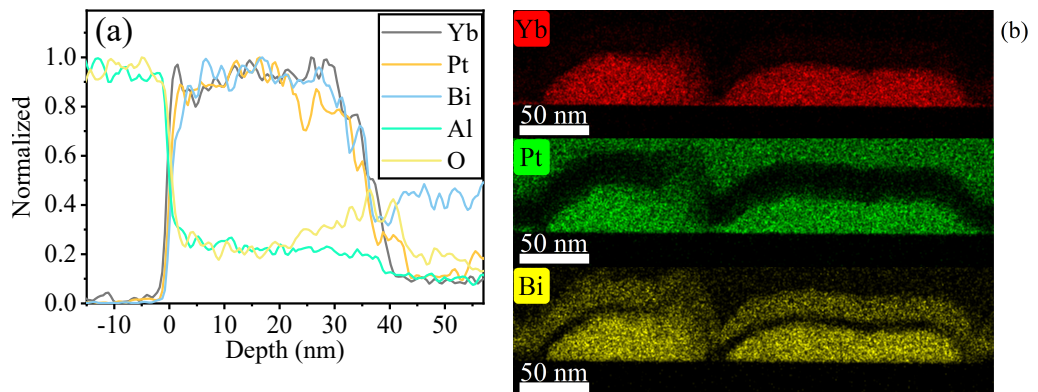
Figure 6.8: (a) Normalized intensity of a cross-sectional depth profile of the relative chemical compositions from an island of YbPtBi. (b) Stacked images of Yb,Pt and Bi chemical EDX profiles across a cross-section of two islands. For TEM preparation the sample is covered in an Ir cap and a Pt/C layer, both of which are visible in the Bi and Yb chemical channels respectively.

and Al K (1.5596 KeV) edges giving rise to an apparent Al inclusion inside the film where none exists (Fig. 6.8.a) [71]. The reverse of confusing Al for Yb does not happen as no Al spectral edges overlap with the main Yb peaks such as the K or L edges. The preparation for FIBSEM to cut the TEM cross-section sputters an Ir cap, Ir (L1=13.4185 KeV) and Bi (L3=13.4186 KeV) also have overlapping edges which make it look as if Bi is covering the top layer surface. Oxygen inclusion was at least partly real as the cross-sectional sample was transferred from the FIBSEM to the Titan TEM in air. Unlike YPtSb there were no excess elements on the film surface and each element is approximately uniform across the depth of the film. Excluding the Al and O from within the island EDX composition of Yb:Pt:Bi was $35 \pm 1\%$: $32 \pm 3\%$: $32 \pm 1\%$ respectively. This is within the expected error of an EDX measurement and so the stoichiometry is reasonably consistent. In between the islands there was some Pt and Yb but no Bi.

6.3.3 AFM

From the SEM images it is clear that we had an issue with island growth. By growing a much thicker sample we looked to see if these islands would merge into one continuous thin film and if the Pt seed layer would have any effect on island formation. Figure 6.9 has AFM images of both the usual thickness and a film approximately 3 times thicker. In the thinner film, the islands are separated with exposed substrate as seen before in the SEM image, in the thicker sample all of the islands merged into a rough surface with very little substrate exposed. From this we achieved an almost fully connected thin film that would prevent erratic current paths. Unfortunately this thicker sample suffers from poor optimization. The area of the sample with good islands was located under the partly occluded area of the sample shutter, here the Yb source was limited. The total area of these merged islands was very limited and approximately 1 mm in width. The addition of the Pt seed layer did not stop island formation in an meaningful way. The triangular islands were not as clear as before but are still present, it is unclear whether this is because of the Pt seed or slight differences in growth conditions.

6.3.4 Electrical Transport

The resistance versus temperature is unlike that expected for a normal metal with a typical linear phonon scattering reduction toward lower temperatures (Fig. 6.10). It
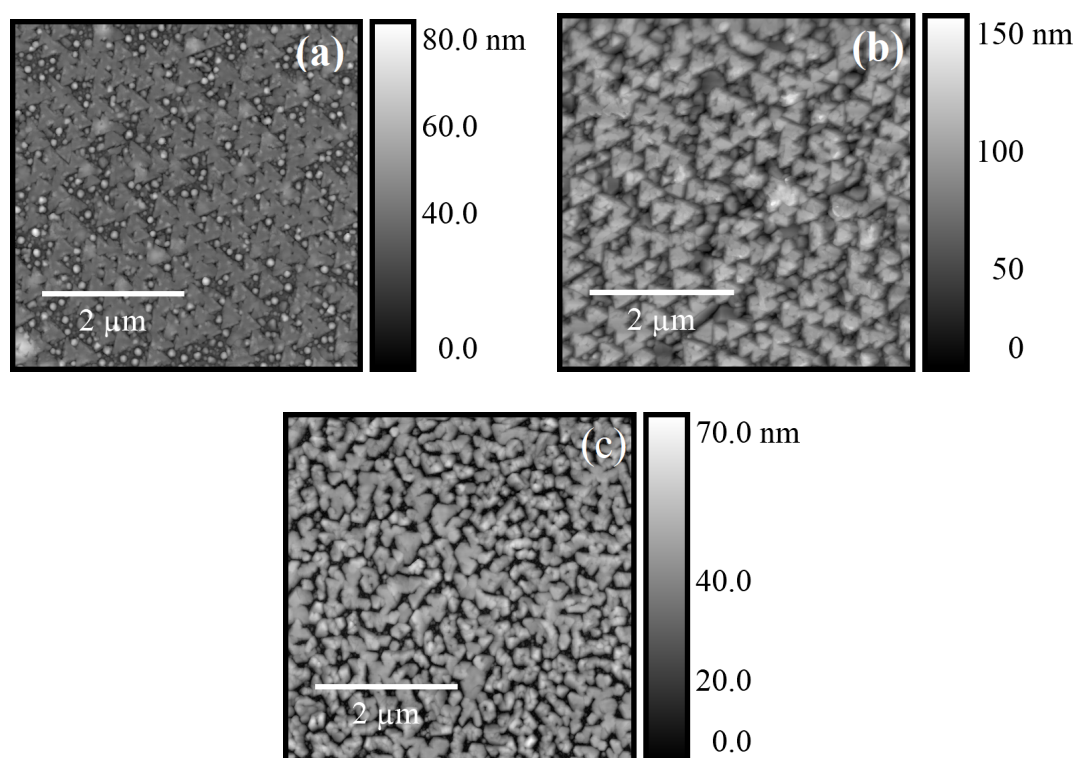
Figure 6.9: AFM images sample of YbPtBi, (a) thin film of the usual thickness and (b) is $\approx \times 3$ thicker. (c) The island formation with a Pt seed layer. Triangles are less clear but still present. None of the images had tip convolution artifacts as the same structure exist in SEM images and some features are not triangle shaped. The only exception is possibly the narrow holes in (b) that reach to the substrate. The zero of the depth scale is at or near the surface of the substrate.

did however share some of the features of the other rare earth, RePtBi (Re=Gd, Ce, Sm), compounds studied that have elements from the top of the f-block [44, 50, 52]. Each of these curves has a peak in resistivity located at different temperatures. The resistance peaks at 190 K falling quickly toward lower temperatures and slowly toward higher ones, the overall resistivity is an order of magnitude greater than bulk [65]. In comparison, in the bulk there is no evidence of a change in slope near 190 K and resistivity does not reach a peak [41].
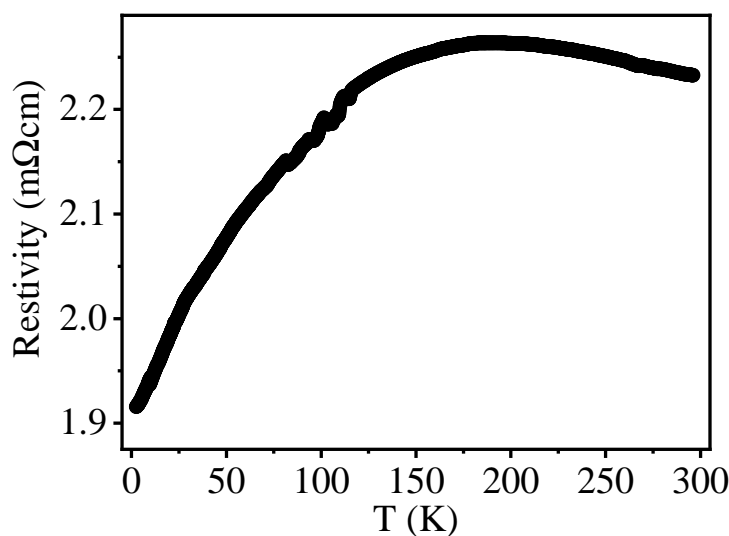
Figure 6.10: Resistance versus temperature of YbPtBiwith a Pt seed layer. Extra noise at ≈ 100 K from a poor contact.

Figure 6.11 contains the dependence of the carrier density and mobility as a function of temperature up to 120 K. The carrier is p-type and is 10 times larger than the bulk crystal values of other groups. The lowest temperature Hall data shows a nonlinear component, this could be an effect of a two band system (Fig. 6.11.b). As is predicted by DFT, there are both hole and electron pockets as sources of charge carriers (Fig. 6.2.a). Attempting to fit the non-linear Hall resistance with a two band model is not possible without an independent measurement to constrain the mobility or carrier densities [6]. Additionally the mobility is too low to observe any effect of the SdH oscillations that could give independent information about both n-type and p-type charge carriers or mobilities. Any hysteresis in the hall data is assumed to be an artifact of temperature drift.

The non-linear shape could be explained by either the anomalous Hall effect (AHE) or the topological Hall effect (THE). We did not observe significant evidence of a ferromagnetic hysteresis loop as measured by VSM or in the MR, so an AHE would be unexpected. The THE contribution at high field should reach zero, so to correctly identify this non-linear shape as the THE much higher fields would be needed.
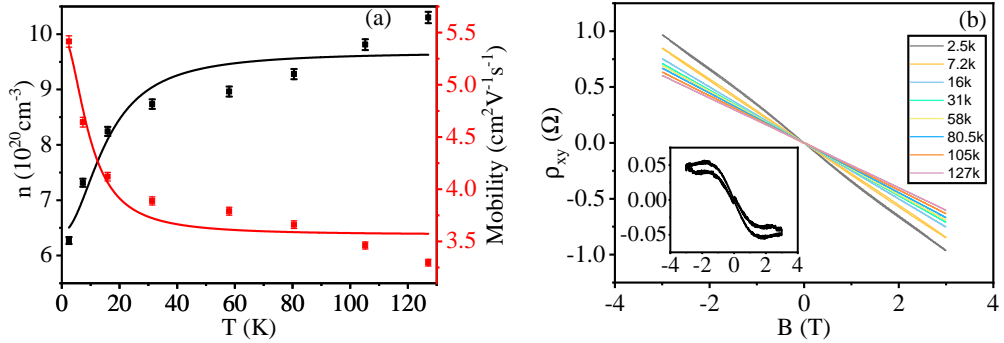
Figure 6.11: (a) The carrier density and mobility dependance on temperature, solid lines are fits to an Arrhenius exponential for later comparison. Typical error of the carrier density is $\pm 8 \times 10^{18}$ cm^3 and mobility is $\pm 0.04\,\mathrm{cm^2V^{-1}s^{-1}}$, dominate by the hieght uncertianty as measured by AFM (Fig. 6.9.c). (b) The Hall effect at each temperature, the inset is the $2.53\,\mathrm{K}$ data with the linear slope removed showing non-linear components.

At low temperatures, $T < 30\,\mathrm{K}$, there is a sharp rise in mobility and drop in carrier density (Fig. 6.11.a). This could either be the freezing of impurities sites in which case as the temperature decreases less of the impurity sites are ionized reducing the carrier density and that also has an effect on the mobility as these act as scattering sites. Or this could be a narrow/zero bandgap for a semimetal. The energies needed to move charge carriers to a mobile unoccupied state in any semimetal is small thus corresponding to a low temperature.

Figure 6.12.a has the MR data from a YbPtBi thin film with a TaN cap and Pt seed layer. The equation used to fit the chirality constant was described in the theory section (Ch. 2.4). This method of fitting is the same as previously used for bulk YbPtBi [40]. From figure 6.12.b it was expected that the negative LMR would become a positive MR out-of-plane where the Hall resistance reaches a minimum/maximum, instead the difference is small and the out-of-plane MR is only marginally smaller than the LMR.
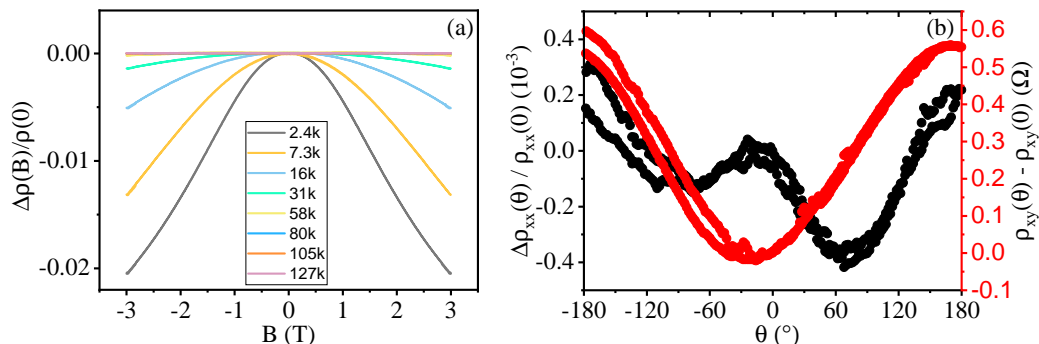
Figure 6.12: (a) LMR of YbPtBi at several temperatures, below 20 K the curve deviates from a pure parabolic function at high fields. (b) Angular MR and Hall Effect at 1 T field and 5 K, the field is perpendicular to the sample when the Hall resistance is at peak/trough.

This is attributed to the island growth and erratic current path as discussed later. The angular dependance of the MR should be be symmetry around a 180°. But because of the small difference between longitudinal and transverse MR, the contamination of the Hall effect from slight misalignment of voltage contacts causes some asymmetry. This contaminating is normally remove decomposing the MR into the symmetric and antisymmetry components.

The negative LMR signal is typical of a chiral anomaly and the chirality constants extracted from the MR fitted the temperature dependance expected from theory exceptionally well, bulk values of YbPtBi of the chiral anomaly give a chemical potential of $\mu = 1.5\,\mathrm{meV}$ and a chirality scattering time of $v_f^3\tau = 135\,\mathrm{m^3 s^{-2}}$ (Equ. 2.5), comparable to our thin films values [40]. The magnitude of the WAL also decreases with temperature as greater thermal energy inhibits phase coherent scattering. The lowest three temperature points for the WAL as missing due to poor fitting as the negative LMR dominates the shape of the MR.

We are confident that current jetting is not an issue as the temperature dependence of the chirality constant is consistent with theory and previous bulk sample values with the addition of a much shorter chirality-changing scattering time (Fig. 6.13). Additionally, the negative MR does not change by changing the contact positions and is consistent across multiple samples, thus the current distribution is predominately uniform across the sample. The film is also not thin enough to be considered 2D for
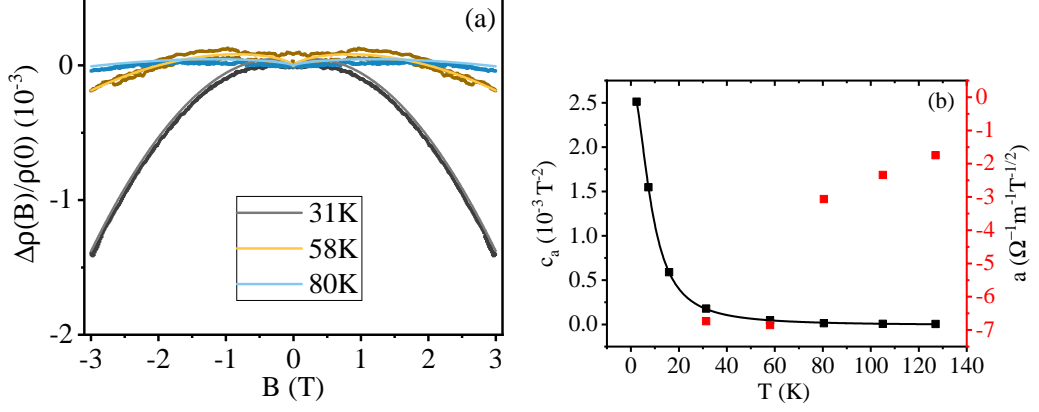
Figure 6.13: (a) Some LMR sweeps that the chirality constant is extracted from by fitting a negative parabolic MR with a WAL component, the solid lines are the fitting curves [40]. (b) The temperature dependence of the chirality constant, c_a, with the expected temperature dependence from theory, $\mu = 1.58\,\mathrm{meV}$ and $v_f^3\tau = 2.71\,\mathrm{m^3s^{-2}}$. The WAL constant, a, is shown in red on the right hand side where the last 3 points are missing to to poor fitting.

electronic transport as the mean free path given by $\ell = \hbar\mu\sqrt[3]{3\pi^3 n}/e$, where n is the carrier density and μ is the mobility, is about $2\,\mathrm{nm}$ much less than the film thickness. From this it follows that 2D effects can be ignored such as those that can also create a negative MR [4].

At very low temperatures, $T \approx 250\,\mathrm{mK}$, we observed a hysteresis in the MR of the YbPtBi that has a very large saturation point about $3\,\mathrm{T}$, this may possibly be a result of some type of magnetic ordering below a critical temperature (Fig. 6.14). Many of the half Heusler alloy family are antiferromagnetic at low temperatures and for YbPtBi the Yb f-electrons become sufficiently delocalized to exchange couple with each other [43]. A sharp increase in the resistance around $0.4\,\mathrm{K}$ might have been expected as it exists in bulk but is known to disappear with the presences of strain [65]. That increase in resistance is from a fragile antiferromagnetic regime that is destroyed by strain, for these thin films strain is inherent in the epitaxial growth [99]. Ferromagnetic ordering as opposed to antiferromagnetic order could be explained by the introduction of strain induced anisotropy. Ferromagnetism from antiferromagnetic epitaxial thin films has been studied in strained thin films before [62, 109].
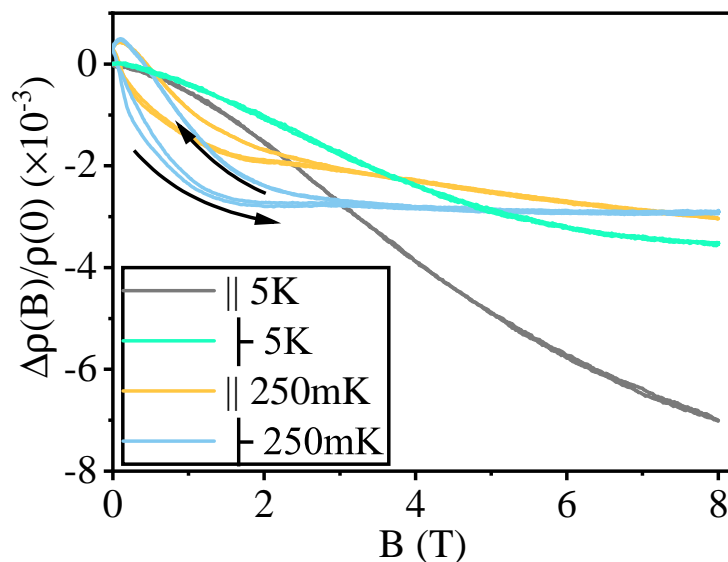
Figure 6.14: Longitudinal and transverse MR of a YbPtBi thin film without a Pt monolayer at 250 mK has a negative MR and a hysteresis up to 3 T.

The magnitude of the negative MR is also weaker at very low temperatures. Given the temperature dependence of the chirality constant at higher temperatures it might be expected to be larger. Instead this could be more evidence of the delocalization of the f-electrons at low temperatures. As these delocalize the effective mass increases and v_f decreases. Since the Chiral anomaly is dependent on the factor $v_f^3 \tau$ there is a reduction at low temperatures as the f-electrons increase the effective mass (Equ. 2.5). This process fits with the bulk model suggested by the Guo *et al.*group [40].

6.4 Discussion

The Pt monolayer made the rocking curves and FWHM of the (111) peak is sharper, implying a more coherent orientation and consistent thin film. Although it also allowed some (110) orientation as that is Pt densest plane. One of the motivations for growing a Pt seed layer is that it may stop Yb binding strongly to the surface as seen by EDX (Fig. 6.8). Our thinking was that Yb is a reactive metal tarnishing quickly in air and was binding to oxygen at the surface of the Al_2O_3. Without the Pt layer Yb would bind to the surface slowing/ stopping the growth of YbPtBi. The ultimate goal was to

change the surface energy and prevent island growth which failed as it had little to no effect.

At ≈600° C the vapour pressure was greater than the sputtering pressure, as such adatoms of Yb are only persistent on the substrate when bound to Pt and Bi atoms. Island formation could be explained by the low melting point of Bi and the low vapour pressure of Yb as it evaporates and redeposits onto the substrate surface. Preferably a lower growth temperature would have been used but early optimization of temperature failed to show a YbPtBi phase, and it may be possible to bring the temperature down further if more time and target material is spent optimizing for it. The sensitivity of the Yb vapour pressure has the effect that sputtering power ratios optimized for one temperature are sub optimal for any other temperature. At lower temperatures Yb would remain on the surface longer with more time to form a YbPtBi phase. Additionally at lower temperatures the mobility of all adatoms would be reduced, possibly preventing island formation as new layers would stack faster than the time taken for adatoms to move into islands.

These islands were connected in a random network where the current path took an erratic path through the film. Percolation theory is about the connectivity of randomly placed objects in space, since our nucleation sites are random and each island grows to approximately the same size we can use percolation theory to describe our thin films. The Percolation threshold (ϕ) is the point above which there is long-range connectivity and is the ratio of circle area to empty space ratio. For the case of randomly placed circles the limit is $\phi = 0.676$ thus 67.6% of the space is covered with circles [58]. Taking the AFM image of the regular thickness film (Fig. 6.9), we can calculate $\phi \approx 0.6$ which is at the limit of the circle percolation threshold. The value of ϕ for circles is insensitive to the shape as long as the aspect ratio is close to 1 as it is for equilateral triangles.

Since MR is symmetric and orientation dependent the measured LMR will have contributions from the transverse and out-of-plane directions as the local current paths move around gaps in the film. Preventing island growth or merging the islands to have a more uniform film would eliminate this issue. Islands such as these are difficult to form into devices like Hall bars with the high aspect ratio discussed earlier. The Hall signal is always antisymmetric so locally small erratic current paths are less important as the sum over all current paths averages to a continuous current distribution on the scale of our samples (a few mm). In general the measured Hall response is proportional

to the total current between the two contacts and insensitive to the small changes in contact geometry as long as the Hall contact points remain close to the edge.

By growing the sample thicker the islands eventually merge into one continuous thin film as is seen in the AFM images (Fig. 6.9.b). A sample like this one has a good chance of direct current path from contact to contact, eliminating the issue with erratic current paths. Although this thicker sample still has large height variations and small portions of exposed substrate. The sidestepping to cross the film was still dramatically reduced in principle. Device fabrication with a film as rough as this is still an issue and stopping island formation would be a better solution if it were attainable.

Quantity	Chemical Potential (meV)
Chirality constant	1.584 ± 0.006
Hall Carrier Density	3 ± 1
Hall Mobility	2.1 ± 0.4

Table 6.1: The chiral chemical potential μ as calculated from equation 2.5. The energies for the carrier density and mobility are calculated from a thermal activation type behaviour, $\propto exp(\frac{-E}{2KT})$, from the data in figure 6.13.a.

The fitting of the chirality temperature dependance was very accurate to what we have measured and similar to previous bulk values (Fig. 6.13). This gives us strong evidence for a Weyl semimetal state within our films. Even so it is still possible some other effect may produce these results. The function for the chirality temperature dependance is derived for the thermal activation of chirality flipping scattering, so these thermal activation processes can correlate to other thermal processes of scattering like that of phonons. Fitting a $\propto exp(\frac{-E}{2KT})$ type trend for the carrier density and mobility temperature dependance we can get associated energy scales typical of thermally excited carriers in a semiconductor (Fig. 6.11.a). Getting an energy scale from the mobility in the way is not necessarily entirely physical, in particular because the Hall and mobility data are strongly correlated, but can give some idea about if the apparent chiral anomaly observed has process based on mobility. More important is that similar energies lead to similarly shaped trends with temperature as the down-turn or up-turn in the carrier density or mobility respectively occur at similar temperatures and rates, leading to a strong correlation and the indication of a causal link.

Table 6.1 contains the fitted energies, the carrier density is larger than that from the

chirality constant thus can be disregarded, but the mobility had nearly the same energy scale within the quoted error. Therefore the reduction in the negative LMR at higher temperatures could be attributed to an increase in scattering and not purely a lose of an apparent chiral anomaly. The reverse could also be that the thermal chirality scattering would lead to the reduction in mobility, but that would imply majority of scattering is involve in chirality flipping. The reduced χ^2 for fitting the chirality constant and the mobility are 1.75×10^{-11} and 0.035 respectively. The goodness of fit could be used as evidence for the validity of the chirality temperature dependence over the mobility temperature dependance.

6.5 Conclusion

We have demonstrated the successful growth of YbPtBi on c-plane sapphire by DC magnetron co-sputtering. Our thin films of YbPtBi show transport properties such as negative LMR that could be interpreted as evidence of a chiral anomaly and as such of Weyl nodes. With the island growth at the percolation limit, the current path is erratic and the MR signals are a mix of many directions, explaining why the MR is also strongly negative in the transverse geometry. At very low temperatures there exists a hysteresis in the MR with a large saturation field ($3\,\mathrm{T}$) not seen before in this material.

CHAPTER 7

Conclusion

7.1 Conclusion

Within this work we have used heavy group V elements along with high Z Pt to construct systems of high SOC in an effort to generate non-trivial topological materials. In doing so we found the unstable interfaces of Bi/Ni bilayers that anneal at room temperature and have grown high quality epitaxial thin films of YPtSb and YbPtBi. While neither of these thin films have shown evidence of non-trivial topology, YbPtBi has signatures of a possible Weyl semimetal state.

Our studies of Bi/Ni bilayers have confirmed the presence of the BCS superconducting alloy $NiBi_3$ at the interface. The $NiBi_3$ was formed post growth by annealing at temperatures as low as room temperature over a few days. At higher temperatures $(+50^\circ \text{C})$ the annealing time would be dramatically reduced (≈ 1 hours). Previously the interest in Bi/Ni bilayers was for clean distinct layers where the superconductivity was coming from some effect of interfacial superconductivity. With our results we suggest that unless great care is taken to prevent heating during the growth, long-term storage, post processing and during measurement then the desired interface will degrade. Many cleanroom device fabrication process require heating to bake resist or lift-off, any of which would fully anneal a sample.

For our work of the HHA we successfully grew thin films of YPtSb and YbPtBi. We found good epitaxial matching to the substrate and for YPtSb the films formed smooth and continuous films. While structurally the film was of high quality with *Pendellösung* fringes indicating single crystals, the electrical transport properties where not as profound. While the thin films did display behaviour to that of a zero gap semiconductor, it did not show any indication of nontrivial topology. The carrier density was too high to observe any effect of potential surface states and the mobility too low for quantum oscillations that could have been used to infer a non-trivial Berry flux.

The work here on YbPtBi has evidence of a chiral anomaly with a temperature dependance expected for a Weyl semimetal. Although the angle dependance in the MR was not what would be expected for the chiral anomaly, it could be explained by the island growth and the erratic current path. The triangular islands are side effects of epitaxial growth and high mobility of Bi and high vapour pressure of Yb, the islands form a network of loosely connected islands near the percolation limits resulting in an erratic current path.

7.2 Future Work

Bi/Ni bilayers could be studied further to look for unusual superconductivity that we had initially failed to see. The residual magnetism allows for a potential triplet pairing superconductivity with an orbital moment component for strong SOC. It would be advantageous to now grow clean interfaces on cooled samples and keep them cold through the measurement process. While we could not grow a completely clean interface initially for measurement, we would not expect a superconducting transition until after annealing.

A Joseph junction type device made of a clean interface would be a very interesting system. By injecting cooper pairs into the junction the superconducting pair type can be deduced. In particular cooper pairs would first need to traverse the residual Ni layer, this would introduce an odd frequency triplet s-wave component to an otherwise even frequency s-wave singlet cooper pair [14]. By repeating the cooper pair injection after several annealing steps one could observe a transition from a ferromagnetic induced p-wave component to the s-wave superconducting $NiBi_3$ alloy.

The issue is creating a device without needing to bake polymer resists for typical device fabrication. Hard shadow mask could generate a pattern without any heat but the spatial resolution is limited and alignment between masks is never imperfect. Focused ion milling only causes localized heating for very short periods of time, ion milling is also a slow process and can not pattern larger areas. A combination of using hard shadow masks to pattern contact leads and then ion milling to create the fine device structure would be one possible option for device fabrication. Assuming that the local heat is insignificant for annealing and the implantation of ions is not detrimental to the superconductivity.

Both of the HHA studied here could have potentially had their transport properties improved by growing substantially thicker films. For YPtSb and possibly YbPtBi the free surface might have been a large source of the charge carriers, thus a thicker film would have been less susceptible to charge carriers originating from a disordered surface. Although ideally the free surface of the thin film would be perfectly ordered, capping with a highly thermally stable material with low diffusion and post growth annealing might allow for this. Additionally For YbPtBi a thicker layer would have allowed for more island merging and a continuous thin film without erratic current paths. Growing thicker films introduces other problems. The growth conditions may not be stable over

a longer time period, at some critical thickness the epitaxial strain relaxes, and thicker films involve a greater expense of target material per thin film.

The low temperature magnetic ordering of both HHAs studied here is another interesting question that is not completely answered. To get an idea of the type of magnetism, very low temperature magnetometry would be needed to identify any stray ferromagnetic field or a sudden change in magnetic susceptibility at the Néel temperature. The dip in resistivity for the YPtSb could be explained by a magnetic order, although Y lacks any f-electrons so any magnetic ordering what have to come from the d-electrons. Neutron scattering would be useful to determine if it is also an antiferromagnetic ordering. Low angle neutron scattering has been used to measure the antiferromagnetic order at $0.4\,\mathrm{K}$ in YbPtBi [99].

Overall we have successfully demonstrated that co-sputtering can produce reasonable quality HHA and the techniques used could be applied to other HHA not trialed here. The lattice constants for many of the potential topological HHA are similar enough that many others should also have epitaxial matching to the same c-plane Al_2O_3. While it is possible to continue with sputtering and make high quality crystals, MBE is another well suited method for thin film growth.

Appendix A

Bi/Ni Bilayers PNR Box Model Fitting values

The full set of GenX fitting parameters for a $Ta_2O_5/Ta/Ni/NiBi_3$ /$Bi/SiO_2/Si$ box model. The Final two annealing steps can be fitted better by a NiBi layer in place of a pure Ni layer. The figure of merit (FOM) for each annealing step is shown, with a NiBi layer on the last two the FOM decrease to 1.167 and 1.807 for $1800\,s$ and $3600\,s$ respectively.

Parameter	0 s	150 s	300 s	600 s	1800 s	3600 s
FOM	1.421	1.341	1.415	1.404	1.174	1.877
Ta_2O_5: d (nm)	1.6 ± 0.3	1.2 ± 0.2	3.9 ± 0.8	2.4 ± 0.5	5.7 ± 0.8	4.0 ± 0.5
ρ (% bulk)	95 ± 6	102 ± 5	85 ± 9	89 ± 5	83 ± 3	118 ± 8
σ(nm)	3.8 ± 0.2	4.0 ± 0.1	4.4 ± 0.3	4.2 ± 0.3	4.4 ± 0.4	5.0 ± 0.2
Ta: d (nm)	4.9 ± 0.4	5.1 ± 0.7	3.9 ± 0.6	3.3 ± 0.3	3.5 ± 0.5	0.5 ± 0.5
ρ (% bulk)	92 ± 1	104 ± 3	103 ± 6	97 ± 5	103 ± 5	80 ± 10
σ(nm)	18 ± 0.3	4.2 ± 0.6	3.8 ± 0.1	1.5 ± 0.9	4.1 ± 0.3	2.3 ± 0.4
Ni: d (nm)	4.5 ± 0.7	3.5 ± 0.1	2.4 ± 0.1	2.1 ± 0.1	0.7 ± 0.2 †	0.7 ± 0.1 †
ρ (% bulk)	91 ± 1	83 ± 2	90 ± 1	101 ± 3	90 ± 20	87 ± 8
σ(nm)	3.2 ± 0.2	2.7 ± 0.2	3.9 ± 0.2	3.3 ± 0.2	3.9 ± 0.2	4.0 ± 0.2
M (μ_B/atom)	0.40 ± 0.02	0.46 ± 0.03	0.51 ± 0.03	0.45 ± 0.03	0.57 ± 0.04	0.27 ± 0.09
$NiBi_3$: d (nm)	2.3 ± 0.4	8.7 ± 0.7	15 ± 2	19 ± 2	24 ± 1	38.8 ± 0.7
ρ (% bulk)	92 ± 2	103 ± 3	99 ± 1	96 ± 7	99 ± 2	91 ± 1
σ(nm)	4.7 ± 0.3	4.5 ± 0.2	3.5 ± 0.3	4.6 ± 0.3	3.8 ± 0.3	5.2 ± 0.3
M (μ_B/atom)	0.03 ± 0.1	0.01 ± 0.05	0.01 ± 0.02	0.01 ± 0.02	0 ± 0.03	0 ± 0.01
Bi: d (nm)	44.1 ± 0.4	37.8 ± 0.8	30 ± 1	29 ± 2	20.9 ± 0.8	9.3 ± 0.7
ρ (% bulk)	96 ± 1	95 ± 2	97 ± 2	97 ± 1	106 ± 3 *	105 ± 1 *
σ(nm)	7.9 ± 0.9	9.5 ± 0.7	7.9 ± 0.8	7 ± 2	15 ± 3	9 ± 1
SiO_2: d (nm)	95.0 ± 0.3	95.1 ± 0.6	95.1 ± 0.3	95.1 ± 0.3	94.7 ± 0.4	93.9 ± 0.5
ρ (% bulk)	100.5 ± 0.1	99.8 ± 0.2	99.9 ± 0.7	99.9 ± 0.3	100.6 ± 0.3	100.1 ± 0.2
σ(nm)	0.1 ± 0.4	0.1 ± 0.7	0.2 ± 0.5	0.4 ± 0.6	0.2 ± 0.4	0.2 ± 0.6
Si: ρ Fixed (% bulk)	100	100	100	100	100	100
σ(nm)	0.1 ± 0.3	0.1 ± 0.4	0.2 ± 0.3	0.2 ± 0.3	0.2 ± 0.2	0.3 ± 0.2

Table A.1: Fitting parameters for the each $70°$ C annealing step with the FOM. The Si substrate density is fixed to the bulk value and all other parameters are free fitting. The density for each free layer is fitted with tight bounds to remain physical. (*) The final two Bi densities are higher that bulk as there is Ni inclusion throughout the layer. (†) GenX does not correctly fit very thin layers

Parameters	1800s	3600s
FOM	1.167	1.807
Ta_2O_5: d (nm)	2.2 ± 0.4	5.1 ± 0.8
ρ (% bulk)	90 ± 10	79 ± 2
σ(nm)	4.4 ± 0.2	4.2 ± 0.1
Ta: d (nm)	2.2 ± 0.4	3.1 ± 0.5
ρ (% bulk)	101 ± 7	103 ± 2
σ(nm)	4 ± 2	1 ± 2
NiBi: d (nm)	3.6 ± 0.8	3.5 ± 0.8
ρ (% bulk)	108 ± 9	90 ± 3
σ(nm)	4 ± 2	10 ± 1
M (μ_B/atom)	0.4 ± 0.1	0.5 ± 0.2
$NiBi_3$: d (nm)	24 ± 1	38 ± 1
ρ (% bulk)	98 ± 2	88.4 ± 0.8
σ(nm)	5.5 ± 0.6	8.5 ± 0.6
M (μ_B/atom)	0.02 ± 0.02	0.00 ± 0.03
Bi: d (nm)	22 ± 1	4.5 ± 0.4
ρ (% bulk)	106 ± 2	92 ± 2
σ(nm)	16 ± 1	3.6 ± 0.5
SiO_2: d (nm)	94.4 ± 0.3	94.9 ± 0.2
ρ (% bulk)	100.7 ± 0.2	100.0 ± 0.3
σ(nm)	0.1 ± 0.5	0.1 ± 0.4
Si: ρ Fixed (% bulk)	100.0	100.0
σ(nm)	0.1 ± 0.3	0.1 ± 0.3

Table A.2: Table of fitted values with the NiBi layer instead of the Ni layer, bulk density from the ordered alloy of NiBi.

References

[1] Stephen L. Adler. Axial-vector vertex in spinor electrodynamics. *Physical Review*, 177(5):2426–2438, 1969.

[2] W. Al-Sawai, Hsin Lin, R. S. Markiewicz, L. A. Wray, Y. Xia, S.-Y. Xu, M. Z. Hasan, and A. Bansil. Topological electronic structure in half-Heusler topological insulators. *Physical Review B*, 82(12):125208, sep 2010.

[3] N. E. Alekseevskii, N. B. Brandt, and T. I. Kostina. Superconductivity of binary alloys of bismuth. *Izv. Akad. Nauk SSSR*, 16:233–263, 1952.

[4] B. L. Altschuler and A. G. Aronov. Magnetoresistance of thin films and wires in a longitudinal magnetic field. *Zh. Eksp. Teor. Fiz. PisÓa Red*, 10:515–518, May 1981.

[5] André Anders. A structure zone diagram including plasma-based deposition and ion etching. Technical Report 1, apr 2016.

[6] Yoichi Ando. Topological insulator materials, oct 2013.

[7] Joseph E. Avron, Daniel Osadchy, and Ruedi Seiler. A topological look at the quantum hall effect. *Physics Today*, 56(8):38–42, aug 2003.

[8] A. Bansil, Hsin Lin, and Tanmoy Das. Colloquium: Topological band theory. *Reviews of Modern Physics*, 88(2), 2016.

[9] J. Bardeen, L. N. Cooper, and J. R. Schrieffer. Theory of superconductivity. *Physical Review*, 108(5):1175–1204, 1957.

[10] Joseph Thomas Batley. *Spin Transport in Lateral Spin Valves*. PhD thesis, University of Leeds, 2015.

[11] V. Berezinskii. New model of the anisotropic phase of superfluid He3. *Soviet Journal of Experimental and Theoretical Physics Letters*, 20(9):287, 1974.

[12] F S Bergeret and I V Tokatly. Spin-orbit coupling as a source of long-range triplet proximity effect in superconductor-ferromagnet hybrid structures. *Phys. Rev. B*, 89(13):134517, apr 2014.

[13] F S Bergeret, A F Volkov, and K B Efetov. Long-Range Proximity Effects in Superconductor-Ferromagnet Structures. *Phys. Rev. Lett.*, 86(18):4096–4099, apr 2001.

[14] F. S. Bergeret, A. F. Volkov, and K. B. Efetov. Long-range proximity effects in superconductor-ferromagnet structures. *Physical Review Letters*, 86(18):4096–4099, apr 2001.

[15] B Andrei Bernevig, Taylor L Hughes, and Shou-Cheng Zhang. Quantum spin Hall effect and topological phase transition in HgTe quantum wells. *Science (New York, N.Y.)*, 314(5806):1757–61, dec 2006.

[16] Matts Björck and Gabriella Andersson. GenX : an extensible X-ray reflectivity refinement program utilizing differential evolution. *J. Appl. Crystallogr.*, 40(6):1174–1178, dec 2007.

[17] Albert James Bradley, Rodgers, and J. W. The crystal structure of the heusler alloys. *Proceedings of the Royal Society of London. Series A, Containing Papers of a Mathematical and Physical Character*, 144(852):340–359, mar 1934.

[18] W Buckel and J Wittig. Supraleitung von germanium und silizium unter hohem druck. *Phys. Lett.*, 17(3):187–188, jul 1965.

[19] N. P. Butch, P. Syers, K. Kirshenbaum, A. P. Hope, and J. Paglione. Superconductivity in the topological semimetal YPtBi. *Physical Review B*, 84(22):220504, dec 2011.

[20] I A Campbell, A Fert, and O Jaoul. The spontaneous resistivity anisotropy in Ni-based alloys. *Journal of Physics C: Solid State Physics*, 3(1S):S95–S101, may 1970.

[21] Stanislav Chadov, Xiaoliang Qi, Jürgen Kübler, Gerhard H. Fecher, Claudia Felser, and Shou Cheng Zhang. Tunable multifunctional topological insulators in ternary Heusler compounds. *Nature Materials*, 9(7):541–545, 2010.

[22] Prashant Chauhan, Fahad Mahmood, Di Yue, Peng-Chao Xu, Xiaofeng Jin, and N. P. Armitage. Nodeless Bulk Superconductivity in the Time-Reversal Symmetry Breaking Bi/Ni Bilayer System. *Phys. Rev. Lett.*, 122(1):017002, jan 2019.

[23] Shiing-shen Chern. On the Curvatura Integra in a Riemannian Manifold. *The Annals of Mathematics*, 46(4):674, oct 1945.

[24] Piers Coleman. *Introduction to many-body physics*. Cambridge University Press, 2015.

[25] Stefano Curiotto, Harry Chien, Hila Meltzman, Stephane Labat, Paul Wynblatt, Gregory S. Rohrer, Wayne D. Kaplan, and Dominique Chatain. Copper crystals on the (1120) sapphire plane: orientation relationships, triple line ridges and interface shape equilibrium. *Journal of Materials Science*, 48(7):3013–3026, apr 2013.

[26] Supriyo Datta. *Electronic Transport in Mesoscopic Systems*. Cambridge University Press, sep 1995.

[27] R D dos Reis, M O Ajeesh, N Kumar, F Arnold, C Shekhar, M Naumann, M Schmidt, M Nicklas, and E Hassinger. On the search for the chiral anomaly in Weyl semimetals: the negative longitudinal magnetoresistance. *New Journal of Physics*, 18(8):085006, aug 2016.

[28] A. J. Drew, M. W. Wisemayer, D. O. G. Heron, S. Lister, S. L. Lee, A. Potenza, C. H. Marrows, R. M. Dalgliesh, T. R. Charlton, and S. Langridge. Using spin-polarized neutron reflectivity to probe mesoscopic vortex states in a Pb thin-film superconductor. *Phys. Rev. B*, 80(13):134510, oct 2009.

[29] Leonhard Euler. Solutio problematis ad geometriam situs pertinentis. *Commentarii academiae scientiarum Petropolitanae*, pages 128–140, 1741.

[30] Z. Fisk, P. C. Canfield, W. P. Beyermann, J. D. Thompson, M. F. Hundley, H. R. Ott, E. Felder, M. B. Maple, M. A. Lopez de la Torre, P. Visani, and C. L.

Seaman. Massive electron state in ybbipt. *Phys. Rev. Lett.*, 67:3310–3313, Dec 1991.

[31] M. G. Flokstra, T. C. Cunningham, J. Kim, N. Satchell, G. Burnell, P. J. Curran, S. J. Bending, C. J. Kinane, J. F.K. Cooper, S. Langridge, A. Isidori, N. Pugach, M. Eschrig, and S. L. Lee. Controlled suppression of superconductivity by the generation of polarized Cooper pairs in spin-valve structures. *Physical Review B - Condensed Matter and Materials Physics*, 91(6), feb 2015.

[32] M. G. Flokstra, N. Satchell, J. Kim, G. Burnell, P. J. Curran, S. J. Bending, J. F. K. Cooper, C. J. Kinane, S. Langridge, A. Isidori, N. Pugach, M. Eschrig, H. Luetkens, A. Suter, T. Prokscha, and S. L. Lee. Remotely induced magnetism in a normal metal using a superconducting spin-valve. *Nat. Phys.*, 12(1):57–61, jan 2016.

[33] M G Flokstra, R Stewart, N Satchell, G Burnell, H Luetkens, T Prokscha, A Suter, E Morenzoni, S Langridge, and S L Lee. Manifestation of the electromagnetic proximity effect in superconductor-ferromagnet thin film structures. *Appl. Phys. Lett.*, 115(7):072602, aug 2019.

[34] Kenji Fukushima, Dmitri E. Kharzeev, and Harmen J. Warringa. Chiral magnetic effect. *Physical Review D - Particles, Fields, Gravitation and Cosmology*, 78(7):074033, oct 2008.

[35] Martine Gautier, Gilles Fenaud, Laurent Pham Van, Bruno Villette, Maud Pollak, Nathalie Thromat, Francois Jollet, and Jean-Paul Duraud. alpha-Al2O3 (0001) Surfaces: Atomic and Electronic Structure. *Journal of the American Ceramic Society*, 77(2):323–334, feb 1994.

[36] V L Ginzburg. Ferromagnetic Superconductors. *Sov. Phys. JETP*, 4(2):153–160, 1957.

[37] Hubert Gnaser. Energy and angular distributions of sputtered species. *Topics in Applied Physics*, 110(94):231–328, 2007.

[38] Xin-Xin Gong, He-Xin Zhou, Peng-Chao Xu, Di Yue, Kai Zhu, Xiao-Feng Jin, He Tian, Ge-Jian Zhao, and Ting-Yong Chen. Possible p-Wave Superconductivity in Epitaxial Bi/Ni Bilayers. *Chinese Phys. Lett.*, 32(6):067402, jun 2015.

[39] Xinxin Gong, Mehdi Kargarian, Alex Stern, Di Yue, Hexin Zhou, Xiaofeng Jin, Victor M Galitski, Victor M Yakovenko, and Jing Xia. Time-reversal symmetry-breaking superconductivity in epitaxial bismuth/nickel bilayers. *Sci. Adv.*, 3(3):e1602579, mar 2017.

[40] C. Y. Guo, F. Wu, Z. Z. Wu, M. Smidman, C. Cao, A. Bostwick, C. Jozwiak, E. Rotenberg, Y. Liu, F. Steglich, and H. Q. Yuan. Evidence for Weyl fermions in a canonical heavy-fermion semimetal YbPtBi. *Nature Communications*, 9(1):4622, dec 2018.

[41] Chunyu Guo, Fan Wu, Michael Smidman, and Huiqiu Yuan. Sample dependence studies of the Kondo Weyl semimetal YbPtBi. *AIP Advances*, 8(10):101336, oct 2018.

[42] Friedrich Heusler. Über magnetische manganlegierungen. *Verhandlungen der Deutschen Physikalischen Gesellschaft*, 5:219, 1903.

[43] Atsufumi Hirohata, Teodor Huminiuc, John Sinclair, Haokaifeng Wu, Marjan Samiepour, Gonzalo Vallejo-Fernandez, Kevin O'Grady, Jan Balluf, Markus Meinert, Günter Reiss, Eszter Simon, Sergii Khmelevskyi, Laszlo Szunyogh, Rocio Yanes Díaz, Ulrich Nowak, Tomoki Tsuchiya, Tomoko Sugiyama, Takahide Kubota, Koki Takanashi, Nobuhito Inami, and Kanta Ono. Development of antiferromagnetic Heusler alloys for the replacement of iridium as a critically raw material. *Journal of Physics D: Applied Physics*, 50(44):443001, sep 2017.

[44] Max Hirschberger, Satya Kushwaha, Zhijun Wang, Quinn Gibson, Sihang Liang, Carina A. Belvin, B. A. Bernevig, R. J. Cava, and N. P. Ong. The chiral anomaly and thermopower of Weyl fermions in the half-Heusler GdPtBi. *Nature Materials*, 15(11):1161–1165, nov 2016.

[45] H. J. Höfler, R. S. Averback, H. Hahn, and H. Gleiter. Diffusion of bismuth and gold in nanocrystalline copper. *J. Appl. Phys.*, 74(6):3832–3839, sep 1993.

[46] D. Hsieh, D. Qian, L. Wray, Y. Xia, Y. S. Hor, R. J. Cava, and M. Z. Hasan. A topological Dirac insulator in a quantum spin Hall phase. *Nature*, 452(7190):970–974, apr 2008.

[47] Xiaochun Huang, Lingxiao Zhao, Yujia Long, Peipei Wang, Dong Chen, Zhanhai Yang, Hui Liang, Mianqi Xue, Hongming Weng, Zhong Fang, Xi Dai, and Genfu Chen. Observation of the chiral-anomaly-induced negative magnetoresistance: In 3D Weyl semimetal TaAs. *Physical Review X*, 5(3):031023, aug 2015.

[48] Jun ichi Wakabayashi and Shinji Kawaji. Hall Effect in Silicon MOS Inversion Layers Under Strong Magnetic Fields. *Journal of the Physical Society of Japan*, 44(6):1839–1849, dec 1978.

[49] Kun-Rok Jeon, Chiara Ciccarelli, Andrew J Ferguson, Hidekazu Kurebayashi, Lesley F Cohen, Xavier Montiel, Matthias Eschrig, Jason W A Robinson, and Mark G Blamire. Enhanced spin pumping into superconductors provides evidence for superconducting pure spin currents. *Nat. Mater.*, 17(6):499–503, jun 2018.

[50] M. H. Jung, T. Yoshino, S. Kawasaki, T. Pietrus, Y. Bando, T. Suemitsu, M. Sera, and T. Takabatake. Thermoelectric and transport properties of CeBiPt and LaBiPt. *Journal of Applied Physics*, 89(11):7631–7633, jun 2001.

[51] Lord Kelvin. On vortex atoms. Technical report, 1867.

[52] Moo-Sung Kim, Tetsuya Sasakawa, Toshiaki Suemitsu, Yoshio Bando, Kazunori Umeo, Fumitoshi Iga, Hiroyuki Mitamura, Tsuneaki Goto, and Toshiro Takabatake. Transport and Magnetic Properties of a Low-Density Carrier System SmBiPt. *Journal of the Physical Society of Japan*, 70(12):3650–3653, dec 2001.

[53] W. Kraus and G. Nolze. POWDER CELL – a program for the representation and manipulation of crystal structures and calculation of the resulting X-ray powder patterns. *Journal of Applied Crystallography*, 29(3):301–303, jun 1996.

[54] A. Kreyssig, M. G. Kim, J. W. Kim, D. K. Pratt, S. M. Sauerbrei, S. D. March, G. R. Tesdall, S. L. Bud'Ko, P. C. Canfield, R. J. McQueeney, and A. I. Goldman. Magnetic order in GdBiPt studied by x-ray resonant magnetic scattering. *Physical Review B - Condensed Matter and Materials Physics*, 84(22):220408, dec 2011.

[55] P. LeClair, J. S. Moodera, J. Philip, and D. Heiman. Coexistence of Ferromagnetism and Superconductivity in Ni/Bi Bilayers. *Phys. Rev. Lett.*, 94(3):037006, jan 2005.

[56] Qiang Li, Dmitri E. Kharzeev, Cheng Zhang, Yuan Huang, I. Pletikosić, A. V. Fedorov, R. D. Zhong, J. A. Schneeloch, G. D. Gu, and T. Valla. Chiral magnetic effect in ZrTe5. *Nature Physics*, 12(6):550–554, jun 2016.

[57] Yufeng Li, Enyu Wang, Xiyu Zhu, and Hai-Hu Wen. Pressure-induced superconductivity in Bi single crystals. *Phys. Rev. B*, 95(2):024510, jan 2017.

[58] Jianjun Lin and Huisu Chen. Measurement of continuum percolation properties of two-dimensional particulate systems comprising congruent and binary super-ellipses. *Powder Technology*, 347:17–26, apr 2019.

[59] L. Y. Liu, Y. T. Xing, I. L. C. Merino, H. Micklitz, D. F. Franceschini, E. Baggio-Saitovitch, D. C. Bell, and I. G. Solórzano. Superconductivity in Bi/Ni bilayer system: Clear role of superconducting phases found at Bi/Ni interface. *Phys. Rev. Mater.*, 2(1):014601, jan 2018.

[60] G Ml Luke, Y Fudamoto, K M Kojima, M I Larkin, J Merrin, B Nachumi, Y J Uemura, Y Maeno, Z Q Mao, Y Mori, H. Nakamura, and M. Sigrist. Time-reversal symmetry-breaking superconductivity in Sr2RuO4. *Nature*, 394(6693):558–561, aug 1998.

[61] Kaustuv Manna, Yan Sun, Lukas Muechler, Jürgen Kübler, and Claudia Felser. Heusler, Weyl and Berry. *Nature Reviews Materials*, 3(8):244–256, 2018.

[62] X. Marti, V. Skumryev, C. Ferrater, M. V. García-Cuenca, M. Varela, F. Sánchez, and J. Fontcuberta. Emergence of ferromagnetism in antiferromagnetic TbMnO3 by epitaxial strain. *Applied Physics Letters*, 96(22):222505, may 2010.

[63] J. S. Moodera and R. Meservey. Superconducting phases of Bi and Ga induced by deposition on a Ni sublayer. *Phys. Rev. B*, 42(1):179–183, jul 1990.

[64] R. A. Müller, N. R. Lee-Hone, L. Lapointe, D. H. Ryan, T. Pereg-Barnea, A. D. Bianchi, Y. Mozharivskyj, and R. Flacau. Magnetic structure of GdBiPt: A candidate antiferromagnetic topological insulator. *Physical Review B - Condensed Matter and Materials Physics*, 90(4):041109, jul 2014.

[65] E. D. Mun, S. L. Bud'Ko, C. Martin, H. Kim, M. A. Tanatar, J. H. Park, T. Murphy, G. M. Schmiedeshoff, N. Dilley, R. Prozorov, and P. C. Canfield.

Magnetic-field-tuned quantum criticality of the heavy-fermion system YbPtBi. *Physical Review B - Condensed Matter and Materials Physics*, 87(7):32–35, 2013.

[66] Eundeok Mun. *Yb-based heavy fermion compounds and field tuned quantum criticality.* PhD thesis, Iowa State University, Digital Repository, Ames, 2010.

[67] Naoto Nagaosa and Naoto Nagaosa. Symmetry Breaking and Phase Transition. In *Quantum Field Theory in Condensed Matter Physics*, pages 51–89. Springer Berlin Heidelberg, 1999.

[68] Yasuyuki Nakajima, Rongwei Hu, Kevin Kirshenbaum, Alex Hughes, Paul Syers, Xiangfeng Wang, Kefeng Wang, Renxiong Wang, Shanta R. Saha, Daniel Pratt, Jeffrey W. Lynn, and Johnpierre Paglione. Topological RPdBi half-Heusler semi-metals: A new family of noncentrosymmetric magnetic superconductors. *Science Advances*, 1(5), jun 2015.

[69] Takeo Nakano and Shigeru Baba. Estimation of the pressureâ€"distance product for thermalization in sputtering for some selected metal atoms by Monte Carlo simulation. *Japanese Journal of Applied Physics*, 53(3):038002, mar 2014.

[70] C. Nash. Topology and physics-a historical essay. sep 1997.

[71] National Institute of Standards and Technology. X-Ray Transition Energies Database, 2016.

[72] M.-A. Nicolet. Diffusion barriers in thin films. *Thin Solid Films*, 52(3):415–443, aug 1978.

[73] H. B. Nielsen and Masao Ninomiya. The Adler-Bell-Jackiw anomaly and Weyl fermions in a crystal. *Physics Letters B*, 130(6):389–396, nov 1983.

[74] Milton Ohring. *Epitaxy.* 2002.

[75] KTS Oldham. *The doctrine of description: Gustav Kirchhoff, classical physics, and the "purpose of all science" in 19th-century Germany.* 2008.

[76] Siham Ouardi, Gerhard H. Fecher, Claudia Felser, Jaroslav Hamrle, Kamil Postava, and Jaromír Pištora. Transport and optical properties of the gapless Heusler compound PtYSb. *Applied Physics Letters*, 99(21):211904, nov 2011.

[77] Siham Ouardi, Chandra Shekhar, Gerhard H. Fecher, Xeniya Kozina, Gregory Stryganyuk, Claudia Felser, Shigenori Ueda, and Keisuke Kobayashi. Electronic structure of Pt based topological Heusler compounds with C1b structure and "zero band gap". *Applied Physics Letters*, 98(21):211901, may 2011.

[78] S T Petcov. The Nature of Massive Neutrinos. *Advances in High Energy Physics*, 2013:20, 2013.

[79] V I Petrosyan, V N Molin, O I Vasin, P A Skripkina, S I Stenin, and E G Batyev. Superconductivity in polycrystalline bismuth films. *Vacuum*, 25(4):181, apr 1975.

[80] Om Prakash, Anil Kumar, A Thamizhavel, and S Ramakrishnan. Evidence for bulk superconductivity in pure bismuth single crystals at ambient pressure. *Science (80-.).*, 355(6320):52–55, jan 2017.

[81] Sumathi Rao. Weyl semi-metals: A short review, 2016.

[82] J W A Robinson, S Piano, G Burnell, C Bell, and M G Blamire. Zero to π transition in superconductor-ferromagnet-superconductor junctions. *Phys. Rev. B*, 76(9):094522, sep 2007.

[83] R. A. Robinson, A. Purwanto, M. Kohgi, P. C. Canfield, T. Kamiyama, T. Ishigaki, J. W. Lynn, R. Erwin, E. Peterson, and R. Movshovich. Crystallography and magnetism of the heavy-fermion compound YbBiPt. *Physical Review B*, 50(13):9595–9598, oct 1994.

[84] Stephen M. Rossnagel. Sputtered atom transport processes. *IEEE Transactions on Plasma Science*, 18(6):878–882, dec 1990.

[85] M. A. Ruderman and C. Kittel. Indirect Exchange Coupling of Nuclear Magnetic Moments by Conduction Electrons. *Physical Review*, 96(1):99–102, oct 1954.

[86] Gary J Russell. Spallation physics: An overview. In *Prepared for 11th Meeting of*, pages 291–299, 1990.

[87] Nathan Satchell and Norman O Birge. Supercurrent in ferromagnetic Josephson junctions with heavy metal interlayers. *Phys. Rev. B*, 97(21):214509, jun 2018.

[88] Nathan Satchell, Reza Loloee, and Norman O Birge. Supercurrent in ferromagnetic Josephson junctions with heavy-metal interlayers. II. Canted magnetization. *Phys. Rev. B*, 99(17):174519, may 2019.

[89] J. Schechter and J. W. F. Valle. Neutrino masses in SU(2)×U(1) theories. *Physical Review D*, 22(9):2227–2235, nov 1980.

[90] Home Search, Collections Journals, About Contact, My Iopscience, and I P Address. Structural and electronic properties of epitaxial V_2O_3. *Journal of Physics: Condensed Matter*, 77(41):413101, jul 2007.

[91] Rong Shan, Enrique V. Vilanova, Juan Qin, Frederick Casper, Gerhard H. Fecher, Gerhard Jakob, and Claudia Felser. Fabrication and characterization of semiconducting half-Heusler YPtSb thin films. *Physica Status Solidi - Rapid Research Letters*, 7(1-2):145–147, 2013.

[92] Chandra Shekhar, Ajaya K. Nayak, Sanjay Singh, Nitesh Kumar, Shu-Chun Wu, Yang Zhang, Alexander C. Komarek, Erik Kampert, Yurii Skourski, Jochen Wosnitza, Walter Schnelle, Alix McCollam, Uli Zeitler, Jurgen Kubler, S. S. P. Parkin, Binghai Yan, and C. Felser. Observation of chiral magneto-transport in RPtBi topological Heusler compounds. *arXiv*, page 1604.01641, 2016.

[93] Chandra Shekhar, Siham Ouardi, Ajaya K. Nayak, Gerhard H. Fecher, Walter Schnelle, and Claudia Felser. Ultrahigh mobility and nonsaturating magnetoresistance in Heusler topological insulators. *Physical Review B - Condensed Matter and Materials Physics*, 86(15):1–6, 2012.

[94] B Silva, R F Luccas, N M Nemes, J Hanko, M R Osorio, P Kulkarni, F Mompean, M. García-Hernández, M A Ramos, S Vieira, and H Suderow. Superconductivity and magnetism on flux-grown single crystals of nibi3. *Phys. Rev. B*, 88(18):184508, nov 2013.

[95] Vantari Siva, Kartik Senapati, Biswarup Satpati, Sudakshina Prusty, D K Avasthi, D Kanjilal, and Pratap K Sahoo. Spontaneous formation of superconducting NiBi3 phase in Ni/Bi bilayer films. *J. Appl. Phys.*, 117(8):83902, 2015.

[96] D. T. Son and B. Z. Spivak. Chiral anomaly and classical negative magnetoresistance of Weyl metals. *Physical Review B*, 88(10):104412, sep 2013.

[97] Mingliang Tian, Jian Wang, Qi Zhang, Nitesh Kumar, Thomas E Mallouk, and Moses H W Chan. Superconductivity and quantum oscillations in crystalline {Bi} nanowire. *Nano Lett.*, 9(9):3196–3202, 2009.

[98] Masashi Tokuda, Natsuki Kabeya, Komei Iwashita, Hiroki Taniguchi, Tomonori Arakawa, Di Yue, Xinxin Gong, Xiaofeng Jin, Kensuke Kobayashi, and Yasuhiro Niimi. Spin transport measurements in metallic Bi/Ni nanowires. *Appl. Phys. Express*, 12(5):53005, 2019.

[99] B. G. Ueland, A. Kreyssig, E. D. Mun, J. W. Lynn, L. W. Harriger, D. K. Pratt, K. Prokeš, Z. Hüsges, R. Toft-Petersen, S. Sauerbrei, S. M. Saunders, Y. Furukawa, S. L. Bud'ko, R. J. McQueeney, P. C. Canfield, and A. I. Goldman. Magnetic-field effects on the fragile antiferromagnetism in ybbipt. *Phys. Rev. B*, 99:184431, May 2019.

[100] Leo J. van der Pauw. A method of measuring the resistivity and Hall coefficient on lamellae of arbitrary shape. *Philips Technical Review*, 20:220–224, 1958.

[101] Matthew Vaughan, Nathan Satchell, Mannan Ali, Christian J. Kinane, Gavin B. G. Stenning, Sean Langridge, and Gavin Burnell. Origin of superconductivity at nickel-bismuth interfaces. *Physical Review Research*, 2(1):013270, mar 2020.

[102] Jing Wang and Shou Cheng Zhang. Topological states of condensed matter. *Nature Materials*, 16(11):1062–1067, 2017.

[103] Junhua Wang, Xinxin Gong, Guang Yang, Zhaozheng Lyu, Yuan Pang, Guangtong Liu, Zhongqing Ji, Jie Fan, Xiunian Jing, Changli Yang, Fanming Qu, Xiaofeng Jin, and Li Lu. Anomalous magnetic moments as evidence of chiral superconductivity in a Bi/Ni bilayer. *Phys. Rev. B*, 96(5):054519, aug 2017.

[104] Wenhong Wang, Yin Du, Enke Liu, Zhongyuan Liu, and G. H. Wu. Fabrication and characterization of the gapless half-Heusler YPtSb thin films. *Journal of Applied Physics*, 112(10):103910, nov 2012.

[105] Pierre Weiss. L'hypothèse du champ moléculaire et la propriété ferromagnétique. *Journal de Physique Théorique et Appliquée*, 6(1):661–690, 1907.

[106] B Weitzel and H Micklitz. Superconductivity in granular systems built from well-defined rhombohedral Bi-clusters: Evidence for Bi-surface superconductivity. *Phys. Rev. Lett.*, 66(3):385–388, jan 1991.

[107] G. Wenski and A. Mewis. REPtX compounds with structures related to AIB2- and MgAgAs-type (RE=Y, Rare earth element;X = P, As, Sb). *Zeitschrift für Kristallographie - Crystalline Materials*, 176(1-2), jan 1986.

[108] Hermann Weyl. Gravitation and the electron. *Proceedings of the National Academy of Sciences of the United States of America*, 15(4):323, 1929.

[109] J. S. White, M. Bator, Y. Hu, H. Luetkens, J. Stahn, S. Capelli, S. Das, M. Döbeli, Th Lippert, V. K. Malik, J. Martynczuk, A. Wokaun, M. Kenzelmann, Ch Niedermayer, and C. W. Schneider. Strain-induced ferromagnetism in antiferromagnetic LuMnO3 thin films. *Physical Review Letters*, 111(3), jul 2013.

[110] A.R. Wildes, J. Mayer, and K. Theis-Bröhl. The growth and structure of epitaxial niobium on sapphire. *Thin Solid Films*, 401(1-2):7–34, dec 2001.

[111] Ning Xu, Yong Xu, and Jia Zhu. Topological insulators for thermoelectrics, dec 2017.

[112] S.-Y. Xu, Ilya Belopolski, Nasser Alidoust, Madhab Neupane, Guang Bian, Chenglong Zhang, Raman Sankar, Guoqing Chang, Zhujun Yuan, C.-C. Lee, S.-M. Huang, Hao Zheng, Jie Ma, Daniel S. Sanchez, B. Wang, Arun Bansil, Fangcheng Chou, Pavel P. Shibayev, Hsin Lin, Shuang Jia, and M. Zahid Hasan. Discovery of a Weyl fermion semimetal and topological Fermi arcs. *Science*, 349(6248):613–617, aug 2015.

[113] Binghai Yan and Claudia Felser. Topological Materials: Weyl Semimetals. *Annual Review of Condensed Matter Physics*, 8(1):337–354, 2017.

[114] Binghai Yan and Shou Cheng Zhang. Topological materials. *Reports on Progress in Physics*, 75(9):096501, 2012.

[115] H Zabel, K. Theis Brohl, M Wolff, and B.P. Toperverg. Polarized Neutron Reflectometry for the Analysis of Nanomagnetic Systems. *IEEE Trans. Magn.*, 44(7):1928–1934, jul 2008.

[116] Huai Zhang, J W Lynn, C F Majkrzak, S K Satija, J H Kang, and X D Wu. Measurements of magnetic screening lengths in superconducting Nb thin films by polarized neutron reflectometry. *Phys. Rev. B*, 52(14):10395–10404, oct 1995.

[117] G J Zhao, X X Gong, P C Xu, B C Li, Z Y Huang, X F Jin, X D Zhu, and T Y Chen. Singlet superconductivity in a single-crystal NiBi 3 superconductor. *Supercond. Sci. Technol.*, 31(12):125005, dec 2018.

[118] Hexin Zhou, Xinxin Gong, and Xiaofeng Jin. Magnetic properties of superconducting Bi/Ni bilayers. *J. Magn. Magn. Mater.*, 422:73–76, jan 2017.

[119] Hexin Zhou and Xiaofeng Jin. Stray field and vortex controlled magnetoresistance in superconducting Bi/Ni bilayers. *J. Magn. Magn. Mater.*, 458:171–175, jul 2018.